Lawrence Berkeley National Laboratory
Recent Work

Title
MEASUREMENT OF THE POLARIZATION PARAMETER IN Jt+p SCATTERING FROM 750 TO 3750 MeV/c

Permalink
https://escholarship.org/uc/item/9rx5p2p7

Author
Johnson, Claiborne Holt

Publication Date
1967-08-01

eScholarship.org Powered by the California Digital Library
University of California

UCRL-17683

eg. 2

University of California

Ernest O. Lawrence Radiation Laboratory

MEASUREMENT OF THE POLARIZATION PARAMETER IN $\pi^+ p$ SCATTERING FROM 750 TO 3750 MeV/c

Claiborne Holt Johnson, Jr.
(Ph. D. Thesis)

August 1967

TWO-WEEK LOAN COPY

This is a Library Circulating Copy which may be borrowed for two weeks. For a personal retention copy, call Tech. Info. Division, Ext. 5545

Berkeley, California

UCRL-17683
eg. 2

DISCLAIMER

This document was prepared as an account of work sponsored by the United States Government. While this document is believed to contain correct information, neither the United States Government nor any agency thereof, nor the Regents of the University of California, nor any of their employees, makes any warranty, express or implied, or assumes any legal responsibility for the accuracy, completeness, or usefulness of any information, apparatus, product, or process disclosed, or represents that its use would not infringe privately owned rights. Reference herein to any specific commercial product, process, or service by its trade name, trademark, manufacturer, or otherwise, does not necessarily constitute or imply its endorsement, recommendation, or favoring by the United States Government or any agency thereof, or the Regents of the University of California. The views and opinions of authors expressed herein do not necessarily state or reflect those of the United States Government or any agency thereof or the Regents of the University of California.

UCRL-17683

UNIVERSITY OF CALIFORNIA

Lawrence Radiation Laboratory
Berkeley, California

AEC Contract No. W-7405-eng-48

MEASUREMENT OF THE POLARIZATION PARAMETER IN $\pi^+ p$ SCATTERING FROM 750 TO 3750 MeV/c

Claiborne Holt Johnson, Jr.
(Ph. D. Thesis)

August 1967

MEASUREMENT OF THE POLARIZATION PARAMETER IN $\pi^+ p$ SCATTERING FROM 750 TO 3750 MeV/c

Contents

MEASUREMENT OF THE POLARIZATION PARAMETER IN $\pi^+ p$ SCATTERING FROM 750 TO 3750 MeV/c*

Claiborne Holt Johnson, Jr.

Lawrence Radiation Laboratory
University of California
Berkeley, California

August 1967

ABSTRACT

We have measured the polarization parameter in $\pi^+ p$ elastic scattering at fifteen lab momenta from 745 to 3747 MeV/c. The positive pion beam was focussed on a one cubic inch polarized proton target and both final-state particles were detected by scintillation counter hodoscopes. On the basis of their coplanarity and opening angle, elastic events involving polarized protons were distinguished kinematically from background events. The polarization parameter was obtained by observing the asymmetry in counting rates detected when the target was polarized successively parallel and antiparallel to the normal to the scattering plane. These results, combined with those of other experiments, are being used to conduct a phase-shift analysis of the pion-nucleon system at 19 energies from 490 to 1566 MeV (1443 to 2025 MeV total center-of-mass energy). Several comments about this analysis and a tentative solution are presented. This solution is not in disagreement with earlier analyses, but its uniqueness has not yet been firmly demonstrated.

---

* Work done under the auspices of the U.S. Atomic Energy Commission.

I. INTRODUCTION

The pion-nucleon system, consisting as it does of particles with spin zero and one-half respectively, is one of the simplest in which the nature of the strong interaction can be studied directly. If this interaction obeys all the currently accepted symmetries, then its complete description in the case of πN elastic scattering at a given energy and scattering angle involves only four independent complex amplitudes. Two (the so-called "spin-flip" and "non-spin-flip" amplitudes) are required to describe the scattering in any given charge state. But the three charge states of the pion and two of the nucleon allow the existence of several types of reactions, each a different mixture of the two possible isotopic spin states, $I=1/2$ and $I=3/2$. Thus there are four amplitudes, two for each I-spin state, that describe all πN elastic scattering.

Each of the observables--total cross section, differential cross section, polarization and rotation of the spin of the nucleon--in any elastic πN reaction can be expressed by an appropriate combination of these amplitudes.[1] Conversely, accurate measurement of sufficiently many of the observables allows the amplitudes to be calculated and their dependence on energy to be studied. This has been the goal of a number of experiments[2-22] and analyses[23-29] in recent years.

With the availability of charged pion beams from modern high-energy accelerators, three types of elastic πN scattering have become readily accessible for study:

$$\pi^+ p \rightarrow \pi^+ p \qquad \text{(I-1a)}$$

$$\pi^- p \rightarrow \pi^- p \qquad \text{(I-1b)}$$

$$\pi^- p \rightarrow \pi^0 n \qquad \text{(I-1c)}$$

The first experiments done were measurements of total cross sections in πN scattering.[2-10] The results (Fig. 1) show a rich structure and indicate that the nuclear force is quite complicated even in this simple case.

Then differential cross section measurements[30-34] and recoil nucleon polarization measurements[35-36] exhibited the angular dependence of the reactions and led to a good understanding of the amplitudes up to beam energies of a few hundred MeV.[37] In this region the reaction is heavily dominated by the prominent "3-3" resonance at 1238 MeV total center-of-mass energy. By this we mean that the reaction tends to proceed predominantly through the intermediate pion-nucleon state with isotopic spin 3/2 and total angular momentum 3/2.

Most recently, with the development of polarized proton targets suitable for high-energy experiments,[38-40] it has become feasible to increase the number of polarization measurements enormously and extend them into the many-GeV range. Particular attention has been paid to the energy range above 300 MeV in which the structure in the total cross sections is obvious and where the most readily decipherable resonances are thought to exist. Enough data has been accumulated from the three types of differential cross section measurements listed in (I-1)[11-17] from polarization experiments in the reactions (I-1a and b)[18-22] to allow several groups to attempt reconstruction of the amplitudes

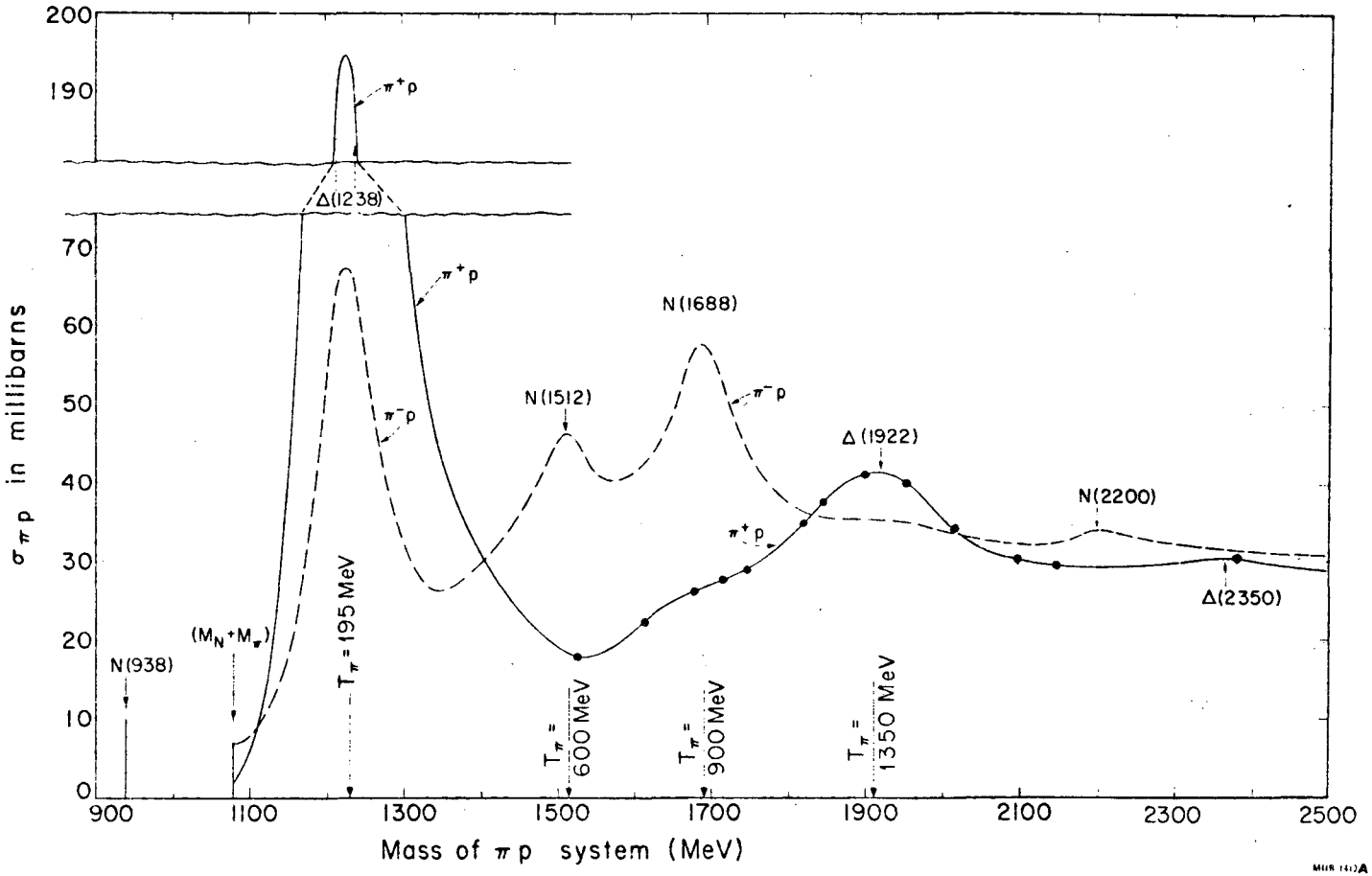

Fig. 1. Total cross sections for π^+p and π^-p reactions. The dots on the π^+p curve correspond to the momenta of this experiment.

by phase-shift analyses. The success of such an analysis depends on the short range of the nuclear force and involves expanding the amplitudes in truncated series of partial-wave amplitudes. These series explicitly exhibit the reactions' dependence on the angular momenta involved and separate the functions of energy from those of angle. Then various procedures are used to fit the partial amplitudes to the data and to discover their energy dependence. This, in turn, allows a great deal to be said about the behavior of the forces which underlie the bumps in the total cross sections.

These analyses have led to good understanding of the πN system up to at least 600 MeV and probably 1 GeV. But of the five types of data generally available, the $\pi^+ p$ polarization has been in shortest supply, even in the resonance region between .5 and 3 GeV. The experiment reported here was performed to improve this last situation; the phase-shift analysis, to test the effect of this new data on the earlier phase-shift findings.

Section II reviews briefly the general assumptions underlying a polarization measurement using a polarized target and describes the specific procedure used in this experiment. Section III explains how the raw data obtained was refined, results calculated, and errors estimated. The results themselves are presented in Section IV and discussed in Section V.

II. EXPERIMENTAL PROCEDURE AND EQUIPMENT

A. Method

The polarization parameter P in πN scattering was originally defined in terms of the recoiling nucleon from an unpolarized target. If the scattering is taken to be in the horizontal plane, then for a given center-of-mass angle θ,

$$P(\theta) = \frac{\text{number of nucleons with spin "up" minus number with spin "down"}}{\text{total number of nucleons recoiling at angle } \theta} \qquad \text{(II-1)}$$

(This "up" direction is more precisely defined below as the direction $\hat{n}$.) Many such experiments have been performed, but they all have had to face the difficulty of determining the recoil polarization through making the nucleon scatter a second time.

With the assumption that parity is conserved in the interaction or that it is invariant under time reversal, however, the same parameter can be determined with only one scattering if that scattering is from a polarized target. Only the differential cross section $I(\theta)$ and target polarization $\vec{P}_T$ need be measured. The relation between P, I, and $\vec{P}_T$ is

$$I(\theta) = I_o(\theta)(1 + P(\theta)\hat{n}\cdot\vec{P}_T) \qquad \text{(II-2)}$$

where I_o is the differential cross section measured with an unpolarized target, and $\hat{n} = \hat{k}_i \times \hat{k}_f$ is the unit normal to the plane determined by the pion's initial and final momenta $\vec{k}_i$ and $\vec{k}_f$. In practice it is easier to avoid systematic errors by measuring the two rates I_+ and I_-,

corresponding to scattering with target polarized in the direction of the normal to the plane of scattering and opposite to that normal, respectively. Then what is computed is the asymmetry

$$\epsilon(\theta) = \frac{I_+ - I_-}{I_+ + I_-} \qquad \text{(II-3)}$$

Finally (ignoring background),

$$P(\theta) = \frac{\epsilon(\theta)}{P_T} \qquad \text{(II-4)}$$

In the experiment reported here, $P(\theta)$ was determined by this second method. The experimental facilities of the Bevatron were used to direct beams of pions of selected momenta at a polarized proton target. The target geometry was such that $\hat{n}$ and $\vec{P}_T$ were horizontal in the lab. Scintillation counters were used to define the directions in the vertical scattering plane of the incoming pion and of each of the outgoing pion and nucleon.

B. Beam Design and Tuning

The pion beam originated in a $\frac{5}{16} \times \frac{1}{2} \times 3$ inch copper target placed at the third focus of the Bevatron's External Proton Beam (EPB). It was focussed and momentum-analysed by the four doublet quadrapole magnets, Q_1-Q_4, and three bending magnets, M_1-M_3, arranged as shown in Fig. 2. The small vertical bending magnet M_4, positioned just in front of the polarized target, was used to compensate for the vertical deflection of the beam in the magnetic field surrounding the target itself. Figure 3 gives a schematic view of the beam optics.

Except for three short sections--one just after the production target at the third focus of the EPB, one near the beam's first focus F_1, and one just before the polarized target at F_2--the beam was enclosed in a vacuum pipe to minimize its scattering in the atmosphere.

Beam momentum was determined by wire-orbit measurements of the second leg of the beam, through Q_3, M_3, and Q_4. The currents in the other magnets were then tuned empirically around their design values to give the best flux and profile at the target. A hodoscope composed of twenty-eight $1/4 \times 7$ inch scintillation counters greatly facilitated this tuning. It was placed perpendicular to the beam at the target position at the second focus and was mounted so that it could be rotated about the axis defined by the beam direction. A system of scalers and an on-line computer (see Section III) made it possible to obtain with this hodoscope a profile of the beam intensity from only one Bevatron pulse. The final result of this tuning was a beam spot at the second

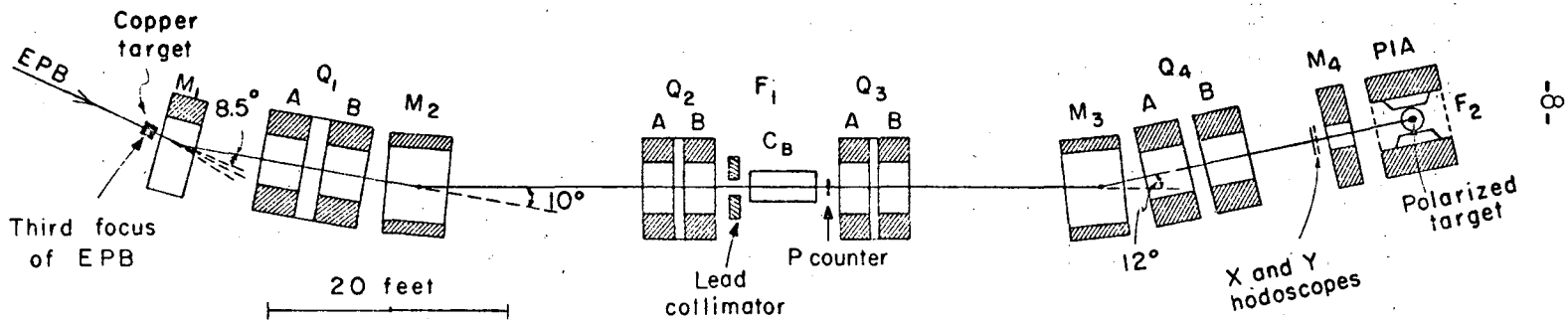

Beam layout

MUB-14038 A

Fig. 2.

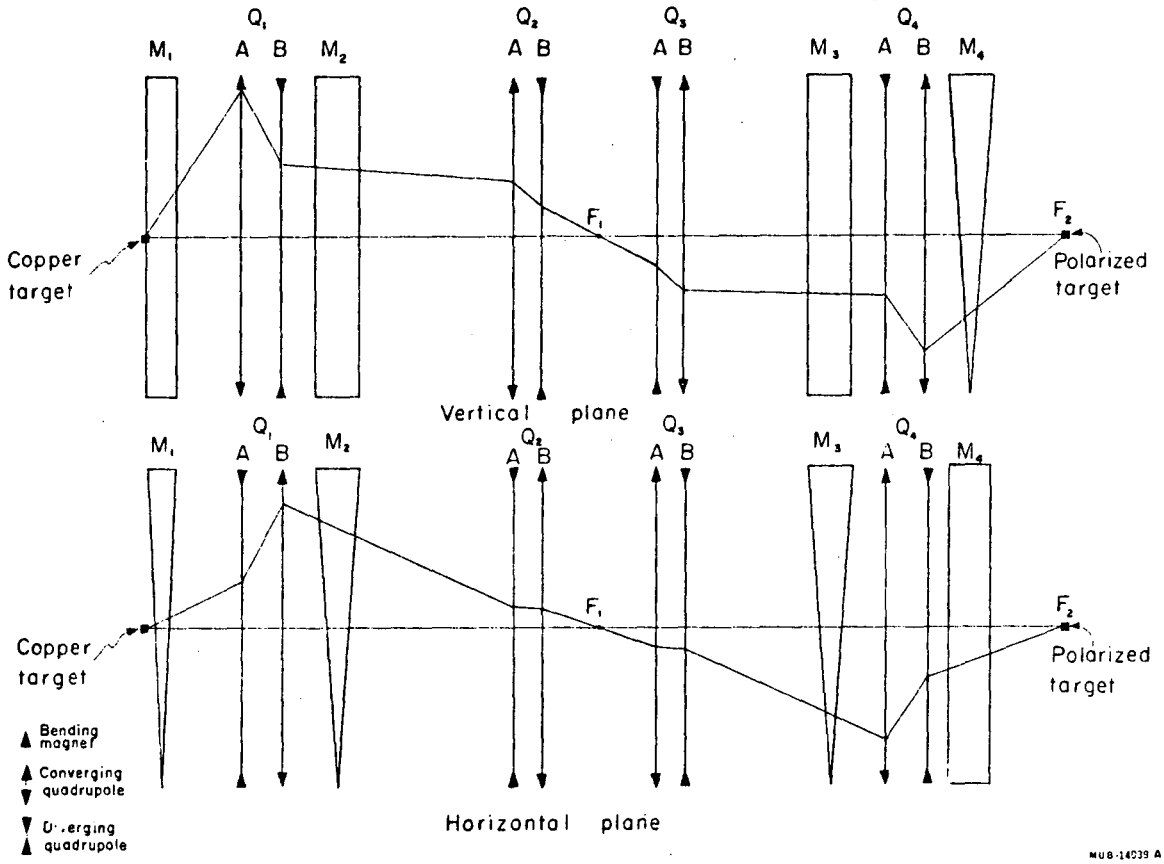

Fig. 3. Beam optics.

focus of approximately Gaussian shape and one inch diameter at half height (Fig. 4).

A momentum bite ($\Delta p/p$) of about 1-1/2% was obtained by placing a 1-1/2 inch wide lead collimator at the first focus where the momentum dispersion was 1% per inch in the horizontal plane.

Protons were the chief contaminant in the beam, with the ratio of protons to pions ranging from about 1:1 at 745 MeV/c to 4:1 at 3747 MeV/c. They were discriminated against in two ways. First the time-of-flight between the counter P at the first focus and the incident-beam-angle defining hodoscope near the second focus was appreciably different for protons and pions of the same momentum. This difference, Δt, ranged from more than twenty nsec at 745 MeV/c to less than four above 2 GeV/c. The beam counters were all physically small and their electronics fast enough so that the timing curves for coincidences between P and the beam hodoscope counters could be made as narrow as three nsec. So this timing requirement alone was quite effective at all but the highest momenta of the experiment. As an additional check, to keep two consecutive protons from conspiring to look like a single pion, the signal from P was also delayed to correspond to a proton's time-of-flight and used in anticoincidence in the beam electronic logic.

The second discrimination was effected by requiring a coincidence pulse from the gas-filled threshold Cerenkov counter C_b at the first focus. Up through 3260 MeV/c this counter was filled with ethane

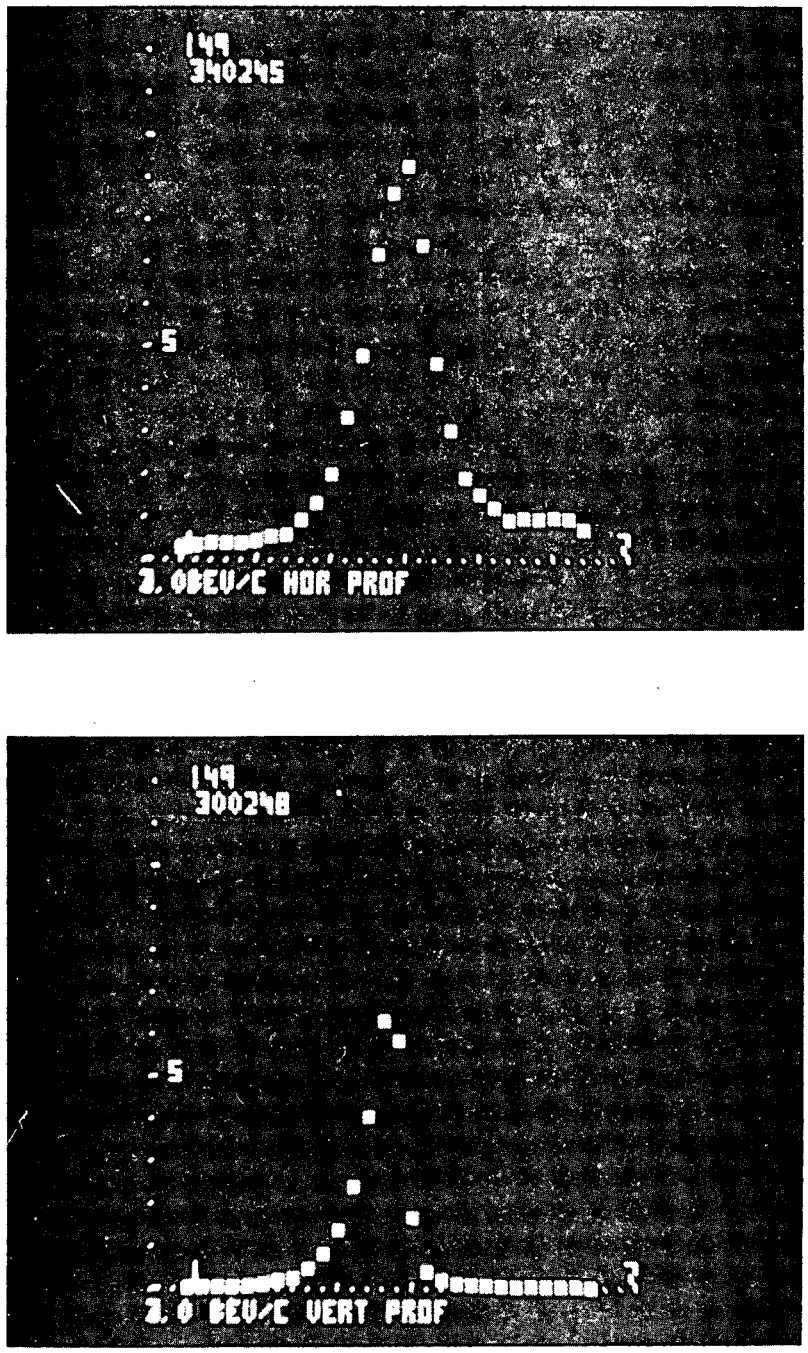

XBB 678-4500

Fig. 4. Horizontal (top) and vertical (bottom) profiles of the pion beam intensity at 3 GeV/c. The plots were drawn by an on-line computer. Each dot represents 1/4 inch in the lab.

(CH_3CH_3) pressurized so that $n > \frac{1}{\beta}$ where n is the index of refraction of the gas and β the velocity of the pion. At the highest momentum nitrogen replaced ethane. The photomultiplier tubes on this counter were equipped with "afterburners", i.e. they were fed by independent power supplies capable of furnishing enough current to these dynodes to keep the tube's output at a constant voltage even at high counting rates. As a result this counter operated reliably even at the highest beam rates available during this experiment--several million pions per Bevatron pulse.

A second much smaller but very troublesome contamination by positrons was discovered partway through the data-taking. A measurement of their abundence at 745 MeV/c, using C_b partially evacuated rather than pressurized, showed it to be less than 1%, but (as will be discussed in Section III) they contributed heavily to the background seen in the final data through much of the experiment. So at the two last momenta to which the beam was tuned towards the end of the experiment, an 1/8-inch lead sheet was placed in the beam at the first focus. This effectively removed the positrons, but had the disadvantage that the difference in energy lost by pions and protons traversing the sheet was sufficient to separate these two components horizontally when they passed through the final bending magnet M_3. This separation was about 1" at the second focus at 745 MeV/c, which was enough to create problems in keeping the pions on target. Also the large proton flux to the side of the target heavily loaded the anticoincidence counter L guarding the left poleface of the polarized target magnet, so data-taking rates

had to be reduced. (The geometry of the target apparatus is discussed in Section III.)

Altogether, though, the fact that pions were distinctly a minority group in the beam population tended to retard the rate of data acquisition, rather than affect the quality of the data. And there were some advantages to having the protons available. Range measurements on them at lower energies at the beginning of the experiment provided a check that the wire-orbit beam momenta were correct. The agreement was within 1%. (Also the wire-orbit measurements were repeated at the end of the experiment. Again, the agreement was within a percent.) And by changing the timing of the beam counters and using C_b in anticoincidence rather than coincidence, it was possible to use the proton beam to measure the polarization parameter in p-p scattering.

The beam conditions during the experiment are summarized in Table I. Data was taken at fifteen momenta, altogether, ranging from 745 to 3747 MeV/c.

Table I. Properties of the pion beams used in this experiment. Δt is the time-of-flight difference between protons and pions from F_1 to the beam hodoscope near F_2. C_b is the ethane-gas-filled (except at 3747 MeV/c) Cerenkov counter at F_1. Where there is no entry, the quantity was neither used in the experimental logic nor measured directly.

Momentum P_π(MeV/c)	K.E. T_π(MeV)	C.m. energy M(MeV)	Δt (nsec)	C_b pressure (psig)	p:π ratio
745	618	1524	25		1:1
895	766	1612	19		4:3
1024	894	1685	16		3:2
1084	953	1718	15		
1155	1024	1756	13	165	2:1
1284	1152	1823	11	135	2:1
1352	1220	1857	10	128	
1441	1308	1902		120	
1570	1437	1964	7	107	
1690	1556	2020		95	
1869	1735	2102		80	
1988	1853	2154	4	73	
2535	2399	2380		56	
3260	3123	2650		46	
3747	3610	2817		125 N_2	4:1

C. Polarized Target

The details of the polarized target have been described adequately elsewhere,[38] so only a brief description will be given here. In this experiment the target was an approximately one-inch cube composed of four crystals of neodymium-doped lanthanum magnesium nitrate, abbreviated LMN [$La_2Mg_3(NO_3)_{12}\cdot 24H_2O$]. The free protons in the hydrogen of the waters of hydration, 3% of the mass of the crystal, were polarized by the process of dynamic nuclear orientation.[40]

The crystals were cooled in liquid helium pumped down to 1° K and placed in a horizontally aligned magnetic field of 18.5 kgauss. In this environment the paramagnetic neodymium ions are over 90% polarized and behave analagously to free electrons. The crystals are then irradiated with microwaves to transfer this high polarization of the "electrons" to the free protons in the target. Depending on which of two nearly equal frequencies is used, the resulting proton polarization is either parallel to or antiparallel to that of the "electrons". In the target magnetic field of this experiment these frequencies are about 70 GHz and differ by about 0.2%, or 150 MHz. Periodic reversal of the proton polarization is obtained simply by changing from one frequency to the other.

Theoretically the "electron" polarization can be almost entirely transferred to the protons, but in practice things are less ideal. The average of the absolute value of the polarization of the target protons in this experiment was 50%. It was measured by the process of nuclear magnetic resonance (NMR) by observing, effectively, the amount

of energy exchanged between the proton spin and an applied weak field. This exchange slightly depolarizes the protons, but, if the depolarization is kept small enough, its sign and magnitude are proportional to the target protons' average polarization.

During the time of data acquisition when the microwaves were on and the target highly polarized, this NMR signal was constantly monitored as a check that the target polarization was maximal and steady. Periodically -- about once every ten minutes -- it was recorded for later use in calculating the actual value of the target polarization. This calculation was based on comparison of the size of the NMR signal obtained when the polarization of the target's free protons was enhanced by the microwave pumping to the size of the NMR signal obtained when those protons were allowed to come to thermal equilibrium with their environment without the microwaves. These latter "T E" signals were recorded about every twelve hours and served as a continually updated calibration of the polarization measurement system.

At six of the beam momenta used in this experiment data were also taken with the LMN crystal target replaced by one of comparable heavy-element composition but containing no free hydrogen. This "dummy" target data was used to estimate the amount of background to be subtracted from the real crystal data before calculation of the final results. (See Section III-B-5) The dummy target itself was composed of a mixture of MgF_2, $BaCO_3$, and CF_2:CF_2 (teflon), dried to remove all water and combined in a proportion to match that of the atomic weights in the LMN crystal.

D. Scintillation Counter Arrays

Six different arrays of counters were combined into three hodoscopes surrounding the target to observe the geometry of the πp interactions. One hodoscope monitored the incoming pion direction; the other two, the final state particles' directions. Their arrangement relative to the polarized target is shown in Fig. 5, and a dimensioned projection of each hodoscope in Fig. 6. The coordinate convention used throughout is right-handed, centered at the target, and with +Z axis along the beam direction and the +Y axis vertically upward. Thus, looking downstream, the X cartesian coordinate increases from left to right, the Y cartesian coordinate from bottom to top. Similarily, above and below the beam the polar angle θ principally defines the vertical lab coordinate and the azimuthal angle φ the horizontal. The counter arrays are named according to this convention.

The beam hodoscope was a 3×3 arrangement of counters placed perpendicular to the beam and to each other and named X_1 through X_3 and Y_1 through Y_3 according to whether they defined the incoming beam particles' X or Y cartesian coordinate eight feet upstream of the target.

The two final-state hodoscopes, one above and one below the beam, were composed of five arrays of counters, and each hodoscope determined the direction of an outgoing scattered particle. According to the coordinate convention mentioned above, the bins in these arrays

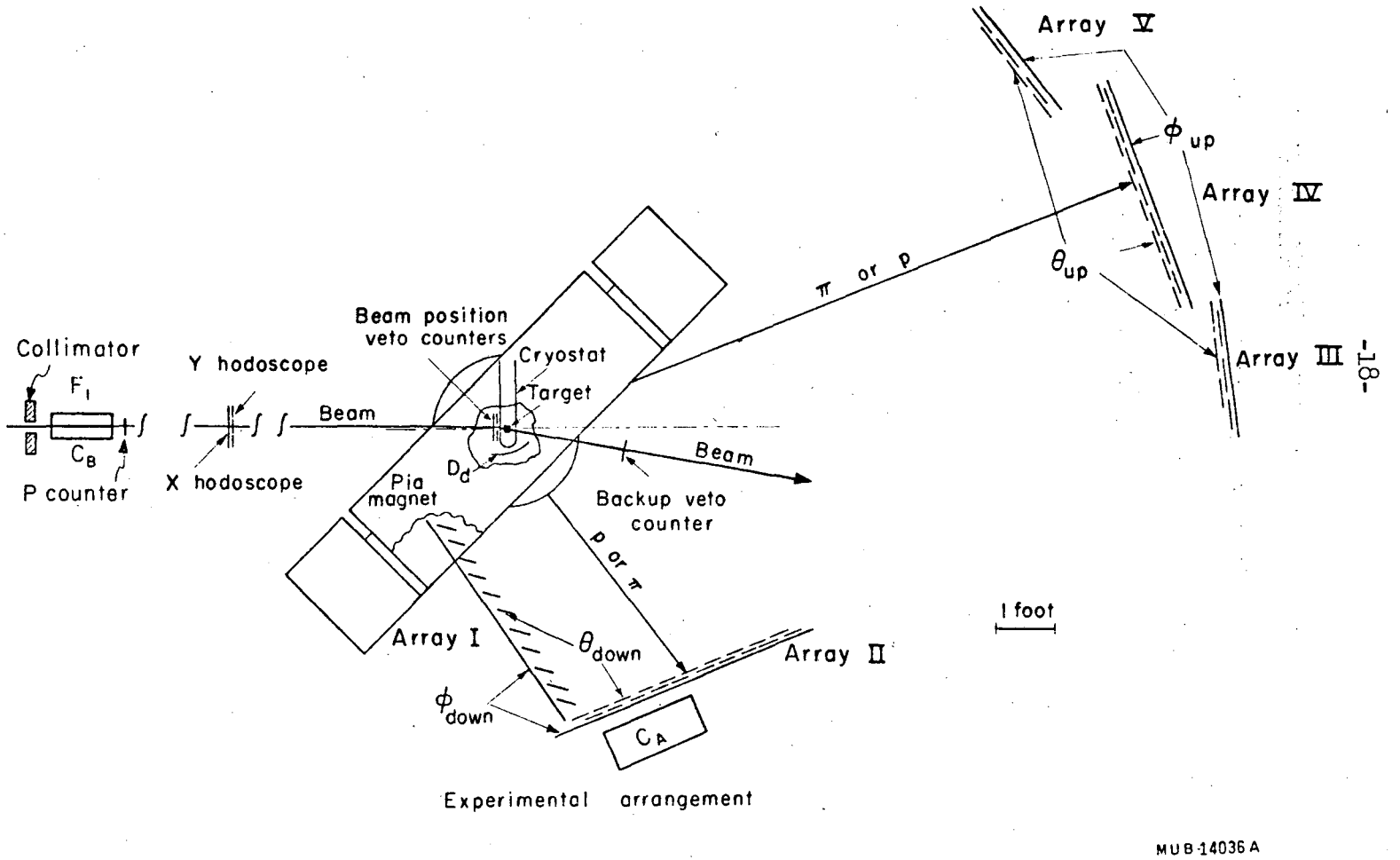

Experimental arrangement

Fig. 5.

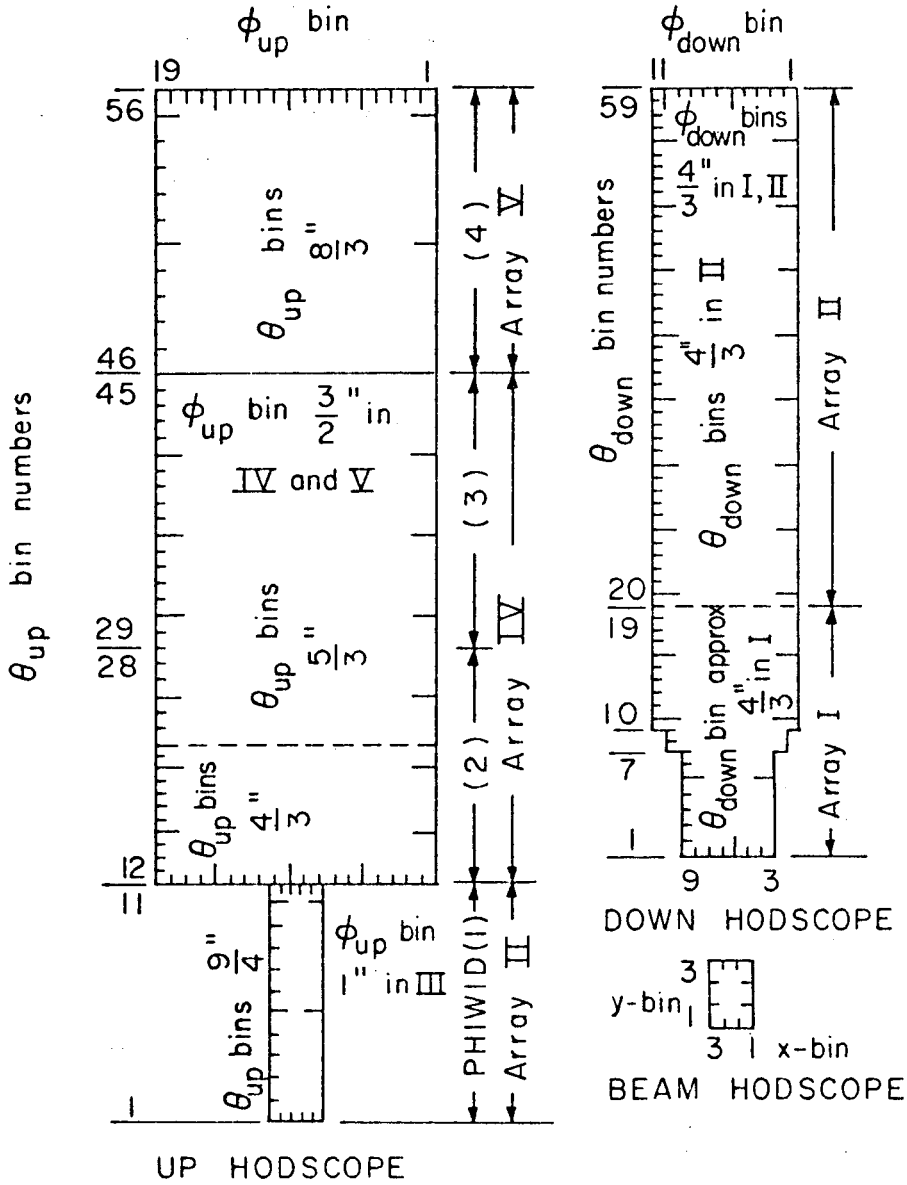

XBL677-3674

Fig. 6. Dimensions and numbering of the hodoscope counters.

were called θ_{up} , θ_{down} , φ_{up} , φ_{down} . The polarized target magnet gap imposed the geometry that the arrays overall were narrow horizontally and wide vertically, so the θ_{up}-θ_{down} correlation determined the lab opening-angle of the final state particles, and the X-Y-φ_{up}-φ_{down} correlation, their coplanarity. As shown in Figs. 5 and 6, each of these arrays was composed of fairly long, thin counters arranged so that in its thin dimension each generally overlapped 1/3 of its neighbor. By separating the events in which two adjacent counters fired simultaneously from those in which only one fired, the distinguishable number of bins into which events could be classified in a given dimension was made almost double the number of counters monitoring that dimension.

Positioned horizontally in the two hodoscopes there were altogether 30 θ_{down} counters, overlapped to provide 59 θ_{down} bins; and 30 θ_{up} counters, overlapped, except in three cases, to provide 56 θ_{up} bins. In the polar direction below and above the beam the physical size of each hodoscope was too great to be spanned by a single counter of reasonable length, so the azimuthal-angle-defining counters in the up and down hodoscopes were physically divided into series of two or three counters placed end-to-end. The outputs of these counters were combined electronically to produce, effectively, 13 φ_{down} and 19 φ_{up} bins.

The size of the bins in each array was chosen to give the best angular resolution consistent with the effects of multiple Coulomb scattering and finite target size. With the exception of Array III, the lowest third of the upper hodoscope which was inherited from a previous experiment, the lengths of the θ-counters were chosen so that in their positions shown in Fig. 4 they covered the entire solid angle downstream from the target into which particles could scatter without hitting the target magnet. The total lab solid angle subtended by the final-state hodoscopes was about .09 steradians by the upper arrays and .33 steradians by the lower.

The entire upper hodoscope was mounted on rails so it could be moved back to give more exact measurement of the angle of forward-scattered particles at higher momenta. This option was used only once, however, at 3260 MeV/c.

Besides the hodoscope counters there were a number of special-purpose counters involved in the experiment. Upstream from the target and immediately in front of the cryostat were four small veto counters called L, R, T, and B (for left, right, top, and bottom) which limited acceptable incoming particles to the actual target area: about one square inch. These counters helped keep events originating in the side walls of the cryostat or magnet pole tips from adding to the background. They also provided a convenient continuous monitor of the beam position while data were being taken. The standard prodcedure was every few hours to place an X-ray film in the beam downstream from the target.

A few minutes' exposure was sufficient to show the shadow of the target. If the beam was well centered, during subsequent data-taking the magnets M_1 and M_4 were tuned to keep the counting rate ratios R/L and T/B constant.

Another pair of veto counters R_p and L_p lay flat against the magnet pole faces behind and to the sides of the target. These also protected against events originating in the magnet iron, but more important helped eliminate inelastic events with multi-particle final states in which one particle came out sideways. They were installed about half-way through the experiment and made a marked improvement in background suppression.

The final veto counter, B_u for Backup, was in the beam downstream of the target magnet and helped eliminate both accidental triggers in which a beam particle did not scatter and multi-particle inelastic events with one particle coming off very forward. Its position was adjusted to compensate for the variations in beam deflection in the target magnetic field as that field or the beam momentum was changed.

Immediately below and behind the target was a small counter D_d (down-defining) used in coincidence with the lower arrays to distinguish particles which came from the target region. The size of the arrays was such that even with all the veto counters, this additional coincidence was an important help. It also, in conjunction with the beam electronics, served to define a definite event time, against which the trigger logic could compare pulses from the arrays for proper time

of flight from target to array, time of counter response, etc.

Finally, beneath the down array was a large water-filled Cerenkov counter C_a. This was used to distinguish whether it was the pion or proton which scattered downward at that angle where the kinematics were ambiguous.

The dimensions and electronics associated with the various counters are summarized in Table II.

Table II. Scintillation counter dimensions and electronics.

Counter or Array	Dimension	Number	Size of Scintillator (inches)	Scintillator Type	Photomultiplier Type
V_{up}	θ	4	30x8x1/4	Pilot B	6655A
V_{up}	θ	2	30x5-1/3x1/4	Pilot B	6655A
V_{up}	φ	8	30x4-1/2x1/4	Pilot B	6810A
V_{up}	φ	2	30x3x1/4	Pilot B	6810A
IV_{up}	θ	10	30x5x1/4	Pilot B	6655A
IV_{up}	θ	2	30x3-1/3x1/4	Pilot B	6655A
IV_{up}	θ	4	30x4x1/4	Pilot B	6655A
IV_{up}	θ	2	30x2-2/3x1/4	Pilot B	6655A
IV_{up}	φ	8	55x4-1/2x1/4	Pilot Y	6810A
IV_{up}	φ	2	55x3x1/4	Pilot Y	6810A
III_{up}	θ	4	5x6-3/4x1/4	Pilot B	6655A
III_{up}	θ	2	5x4-1/4x1/4	Pilot B	6655A
III_{up}	φ	5	1x25x1/4	Pilot B	6655A
II_{down}	θ	19	16x4x1/4	Pilot B	2067
II_{down}	θ	1	16x2-2/3x1/4	Pilot B	2067
II_{down}	φ	4	55x4x1/4	Pilot Y	6810A
II_{down}	φ	2	55x2-2/3x1/4	Pilot Y	6810A
I_{down}	θ	5	16x4x1/4	Pilot B	6655A
I_{down}	θ	1	10x5x1/4	Pilot B	6655A
I_{down}	θ	3	8x6x1/4	Pilot B	6655A
I_{down}	θ	1	8x4x1/4	Pilot B	6655A
I_{down}	φ	4	55x4x1/4	Pilot Y	6810A
I_{down}	φ	2	27-1/2x2-2/3x1/4	Pilot Y	6810A
X_{beam}	X	3	7-1/4x1-1/3x1/8	Pilot B	6655A
Y_{beam}	Y	3	4-1/4x2-1/3x1/8	Pilot B	6810A

(continued on next page)

Table II. Scintillation counter dimensions and electronics. (continued)

Counter or Array	Number	Size of Scintillator (inches)	Scintillator Type	Photomultiplier Type
C_a	1	19x24x5	water	6-7046's
C_b	1	8" diam., 24" long	ethane or nitrogen	2-7046's
T	1	2x2x1/4	Pilot B	6655A
L,R	2	1x6x1/4	Pilot B	6655A
B	1	2x4x1/4	Pilot B	6655A
D_d	1	10x2-1/4x1/4	Pilot B	6810A
P	1	6x3x1/8	Pilot B	6810A
P_R,P_L	2	20x6x1/4	Pilot B	6810A
B_u	1	14x6x1/4	Pilot B	6810A

E. System Electronics and Programming

1. General Description

Figure 7 is a block diagram of the overall system. Array counter pulses were stored in delay lines while the fast (nanoseconds) electronics compared timing of signals from the various sources to decide if an acceptable event had probably occurred. If the decision was yes, coincidence gates at the ends of the delay lines were opened in time for the array counter signals to set short memory flip-flops (SMFF's). Then at computer-electronics speeds (microseconds) the binary information in these flip-flops, one bit per array counter, was transferred to the core memory of an on-line PDP-5 computer. When the transfer was complete, the SMFF's and trigger circuitry was reset to watch for another event. During the time it was not actually having an event loaded into its core, the PDP-5 was programmed to decode the binary counter information, to check for the event's validity, and between Bevatron pulses to write the events accumulated during the previous pulse onto magnetic tape for future, more sophisticated processing. It also performed various supervisory and summarizing functions to control the flow of data and give the experimenter a real-time survey of how the data looked.

Up to 128 events could be accepted during one 800/msec Bevatron pulse. (Typical trigger rates actually observed are listed in Table 1.) It took about 80 nsec for the fast trigger to decide on one event's possible validity, 60 μsec to load it into computer core, and 10 msec for the computer to check its actual validity and recode it for future processing.

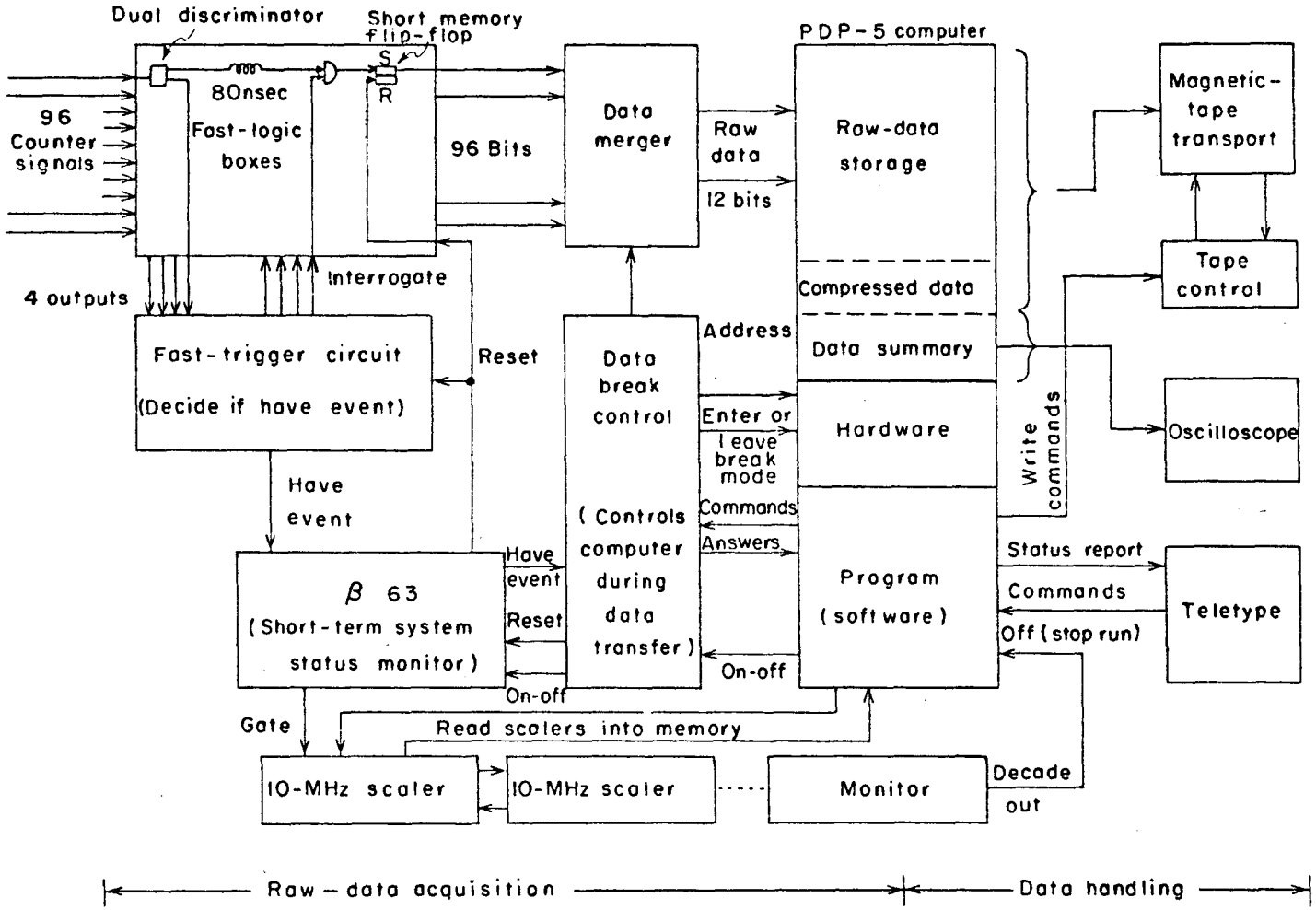

Fig. 7. Block diagram of the system electronics.

The between-pulse transfer of an entire core load of encoded events onto magnetic tape took .75 sec.

More complete discussion of these various functions is in the following paragraphs.

2. The Fast Electronics

A detailed schematic of the fast electronics is shown in Fig. 8. Overall, the coincidence requirements for a trigger were:

1) The beam Cerenkov counter pulse C_b had to be present to signal that a beam particle had been involved which had sufficiently high velocity to be a pion.

2) The first-focus counter P and each dimension of the X-Y beam hodoscope near the second focus had all three to fire with timing appropriate to the velocity of a pion with the momentum to which the beam was tuned.

3) The delayed P signal, P_d, could not be present since this was a warning that a proton had passed the first focus at a time which would permit it to confuse the final event.

4) None of the beam-position veto counters L, R, T, or B in front of the target could fire, or else the beam particle might not have hit the polarized target crystal.

5) Neither of the target magnet pole-face veto counters P_R or P_L could fire, or else some particle might have scattered sideways to invalidate the event.

6) A signal from the down-defining counter D_d was required to

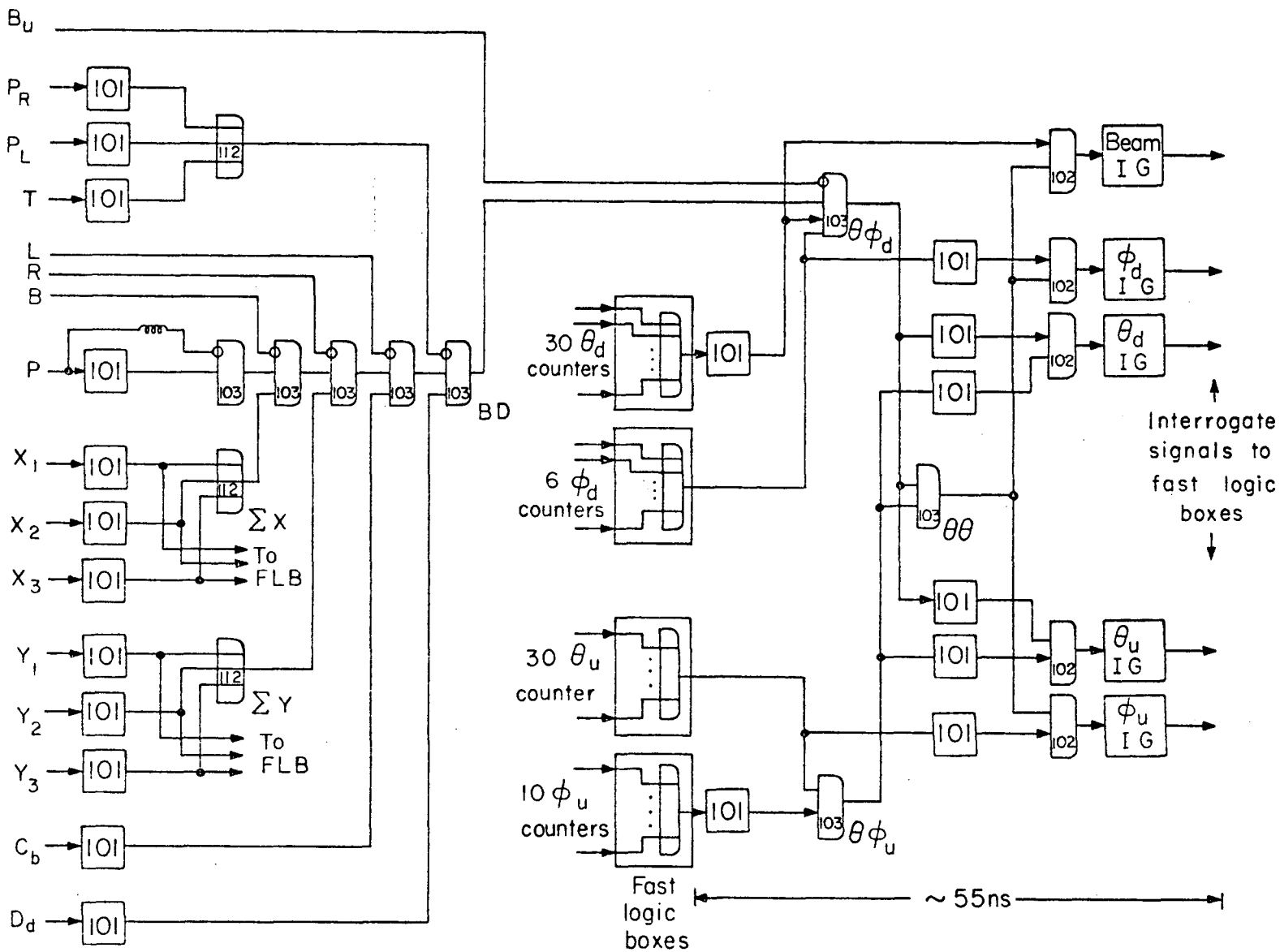

Fig. 8. Detailed block diagram of the fast electronics.

be present to prove that some particle had scattered from the target area into the lower array.

7) The veto counter, B_u, in the beam line behind the target was not allowed to fire. This guaranteed that two beam particles very close together had not been involved and that an inelastic event with one particle going very forward had not occurred.

8) Each dimension of each of the two final-state hodoscopes had to fire. Thus a pulse was required from at least one of each of the θ_{up}, θ_{down}, φ_{up}, and φ_{down} counters. The timing of these pulses depended on the times-of-flight of the final-state particles from the target to the arrays and on the response time of the counters involved. Hence it was necessary for the logic to distinguish among the times at which each array fired and to "remember" these times' relations to each other. In the discussion below the relative timing of these signals, referenced to a basic time fixed by the beam particle involved in each event, is referred to as θ_u-time, θ_d-time, etc.

Discussion of these coincidence requirements can be divided between those referring to the beam and those referring to the final-state particles.

The beam logic is simple and was discussed briefly in Section II-B. Each of the counters involved was equipped with an afterburner and adjusted to deliver .3-.5 volts to its discriminator, a Chronetics

Model 101 with output clipped by a six-inch line. The signals from X1-X3 and Y1-Y3 were added actively in the OR gates "ΣX" and "ΣY" and simultaneously stored individually on delay lines in one of the fast logic boxes. A "beam" signal B was a coincidence $P \cdot \Sigma X \cdot \Sigma Y \cdot C_b \cdot \bar{P}_d \cdot \bar{L} \cdot \bar{R} \cdot \bar{T} \cdot \bar{B}$, and the input to the final-state array logic which defined an event's time was the coincidence $BD = B \cdot D_d \cdot \bar{P}_R \cdot \bar{P}_L$.

The array fast logic was complicated by the appreciable times of flight and counter lengths involved. The essential coincidence desired was $BD \cdot \theta_{up} \cdot \varphi_{up} \cdot \theta_{down} \cdot \varphi_{down} \cdot (C_a \text{ or } \bar{C}_a)$, but the amount of freedom to be allowed in this coincidence varied from signal to signal. Also the interrogate signals which the trigger was required to return to the fast logic boxes had to be timed properly if they were to allow the array counter signals to set their short-memory flip-flops. These interrogate pulses were shortened to a 15 nsec width to help reduce the number of triggers in which two SMFF's for a given hodoscope dimension might get accidntally set. So the trigger was designed to remember five different times: BD time, the time 60 nsec after which the X-Y FLB was to be interrogated, and analogously, $\theta_d$time, $\theta_u$time, $\varphi_d$time and φ_u time. Furthermore the θ-φ coincidences in each of the up and the down hodoscopes had to be allowed to vary over times determined by the counter lengths and photomultiplier response, while the up-down hodoscope coincidence requirement had to be more lenient since it had to allow for the time-of-flight from target to hodoscope

which varied with angle and whether the pion went up or down.

These are the reasons for the series of AND gates building up to the final coincidence decision. First each hodoscope had to fire in the sense that its φ and θ pulses were coincident to within ± 8 nsec at the $\theta\varphi$up and $\theta\varphi$down gates. In addition, the down hodoscope, which was closer to the target and subject to less target-to-array time-of-flight jitter, was required to be in coincidence with BD to within a constant, ± 8 nsec. Then the up and down hodoscopes had to be coincident to within ± 15 nsec at the $\theta\theta$ gate, so named because the θ pulses were used to define the hodoscope time since their counters were physically shorter. The $\theta\theta$ coincidence was the decisive permit to trigger the event and so opened the final gates for the five array-timed pulses to trigger their respective interrogate-pulse generators. These in turn loaded the SMFF's and notified the computer that an event was waiting to be loaded into core.

3. On-Line Computing System

This microsecond-speed part of the experiment's electronics was built around the PDP-5, a small programmable computer. It has a core memory of 4096 12-bit words and a programming structure built around eight basic commands. It also has a program interrupt facility, which allowed various external devices to ask for special attention during the execution of its main program. The action required by such interrupts was itself programmed into the computer and was executed like any other part of its program. Depending on the nature of such

an interrupt, after it was serviced, control was returned to the main program in various ways. The binary counter information of each fast-logic triggered event was transferred into core through another facility, called the data break. When a data break occurred, execution of the regular program can be more accurately described as suspended than interrupted. Control of the computer's memory input and address registers passed to an external device, the Data Break Control (DBC). The DBC loaded the 96 bits of counter information of a single event into a prearranged eight words of core, then returned control to the computer itself and the main program continued with the next instruction.

Besides the DBC, the computer was interfaced with twenty to thirty 10-MHz scalers, two oscilloscopes, a Model-35 ASR Teletype, several external flip-flops and switch registers, and a Datamec Model D2020 magnetic tape transport. The program interrupt facility was used to initiate input from or output to most of these devices.

In general the 10-MHz scalers monitored the fast electronics and advised the computer to take action to change the status of the experiment when certain total counts were reached. E.g., single continuous stretch of data accumulation, a "run", was terminated when, say, 400 million counts had been received from the beam coincidence circuit B. One oscilloscope provided real-time visual display of the experiment's progress to the experimenter. The other was fitted with a Polaroid camera so that graphs of data summaries could be photographed

periodically. The Teletype keyboard was the principal instrument through which the experimenter could input commands to the computer. Conversely, the Teletype printer allowed the computer to output comments and status reports to the experimenter. The flip-flops and switch registers determined, or were determined by, the various external conditions of the experiment--whether a Bevatron beam spill was in progress, what the current beam momentum was, etc. The magnetic tape transport was the ultimate recorder of the information in each scattering event as well as much summary information obtained from scalers and the main program in the course of the run.

The overall block diagram in Fig. 6 shows the major components of the computer system. One not mentioned specifically above is the Data Merger (DMR) which was simply a system of gates which, under the control of the DBC, converted the 96-bit parallel input from the fast logic box SMFF's to a series of eight sequential 12-bit inputs to the computer memory. Another is "β63" which was used here as a high-speed system status monitor. Basically it supplied the gate signals which signalled whether an event was being watched for, being received and transferred to computer core, or being written onto magnetic tape. It was the instrument by which status commands were relayed to the other apparatus--scalers, fast logic, etc.--external to the computer.

4. Programming

The main advantage in having the PDP5 available was its programmability. This allowed many tasks which would have required special hardware or human effort to be accomplished instead by a combination of computer "software", its program, and standard external devices like the oscilloscopes. Also the same basic system could be operated in different modes, one for beam tuning, another for counter timing, a third for data taking, simply by changing the program and reconnecting a few cables. Finally, periodic use of a system test program enabled the computer to check automatically its own reliability and that of most of the peripheral electronics and also to facilitate repair work when components failed.

The PDP5 program which controlled data acquisition was called Escoffier. It had two primary functions: to write the counter information onto magnetic tape and to keep the experimenter informed of the experiment's progress. In the process of accomplishing the latter, some reduction and validity-checking of the incoming binary counter data was necessary, and so this additional information was also written on magnetic tape to simplify the subsequent analysis.

Specifically, the incoming raw data, 96 bits per event, was converted to a series of six numbers which were coded into twelve octal digits (36 binary bits) and specified which bin had fired in each dimension of each hodoscope. This conversion took into account the overlapping of most of the counters and also checked the event's validity: one and only one bin had to fire in each array. If no bin appeared to have

fired in some array (because the fast electronics had failed to relay some counter pulse into the computer core), the event was classified no-good-zero (NG0); if more than one, as no-good-two (NG2). For each event this validity classification as well as its six bin numbers and 96 bits of raw data all eventually went onto the magnetic tape.

In addition, after each event's decoding, the program retained certain information about it in an area of the computer memory reserved for accumulating summary information. The number of valid events (NG0 or NG2) in each array, the number of times each of the 3+3+59+19+56+11 = 151 bins (See Section II-D) had fired, correlations between counts in the up and down arrays -- all this was remembered to be displayed on the oscilliscope at the experimenter's request. Thus, while the data was being accumulated, it was possible to tell when a scintillation counter failed or when accidental rates changed or how the elastic events from free hydrogen in the target stood out above background.

The program checked for parity errors when it read external scalars into its memory or wrote onto magnetic tape, and a failure of these external devices was communicated to the experimenter via the teletype printer. At certain intervals this printer was also the output for standard summary information -- counting rates, time of day, etc. -- which provided a running log of the experiment's progress.

Control of the program by the experimenter was principally through the teletype keyboard. A variety of some ten commands told the computer to start or stop the counting, rewind the magnetic tape, type out

information, etc. Conversely, the program checked to be sure that the experimenter avoided certain trivial errors like trying to start taking data without readying the magnetic tape transport. This proved a valuable feature and kept the amount of data lost through human error to almost zero.

A simplified diagram of the logic of Escoffier is in Figure 9.

Another program which greatly simplified the task of setting up the experiment was called Herbie. It enabled the computer to accumulate in its memory the data from as many as thirty external scalars and then display various types of graphs of that data on the oscilloscopes. This program was used for beam tuning, counter high-voltage adjusting, counter timing, etc. The beam profiles in Figure 4 are examples of its output. In that instance, 28 scalars had monitored counters in a hodoscope in the beam through one Bevatron pulse, then the counts were read by the computer, normalized, and plotted. Total elapsed time was less than one second.

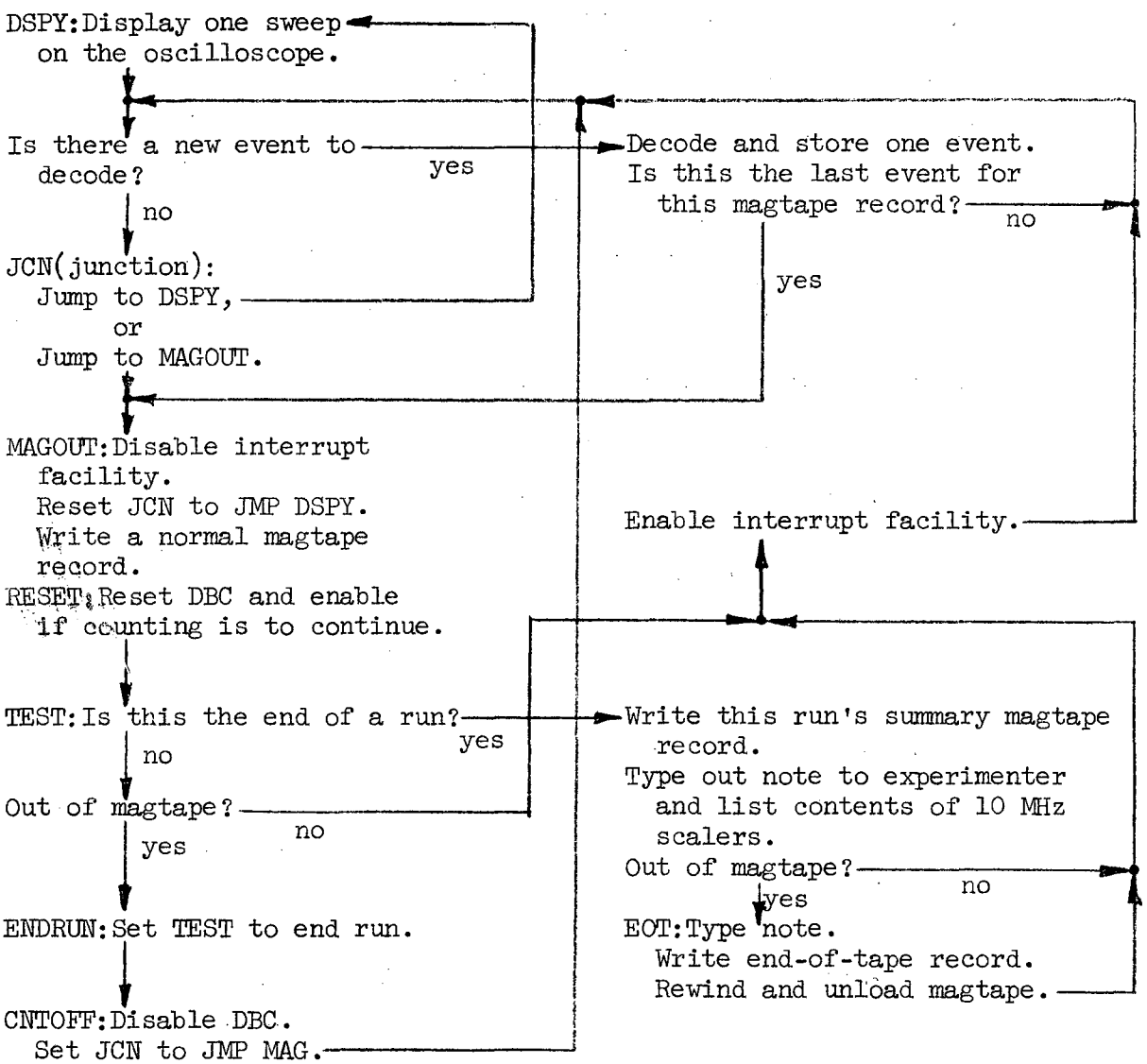

The experimenter controls the computer through its interrupt facility. His commands cause the program to behave essentially as if it has encountered the following instructions:

Start run: jump to RESET
Stop counting: jump to CNTOFF
Resume counting: jump to RESET
End run: jump to ENDRUN
Rewind magtape: jump to EOT

Fig. 9. Logic of the PDP-5 data acquisition program Escoffier.

III. DATA ACQUISITION AND REDUCTION

A. Raw Data Acquisition

Altogether, data for this experiment was accumulated in stages between December, 1965, and March, 1966. During this period polarized-target $\pi^+ p$ data was taken for 65 12-hour Bevatron periods, and filled 43 magnetic tapes with about 12 million events. An additional 13 periods and 10 tapes were used taking dummy-target background data.

Conditions changed several times during this time. The beam Cerenkov counter was installed in January, 1966. The poleface anti-counters P_R and P_L were added in late February, and the positron contamination of the beam eliminated with the lead sheet at the beam's first focus only in the beginning of March. So the data-to-background ratio, counting rates, etc. at different energies often were quite different, and in the case of the positron beam contamination at lower momenta, enough so to effect somewhat the method of the subsequent data reduction as will be discussed below.

In addition, some of the data was taken with the field of polarized target magnet in the "normal" direction, defined to be that direction which bent the positive beam downward, and some with that field reversed. This was to make different center-of-mass angular regions accessible in the lab geometry. But it affected the type of background subtraction used in the data reduction, which also will be discussed below.

Common to all the data-taking, though, was its division into

the 15-to-30-minute periods called "runs" mentioned in Section II-E-4. During each of these periods every effort was made to keep target polarization, beam conditions, counting rates, etc., constant. The run was the basic unit of data for later individual reduction.

Also universal were the practices of reversing the target polarization about every two hours to minimize the effects of any long-term changes in the environment and of taking thermal-equilibrium polarization signals every twelve hours to calibrate the target polarization detection apparatus. Beam, trigger, and accidental rates were monitored continuously and recorded by the computer as explained in Section II-E-4.

In Table III are listed some of the counting conditions and rates as a function of beam momentum. Where there is more than one entry for a given momentum, each entry corresponds to a block of runs which were eventually analyzed together. Comparison of the results from the different blocks and their combination will be discussed below.

Table III. Experimental conditions for each block of data.

Momentum P_π(MeV)	Target magnet polarity	type	Total beam (X10-9)	Rates per pulse beam (X10-3)	triggers	NG2 (%)	Comments
745	normal	xtal	5.3	650	70	22	
	normal	xtal	1.0	460	60	15	
	normal	xtal	2.9	400	45	22	(a)*
895	normal	xtal	6.6	670	37	15	
1024	normal	xtal	2.9	650	50	13	
	normal	xtal	2.5	690	61	15	
	normal	dummy	3.5	550	27	14	
1084	normal	xtal	3.3	440	15	10	(a);(b)*
1155	normal	xtal	3.8	670	65	14	
	reverse	xtal	4.5	360	15	18	
1284	normal	xtal	5.5	660	47	19	
	reverse	xtal	6.0	390	28	19	
	normal	dummy	4.0	680	40	19	
	reverse	dummy	2.9	360	28	20	
1352	normal	xtal	3.8	600	17	13	(a);(b)
1441	normal	xtal	5.6	680	50	21	
	reverse	xtal	3.4	400	37	20	
	reverse	xtal	1.5	480	28	21	
1570	normal	xtal	6.0	1000	63	26	
	reverse	xtal	4.4	500	37	20	
	normal	dummy	4.0	1100	66	24	
1690	normal	xtal	6.0	1000	68	25	
	normal	xtal	4.4	550	26	19	(a)
1869	normal	xtal	5.6	1300	75	27	
	normal	xtal	3.5	370	15	19	(a)
	normal	dummy	5.0	1300	65	25	

(continued on next page)

Table III. Experimental conditions for each block of data. (continued)

Momentum P_π(MeV)	Target magnet polarity	Target type	Total beam (X10-9)	Rates per pulse beam (X10-3)	Rates per pulse triggers	NG2 (%)	Comments
1988	normal	xtal	4.7	1330	70	28	
	normal	xtal	6.3	1900	73	19	
	normal	xtal	8.2	1100	55	20	
2535	normal	xtal	8.6	1800	63	24	
	normal	xtal	14.0	1550	50	22	
3260	normal	xtal	17.2	1500	15	27	(c)*
	normal	dummy	7.8	1500	24	26	(c)
3747	normal	xtal	5.3	400	8	35	(d)*

* (a) Poleface anticounters P_R and P_L were in use.

(b) Lead sheet in beam at F_1.

(c) Up array moved back.

(d) Beam spill length reduced to 200 msec.

B. Data Reduction

1. General Considerations

The six bin numbers written on magnetic tape by the PDP-5 to describe each valid event theoretically could occur in $3 \times 3 \times 59 \times 19 \times 56 \times 11 \simeq 10^7$ possible combinations. Most of these combinations were seldom detected because they would have described events which were hopelessly bad fits to elastic $\pi^+ p$ scattering. But many could correspond to quasi-elastic scattering off one of the unpolarized protons bound in the nucleus of a heavy element in the target. Others could have resulted from inelastic pion-nucleon reactions or even reactions not involving a beam pion at all. Hence the second step was to refine the data on a CDC 6600 computer.

There were several tasks to be accomplished. The 10^7-bin correlation matrix needed to be reduced to manageable size. The background had to be suppressed enough to make it possible to select the true elastic events. The size, shape, and normalization of remaining background had to be determined.

The general principle involved was to use the kinematics of elastic scattering on a fixed target to distinguish the events involving free protons from inelastic events and from those involving bound protons with appreciable Fermi momentum. The beam momentum, the hodoscope and target positions in the lab, and the magnetic field surrounding the target were all known. So for each beam momentum, each pair of beam hodoscope bin numbers, and each pair of upper array bin numbers,

the conjugate lower array bin numbers expected for elastic scattering could be calculated. Each valid event was then compared to this ideal and classified by how well it fit. Finally a judgment was made on how many of the events clustered around the ideal could be considered real and how many background. This comparison and selection process proceeded through the several steps discussed in the rest of this section.

2. Compression of the Correlation Matrix

The overall geometry of the magnet-target-hodoscope system dictated the manner in which the individual counts in the 10^7-bin matrix were summed together into a reasonable-sized correlation scheme which could still show the distribution of events about the free elastic ideal at each angle. Since the four-inch polarized target magnet gap limited detectable scattering principally to the vertical plane in the lab, it was natural to judge events in two steps--first on the basis of their coplanarity, and second on the basis of their opening angle.

The procedure, then, was to select events on the basis of their X, φ_{up}, and φ_{down} coordinates first, since to within the hodoscopes' angular resolution these alone determined coplanarity. Events which were very non-coplanar were eliminated, and what remained was a Y, θ_{up}, θ_{down} correlation matrix. But a change in Y bin number corresponds essentially to a rotation of an event in the vertical plane bisecting the beam and up and down arrays, and then by only a bin or two in the θ_{up} and θ_{down} dimensions. So by adjusting the two θ bin numbers to effect this rotation the Y index of each selected event

was also eliminated, leaving only a θ-θ correlation. (Actually this compression was performed at the very final step, but this was a quirk of the computer programs used.) But for a given θ_{up}, only about half of the bottom array needed to be considered to get a good profile of the event distribution about the elastic opening angle. So the final result was a 56×30 θ_{up}-θ_{down} opening-angle correlation matrix, extracted on the basis of coplanarity.

Actually it was convenient in each scan through the PDP-5 tapes storing the unreduced matrix to divide events into five groups depending on how they satisfied the coplanarity requirement. The middle group consisted of events which fell into what was called φ-φ stripe 3. They were the most coplanar. Groups 2 and 4 contained those events in φ-φ stripes 2 and 4 where the φ_{down} bin slightly failed coplanarity to the beam's right and left, respectively. Events in φ-φ stripes 1 and 5 were grossly non-coplanar to the right and left. Events in stripes 1 and 5 were discarded, but separate 56×30 θ-θ matrices were simultaneously constructed for the other three stripes.

The term "φ-φ stripe" arose because of their appearance in a slice through the original matrix in the φ_{up}-φ_{down} plane. Finite bin and target size, Coulomb scattering, and roundoff errors dictated that in general several φ_{down} bins needed to be considered coplanar to each φ_{up} bin for given θ_{up}, θ_{down}, X, and Y. The result of the computer's actual calculation of one such φ-φ coplanarity correlation is shown in Fig. 10. The widths of the stripes shown there are typical of those

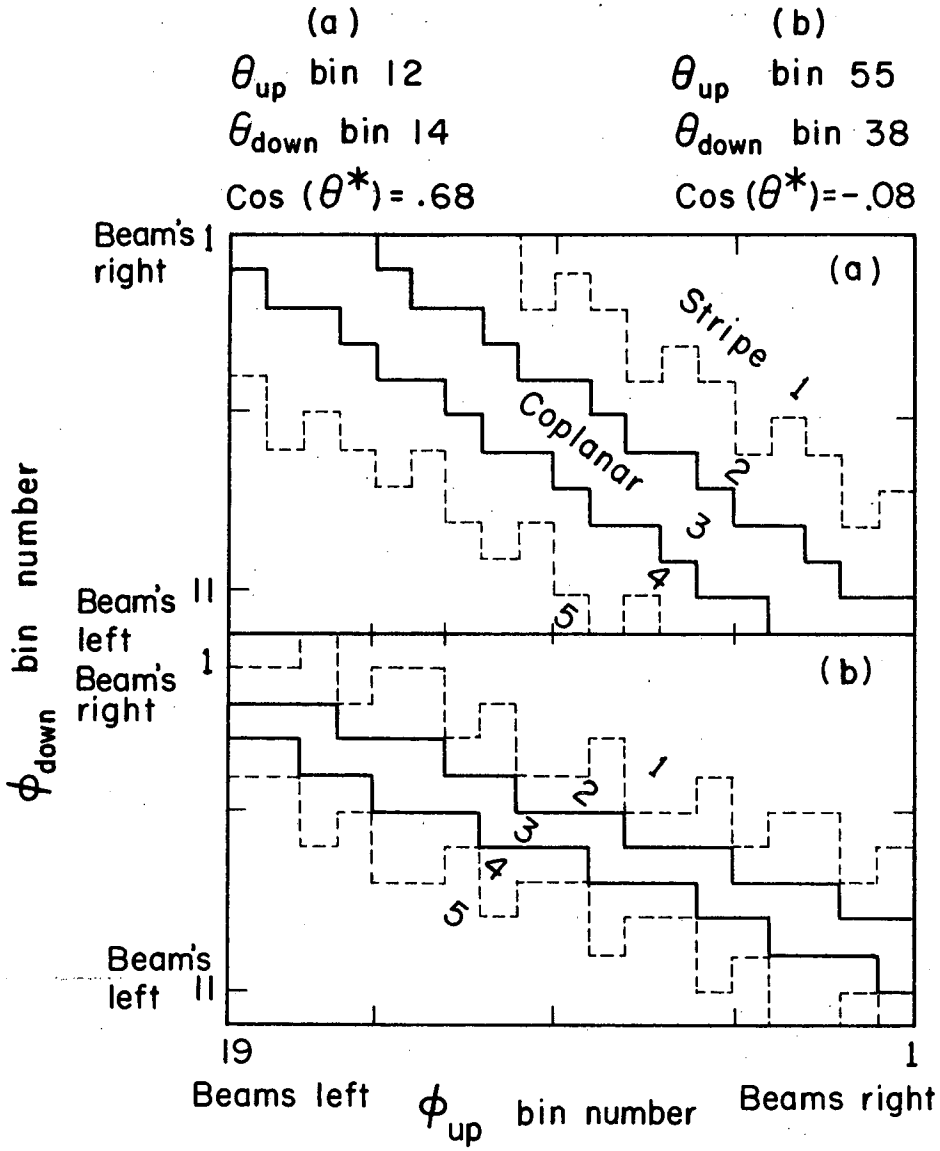

Fig. 10. Typical examples of the φ_{up}-φ_{down} bin correlations required for an event to be coplanar. The meaning and use of "stripe 1", "stripe 2", etc. are explained in the text. The roughness of the dotted lines results from requiring that for each φ_{up} bin, stripes 2, 3, and 4 all have the same width in the φ_{down} direction. In the case shown here, it was assumed that the pion passed through the center X bin of the beam hodoscope and scattered into the up array.

used in practice. The point in explaining this coplanarity treatment in such detail is that the relative appearance of the hydrogen peak in stripes 2, 3, and 4 for given θ_{up} angles was the deciding factor in the background suppression discussed next. The usefulness of this coplanarity-stripes concept lay in the fact that their width and position were programmed to be adjustable. This was one of the main weapons against background.

3. Background Suppression

Using the general reduction process just described, for each block of data in Table III several preliminary surveys were made of the distribution of counts recorded on the PDP-5 tapes. The goal was to suppress the background by making the coplanarity condition as exacting as possible consistent with not losing too many elastic events.

The basic hodoscope dimensions and positions involved in the coplanarity calculation were known from surveys made both before and after the experiment (and found in good agreement). But in the case of the X-hodoscope the flux distribution of the beam made the effective centers of these counters somewhat different from their physical centers and slightly variable from one energy to another.

So the best position to use in the final data reduction was determined experimentally. First the width of the φ-stripes was artificially narrowed so that part of the elastic peak would overflow into stripes 2 and 4. Then the computer scanned the entire block of data, picking out events involving selected θ_{up} bins. For each such

event the coplanarity calculation was done several times using different positions for the X counter involved. Finally the θ_{down} count distributions for each θ_{up} and each position of each X counter were plotted. It was possible to choose to within a quarter inch the position which best centered the elastic peak in stripe 3 for each θ_{up} and each X counter. This best position for a given X was always the same for each θ_{up}, as it should have been, indicating that the arrays were not tilted. The effective center of each X counter defined in this manner was used in subsequent handling of that block of data.

The next step was to determine how narrow the center stripe could be made and still include most of the elastic peak. The parameter determining the stripe width was called PHIWID and was the magnification factor introduced in projecting onto the lower array the conjugate of the θ_{up} bin which fired. Events were in stripe 3 if they fell into any of the θ_{down} bins covered by this projection, in stripe 2 if they fell one projection to the right, etc. This factor was not independent of θ_{up}, so the up array was divided into the four sections shown in Fig. 6 and the best PHIWID determined for each. These PHIWID's were selected in a manner analogous to that of the X positions. The entire block of data was scanned and each event involving selected θ_{up} bins was processed several times using various PHIWIDs. A θ_{down} distribution was plotted for each θ_{up} and each PHIWID, and the best PHIWID chosen on the basis of the peak-to-background ratios in stripe 3.

The final step in this phase of the data reduction was to make

one more scan through the PDP-5 tapes and, using the optimized coplanarity criterion, to construct and record the 56×30 θ_{up}-θ_{down} correlation matrix for each run.

4. Selection of Elastic Events

Then the θ-θ matrices for all runs in a given block of data were summed together and the θ_{down} distribution plotted for each θ_{up}. Usually the elastic peak stood out clearly and the θ_{down} bins containing it could be chosen for the final run-by-run analysis. Sample distributions are shown in Fig. 11. But some comments are needed.

So far, the question of whether it was the pion or proton which went into the upper array has been avoided for simplicity. But usually there was some region of the upper array where either event was possible and a distinction had to be made. In general the conjugate down particle would be expected in different regions of the down array in the two cases. Figure 11 shows instances where both elastic peaks stand out, well separated. In such cases the coplanarity calculation is somewhat different for the two types of events because of the difference in momenta and bending in the target's magnetic field. Still, both particles have the same charge, and the bending is not too great. If both peaks can be seen at all, they are both visible when the coplanarity reduction is done under either assumption. Figure 11, in fact, was obtained using π-up kinematics on all events. The general procedure adopted was to reduce a block of data assuming all pions went up, then if a π-down peak appeared, the whole analysis was repeated with the

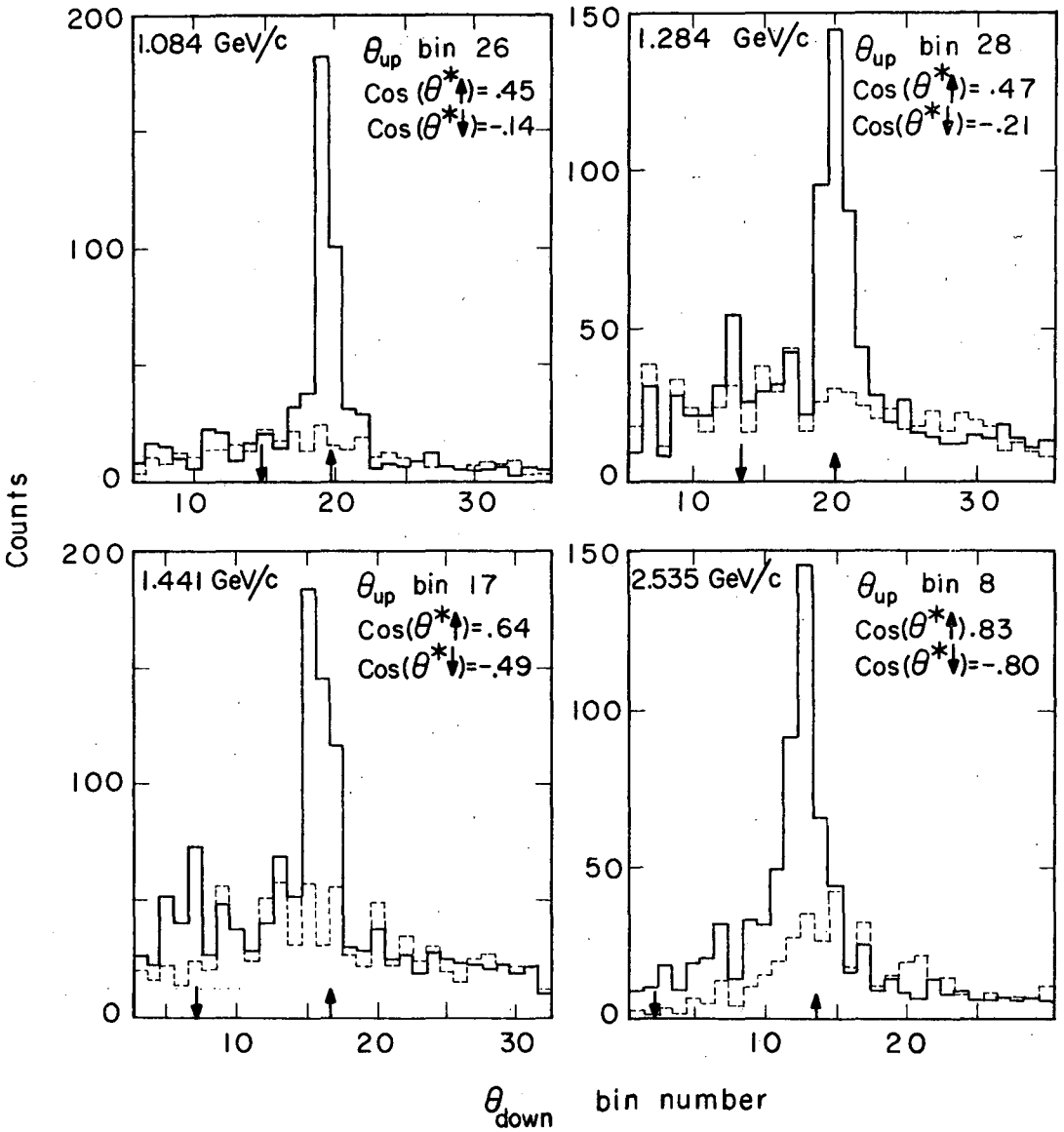

Fig. 11. Typical distributions of counts in the θ_{down} bins for some particular beam momenta and θ_{up} bins. The solid lines are the coplanar events obtained from the polarized target. The dashed lines are normalized estimates of the background, obtained in the 1.284 GeV/c case from a dummy target containing no free protons, and in the other three cases from off-coplanar events from the polarized target. The arrows show the positions of the π_{up} and π_{down} elastic peaks predicted by kinematic calculations.

XBL677-3677

opposite assumption.

There are several reasons why the pions going down never stood out so prominantly as those going up. First, for all but the highest θ_{up} bins the θ_{down} event was more backward in the center-of-mass and thus had generally smaller cross section. Second, those π-down events involving the lower θ_{up} bins had their conjugate protons going into the θ_{down} bins nearest the target where background was always high. (This background was much reduced towards the end of the experiment, though, after the poleface anticounters were installed and the positron beam contamination eliminated. Then more π-down events were visible and data were obtained over a wider range of center-of-mass angles.) Finally, at lower center-of-mass angles with higher π-down cross sections, the transformation to the lab is such that a given θ_{up} bin is conjugate to from two-to five-times as many θ_{down} bins. The elastic peak is more smeared out and tends to be lost in the background. Data at these angles, though, is supplied adequately by π-up events alone.

Even when the π-down peak is not visible, however, its predicted location is of interest because of how the background subtraction was performed. There is further discussion of this below, but the point to be made here is that the subtraction was normalized to the "tails" of the θ_{down} distribution, i.e., the counts in those bins far enough away from the elastic peak to be free of events whose distribution is affected by the polarization of the target. Thus it is important to keep π-down polarization from biasing the π-up background subtraction,

so in choosing the limits of the π-up "tails" care was taken not to include any θ_{down} bins which might reasonably be expected to contain an appreciable fraction of elastic π-down events. And of course π-up background contamination was treated similiarly when subtracting background from π-down elastic peaks.

There remains the more serious problem of when π-up and π-down events are indistinguishable kinematically. When the target's magnetic field was in the normal direction, at each energy there was always some lab angle such that no matter which of the proton or pion went up or down, the same θ_{up} and θ_{down} bins were conjugate for elastic events. In such cases the lab momenta of the proton and pion are equal, and so are the center-of-mass scattering angles for π-up or π-down events.

It is vital to distinguish among such ambiguous events because if there is a non-zero asymmetry at that center-of-mass angle, any wrongly classified events will dilute it. For a given target polarization π-up and π-down events will contribute to opposite sides of the asymmetry. This was the reason for the Cerenkov counter C_a mentioned in Section II-D. The ambiguous angle changed depending on the beam momentum, so C_a was moved to cover the twenty or so θ_{down} bins centered on the critical angle. Whether or not there was a C_a pulse was used to divide events in the questionable θ_{down} bins into two classes. A pion was considered to have gone down only if C_a had fired. This procedure left the π-up asymmetry at the mercy of the efficiency of C_a, but can be justified on several counts. The Cerenkov counter was conservatively

designed and several times was carefully checked to be performing well. At all momenta where either type of event was detectable at this angle, the differential cross-section transformation from center-of-mass to lab always limited the expected ratio of π-down to π-up events to a fairly small fraction (one-half at 2535 MeV/c down to one-fifth at 745 MeV/c). In the few instances where the limited statistics in the π-down elastic peak centered over C_a made an asymmetry calculation meaningful, the result agreed well with the comparable π-up calculation. And finally, at all energies where the polarization parameter was calculated from events classified as π-up simply by the absence of a C_a pulse, its absolute value never displayed an anomalous dip at the ambiguous angle. In spite of these reassurances, though, when the π-up and π-down peaks were nearly but not quite overlapping, the choice of the θ_{down} bins defined to contain the elastic peak was biased away from the ambiguity as an extra precaution, even at the possible expense of some statistics. For instance, if the π-up elastic peak appeared to cover three θ_{down} bins and the center of the π-down peak was predicted to lie only four θ_{down} bins lower than that of the π-up peak, then the counts in the lowest of the three π-up peak bins were not used in the analysis.

5. Background Subtraction

Even after the background suppression discussed above, it was always the case that a significant number of the events in the elastic peak region did not come from free protons. This fraction had to be subtracted from the total, of course, before the asymmetry for scattering

off the polarized protons could be computed. Two basically different methods were used to accomplish this, and they confirmed each other by giving almost identical results.

At some momenta dummy-target data were taken under conditions as closely paralleling those of the polarized-target data as possible. The only difference was that the LMN crystal target was replaced by one of similar heavy-element composition, but containing no free protons. These dummy data were then normalized to the real data as mentioned above by equalizing the total counts in θ_{down} bins well away from the elastic peak region. The total counts in the elastic peak region of the crystal data minus the normalized total counts in the same region of the dummy data was used to calculate the final polarization parameter. (See next section.)

The other subtraction procedure used the non-coplanar events accumulated while the LMN crystal target was in place to estimate the size of the background under the elastic peak. In the terminology of Section III-B-3, the φ-φ stripes 2 and 4 were displaced safely (two or three φ_{down} bins) to the sides of stripe 3, and then whatever events fell into them were considered background. The assumption was that the shape of this background was the same as that which fell into stripe 3. Normalization again was to the total counts in the region away from the elastic peak in the θ-direction.

These two subtraction procedures were compared directly at the six of fifteen momenta where dummy data were taken. (See Table III.)

Except for target-magnet-normal data involving up Array III, the final results were found to be in excellent agreement in every case. Where raw asymmetries were small or zero and peak-to-background ratios good, this was not surprising. But the finding was the same even when there was appreciable asymmetry. As an example, the polarization parameter calculated with each type of background subtraction at 1284 MeV/c is shown in Fig. 12. The conclusion was that at all momenta the background constructed from off-coplnar events was a faithful estimate of the true background except in Array III. As an additional safeguard, regardless of the subtraction method used, the dummy and real data were checked for consistency. It was required that the normalization factors computed from counts in the tails of each θ_{down} distribution on the left and the right and from one θ_{up} to another all agree within statistics for each block of data.

Except in the lowest part of the upper array, these criteria were always reasonably satisfied. The trouble with the lower θ_{up} bins resulted from their narrowness in the φ_{up} direction (Fig. 6), combined with the fact that when the target magnetic field was in the normal direction they were usually conjugate to θ_{down} bins inside the magnet gap and thus also narrow in the φ_{down} direction. This made it impossible to detect enough non-coplanar events to estimate background from the non-coplanar events alone. When dummy-target background data were available, there was no problem. Likewise, with the target magnetic field reversed these θ_{up} bins were conjugate to the

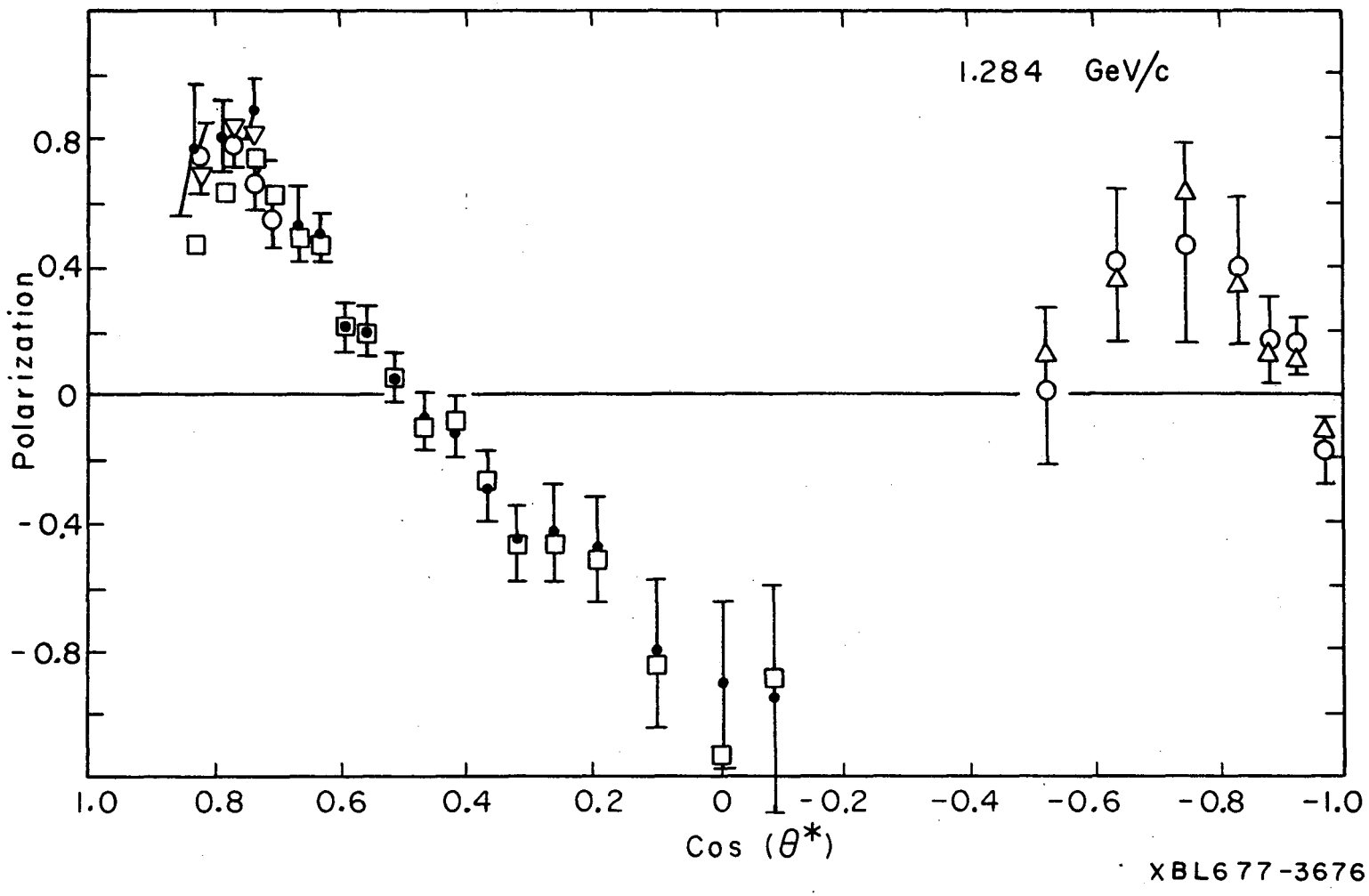

Fig. 12. Comparison of the results obtained at 1.284 GeV/c with the two polarities of the target magnetic field and two methods of background subtraction. The dots are normal field and dummy target background; squares, normal field and off-coplanar background; triangles, reverse field and dummy target background; circles, reverse field and off-coplanar background.

wide section of the down array where non-coplanar counters existed, and there was no problem. But with the target field normal if only the off-coplanar events were used to estimate background, the estimate was usually unreasonably low. The solution adopted was to estimate the background under the elastic peaks conjugate to the eleven lowest θ_{up} bins by direct inspection of the θ_{down} distribution plots. The reliability of this more subjective treatment was supported by its good agreement with the real target results and by data taken at some momenta with the target magnet reversed. Figure 12 also compares results obtained with these two signs of the target magnetic field. Note the better agreement between results of dummy-target and off-coplanar background subtraction when the target magnet was reversed and Array III not involved.

A particularly annoying background problem experienced at low momenta early in the experiment was the result of a positron contamination of the beam. Although relatively few such particles hit the target, that target constituted 1/3 radiation length of material, and so those which did stood an appreciable chance of creating a bremsstrahlung gamma ray which would convert to an electron-positron pair. These final particles had momenta nearly colinear with the beam, so the target's horizontal magnetic field deflected one of them into each hodoscope. The resulting "event" was almost exactly in the vertical plane bisecting the arrays and so was automatically coplanar. The background contributed in this way was especially troublesome because its shape could not be estimated from non-coplanar events alone.

At momenta above 1 GeV/c there were too few positrons in the beam to be worrisome, and after the lead sheet was inserted at the first focus there were essentially none at any momenta. But at the two lowest momenta reported here, this background had to be reduced artificially if the data were to be useful at more than a very few angles. The solution was to ignore events in or very near the vertical plane, both in summing the counts in the elastic peak and in computing the background from non-coplanar events. In effect the middle three of the φ_{up} bins and middle three of the φ_{down} bins were turned off. This discarded a good fraction of the real elastic events but almost all of the electron "events". An example of the net improvement obtained is shown in Fig. 13. The resulting good peak-to-background ratios and consistency in normalizing the off-coplanar background to the non-elastic peak regions support the validity of the final results obtained this way.

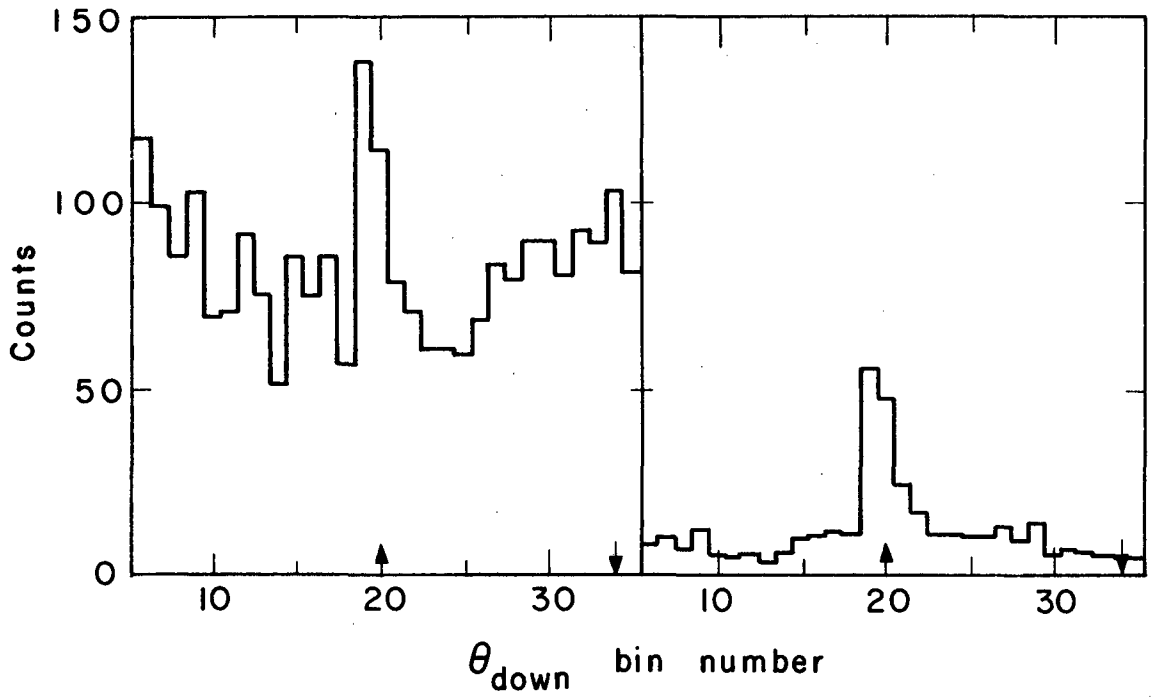

XBL677-3679

Fig. 13. Distributions of coplanar θ_{down} counts obtained before (left) and after (right) suppressing the center three φ bins to reduce the background caused by positron contamination in the beam. The data shown are for θ_{up} bins 40 and 41, summed together, ($\cos\theta_{cm}$=.15 for π_{up} events) and were taken at 745 MeV/c before a lead sheet was placed in the beam at F_1.

C. Calculation of the Polarization Parameter

1. Mathematical Procedure

Use of the simple expressions (II-3 and II-4) was somewhat complicated in practice by the problems of background subtraction and of combining the results from the different runs in one block of data. In this section the formulae actually used to compute the polarization parameter P and its statistical error ΔP will be explained.

Just as a block of runs was the basic collection of data to be analyzed together, the run itself was the basic collection of counts to be considered together. We will adopt the following conventions and notation:

The subscripts i and j will vary with run number. i will refer to runs being used for their hydrogen counts and j to runs being used to calculate background. (When the off-coplanar method discussed in the last section is used to estimate background, i and j can actually refer to the same run, but in different contexts. When dummy-target data is used, the hydrogen and background runs are physically distinct.)

The subscript k and c.m. angle θ (or θ_k) will vary with θ_{up} bin number.

$N_{ik}=N_i(\theta_k)$ is the total number of coplanar counts for the i^{th} run of real crystal data in those θ_{down} bins of the 56 x 30 correlation matrix which have been selected as defining the elastic peak region for θ_{up} bin k at angle θ_k.

$D_{jk}=D_j(\theta_k)$ is the analogous number of coplanar elastic-peak-region counts for the j^{th} run of dummy target data, or of the off-coplanar elastic peak region counts of simulated dummy, depending on which type of background subtraction is to be used.

M_i is the number of monitor counts for the i^{th} run of crystal data;

M_j is the number of monitor counts for the j^{th} run of dummy data, or simulated dummy data. M_i or M_j is the total counts in the non-elastic-peak region of the 56x30 θ-θ matrix for run i or j. Specifically, for each θ_{up}, the θ_{down} counts are first summed over all the θ_{down} bins which are safely non-conjugate to that θ_{up} for elastic π_{up} or π_{down} events. Then these numbers are summed over all the θ_{up} bins for run i or j to get M_i or M_j. All M_i and those M_j corresponding to dummy-target runs are calculated from coplanar events, since that is the way the θ-θ matrix is constructed. The M_j of simulated dummy runs, however, are calculated from the same off-coplanar region in the φ direction that is used to construct the D_{jk}. Thus in general $M_i \neq M_j$, even if i and j refer to the same physical run.

p_i is the algebraic value of the target polarization during the i^{th} run. p_i is positive when $\vec{P}_T$ is parallel to $\hat{n}$, negative when antiparallel.

A basic assumption underlying the background subtraction method is that the shape of the background is the same for the whole block of runs being analyzed together; only its size should vary from run to run, and then in proportion to the monitor. So for each k (θ_{up} bin) under the hydrogen peak there is a unique amount of background per unit monitor, given by

$$b_k = \frac{\sum_j D_{jk}}{\sum_j M_j} \qquad \text{(III-1)}$$

From this one predicts the actual background at angle k in a particular run i to be

$$B_{ik} = M_i b_k \ . \qquad \text{(III-2)}$$

And so the number of events coming from free hydrogen, normalized to unit monitor, is

$$H_{ik} = \frac{N_{ik} - B_{ik}}{M_i} \ . \qquad \text{(III-3)}$$

This is the counting rate which is related to the polarization parameter according to Eq. (II-2) by

$$H_{ik} = I_o(\theta_k)(1 + p_i \ P(\theta_k)) \ . \qquad \text{(III-4)}$$

Now p_i and H_{ik} vary with i, so the method of least squares is used to solve Eq. (III-4) for a single value of $P(\theta_k)$ for the whole block of runs i. The quantity to be minimized with respect to I_o and P is

$$J = \sum_i M_i \ (H_i - I_o - p_i \ I_o P)^2 \qquad \text{(III-5)}$$

where the factor M_i is included to give proper statistical weight to the i^{th} run, and the subscripts j have been suppressed for clarity. The conditions for a minimum are

$$\frac{\partial J}{\partial P} = \frac{\partial J}{\partial (I_o P)} = 0 \ . \qquad \text{(III-6)}$$

From Eq. (III-6) it is straightforward to relate P and the statistical error ΔP to the various counting rates mentioned above. The details are given in the Appendix.

2. Consistency Checks and Data Combination

Though the number of different blocks of data listed in Table III complicated the process of calculating the final results, it did serve to provide a variety of consistency checks on those results. In fact at only four of the fifteen momenta was there no comparison possible between results of data taken in independent blocks. At the other momenta the variations in experimental conditions among the different blocks of data allowed several types of consistency checks.

At each of the momenta 745, 1024, 1690, 1869, 1988, and 2535 MeV/c there were at least two distinct periods of data-taking each involving the same target magnet polarity and lab geometry. The results of such separate periods of running should agree at all angles for each beam momentum. This was checked and found to be so, within statistical fluctuations, in every case. In about half of these cases, experimental conditions other than the geometry had been changed somewhat between the times the different blocks of data were accumuled. For instance, at

1690 and 1869 MeV/c, the poleface anticounters P_R and P_L were installed between the two times data were taken at each momentum. Though this sort of change usually affected the quality of the data--in signal-to-noise ratios, for instance--in no case did it significantly change the result of the final calculation of the polarization parameter.

At each of the momenta 1155, 1284, 1441, and 1570 MeV/c, data were taken with both polarities of the target magnetic field. The primary reason for this was to make events at backward center-of-mass angles visible by bending the positive final-state particles upward in the lab. This deflected backscattered pions into the lower Array I. But it also allowed forward-scattered pions to hit the higher part of the upper arrays while their conjugate protons scattered downward into Array II. This provided a particularly gratifying check on the validity of the background subtraction method (discussed in Section III-B-5) which was used for forward-angle π-up events with the target magnetic field in the normal direction.

At all momenta and for all data blocks there was available the bin-to-bin consistency check. In no instance was an anomalous variation noted between the polarization parameter calculated from counts in adjacent θ_{up} bins (unless some array counter actually was not working--and the few instances when this happened were readily detected.) An example of a bin-by-bin calculation of the polarization parameter at 1441 MeV/c is shown in Fig. 14.

In the final results reported below, the results of these

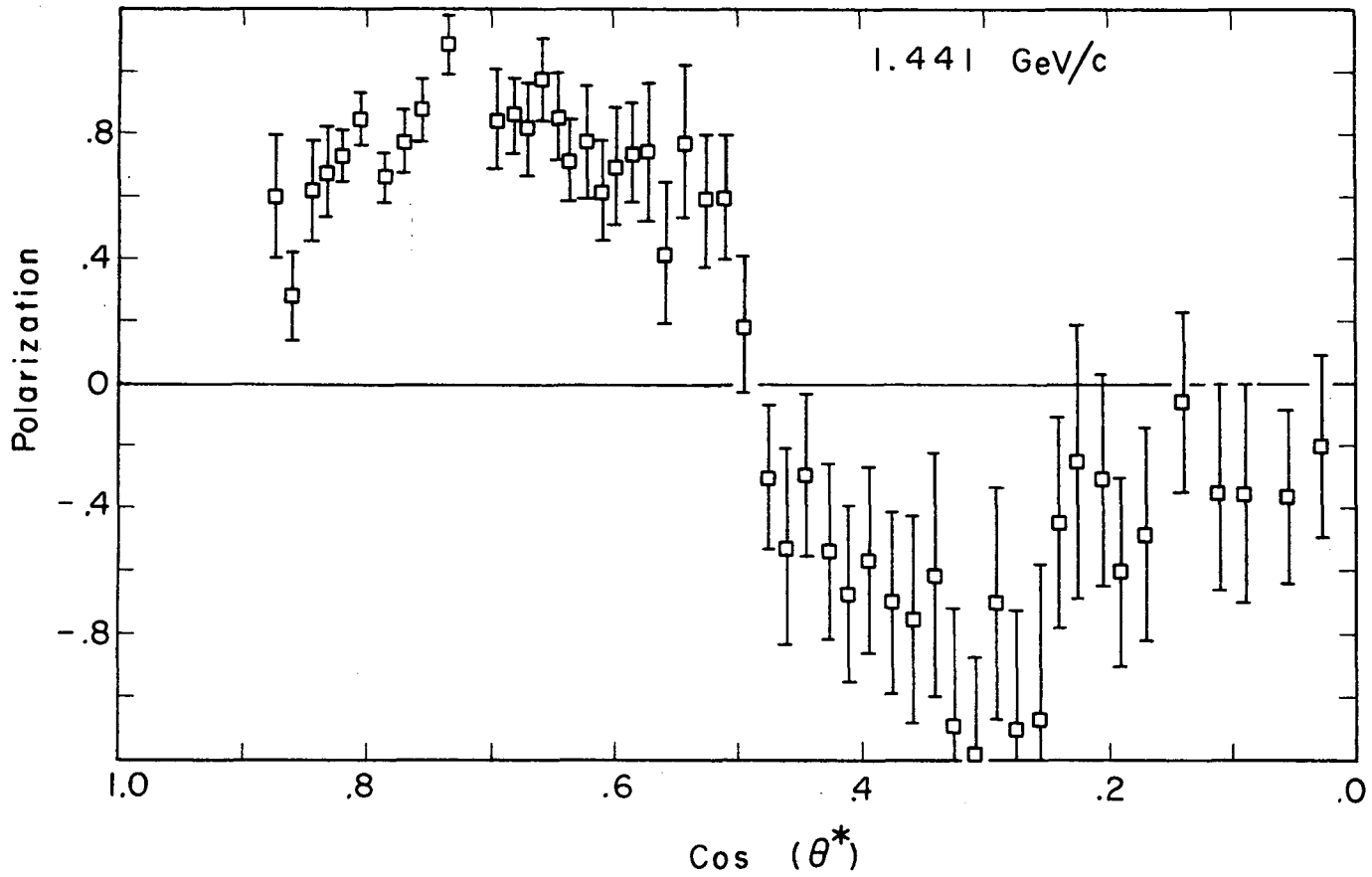

X BL677-3675

Fig. 14. Results obtained at 1.441 GeV/c plotted before being averaged over groups of adjacent θ_{up} bins. The bin-to-bin consistency in the case shown here is typical of that found in each block of data.

separate analyses of the different blocks of data have been combined where they overlap in energy and angle. Also, the results of the calculation of the polarization parameter from counts in adjacent θ_{up} bins have been averaged over groups of from two to four bins. The actual number of bins combined in a given instance depended on how rapidly the polarization parameter appeared to be changing as a function of angle. In all cases the final result reported below has been calculated with weighting matching the statistical accuracy of the points involved. The formulae used were the customary ones:

$$P = \frac{\Sigma(\Delta P_k)^{-2} P_k}{\Sigma(\Delta P_k)^{-2}} \quad ; \quad \Delta P = (\Sigma(\Delta P_k)^{-2})^{-1/2} \quad ,$$

where the P_k and ΔP_k are the values and statistical errors of the polarization parameter calculated from the θ_{up} bins to be combined.

3. Errors

The principal source of error in all the data was simply statistical fluctuations in counting rates. Throughout the experiment the emphasis was on obtaining moderately good information at as many different energies and angles as possible with the intention of providing data for phase shift analyses of the πN system, rather than on accumulating very good data at only a few points.

But there is also a possible systematic error of ±8% associated mainly with inaccurate measurement of the target polarization. This would have the effect of changing the scale against which the polarization results are quoted. This error results from uncertainty concerning how accurately the NMR polarization signal in the course of data-taking run can be measured, how well that signal represents the true average target polarization during that run, and how absolutely that signal can be normalized. Error in the first and second cases is probably about ±3% each, judging from repeated measurements under stable conditions. The final normalization, though, relies on how well the thermal equilibrium (TE) polarization can be known and used to calibrate the system. Even if it is reasonably assumed that the crystals are at the temperature of their helium bath and that that temperature is well known by an accurate McCleod-gauge vapor-pressure measurement, the detected TE NMR signal is small and noisy enough to be unreproducible by ±5% over short periods of of time, and the whole detection system seems to have enough slow drift to make the short-term averages not repeatable over 12-24 hour periods to more than another ±5%. Combining these uncertainties gives the quoted

8% systematic error.

Concerning the topic of measuring target polarization, it is worth mentioning that there are differences in the techniques used at the various laboratories which have polarized targets. In this experiment the NMR frequency was swept slowly through the proton resonance. A complete sweep took about two minutes. Both the change in the rf power level in the NMR circuit and the derivative of that change were recorded for later computer calculation of the target polarization. In contrast, the European laboratories in recent experiments have used a fast (milliseconds) sweep through the resonance, repeated frequently, and allowing on-line computation of the target polarization by analog methods. They tend to report consistently higher target polarizations than we do. And for a given observed scattering asymmetry, higher target polarizations give lower (absolute) values of the polarization parameter.

See Ref. 39 for a more complete discussion of the types of polarization detection systems currently in use.

IV. FINAL RESULTS

Tables IV through XVIII and Figures 15 through 29 give the final results of the polarization calculation and data combination discussed in Section III-C. The errors quoted and shown are only the purely statistical ones discussed in III-C-1 and the Appendix. The ±8% systematic error estimated in Section III-C-3 is not included. Its effect is to introduce a ±8% uncertainty in the scale against which the polarization is quoted and plotted.

The angular ranges over which results were obtained were limited by several factors. At some momenta data were taken only with the polarized target magnetic field in the normal direction, and at the lower momenta this left the backward angles inaccessible. This was the chief backward limitation on the data up through 1084 MeV/c.

At all momenta the forward limitation was the requirement that the recoil proton have more than about 350 MeV/c momentum to escape the target and be detected reliably.

Finally there was the problem of cross sections being too small to permit the elastic peak to stand out above background. Fifty μb/sr, center-of-mass, was about the limit under best conditions. This was the principal backward limitation on the higher momenta results. And it was a limitation at backward angles aggravated at all momenta by the fact that pions had to be detected in down Array I near the target where background was highest.

Agreement of the results of this experiment with similar existing data is good where such data does exist. Also in good agreement with

existing data[41-43] is the result of a test run which measured p-p polarization with the same experimental setup described here, unchanged except for tuning the beam to 1390 MeV/c (kinetic energy = 738 MeV) protons. This provided a check of the target polarization calculations as well as of the counting apparatus. The results of this p-p polarization measurement are given in Table XIX.

Table IV. Polarization parameter $P(\theta)$ in $\pi^+ p$ scattering. The error $\Delta P(\theta)$ is statistical only and does not include the systematic error discussed in Section III-C-3.

P_{lab}=.745 GeV/c	T_{lab}=.618 GeV		E_{cm}=1.524 GeV
Cos θ_{cm}	-t	$P(\theta)$	$\Delta P(\theta)$
.510	.208	-.28	.13
.466	.227	-.24	.11
.419	.247	-.19	.09
.362	.271	-.20	.08
.303	.297	-.25	.09
.243	.322	-.09	.10
.183	.347	-.04	.12
.124	.373	-.21	.12
.054	.402	-.19	.13
-.042	.443	-.17	.17

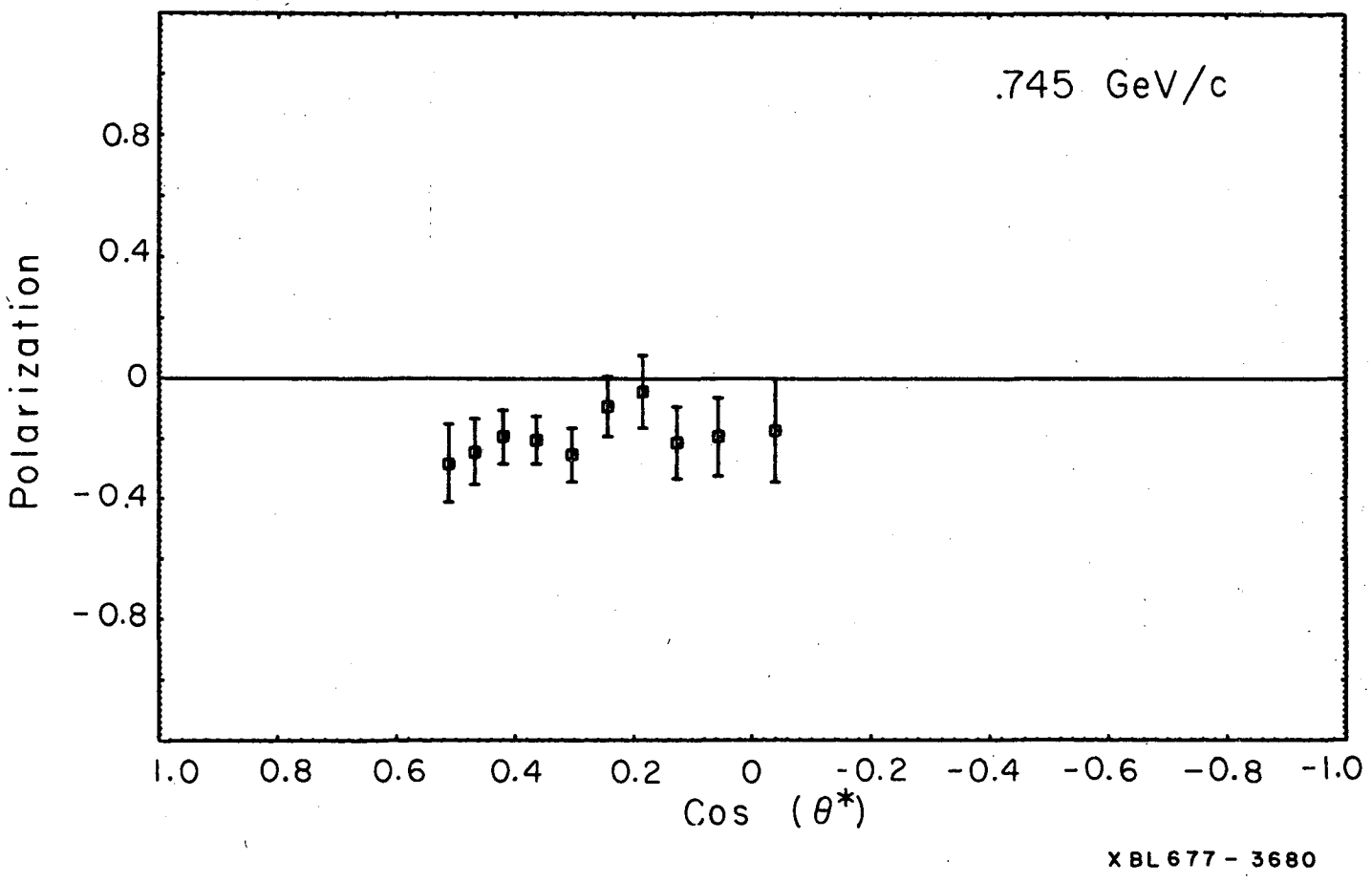

Fig. 15. Polarization parameter in π^+p elastic scattering for an incident pion momentum of 0.745 GeV/c. The errors shown are statistical only and do not include the ±8% systematic error discussed in Section III-C-3. This systematic error comes from inaccurate knowledge of the target polarization and results in an 8% uncertainty in the scale against which the polarization parameter is plotted.

Table V. Polarization parameter $P(\theta)$ in $\pi^+ p$ scattering. The error $\Delta P(\theta)$ is statistical only and does not include the systematic error discussed in Section III-C-3.

P_{lab}=.895 GeV/c	T_{lab}=.766 GeV	E_{cm}=1.612 GeV	
Cos θ_{cm}	-t	$P(\theta)$	$\Delta P(\theta)$
.601	.170	-.20	.13
.549	.192	-.15	.12
.503	.211	.04	.11
.451	.233	-.14	.09
.391	.259	-.21	.09
.329	.285	-.19	.10
.268	.311	-.10	.12
.207	.337	.00	.13
.145	.364	.04	.16
.055	.402	-.05	.15
-.046	.445	.22	.22

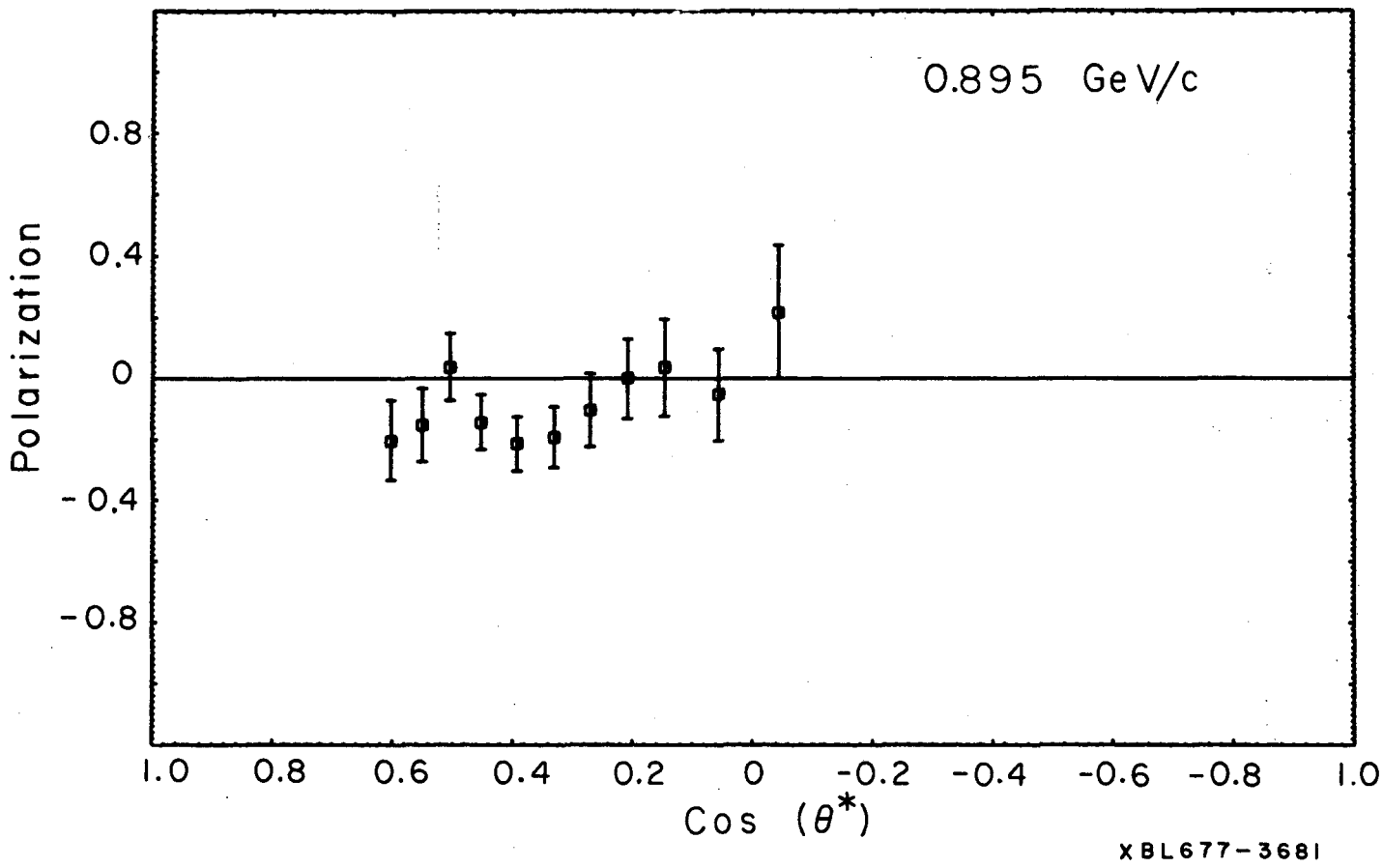

Fig. 16. Polarization parameter in π^+p elastic scattering for an incident pion momentum of 0.895 GeV/c. The errors shown are statistical only and do not include the ±8% systematic error discussed in Section III-C-3. This systematic error comes from inaccurate knowledge of the target polarization and results in an 8% uncertainty in the scale against which the polarization parameter is plotted.

Table VI. Polarization parameter $P(\theta)$ in $\pi^+ p$ scattering. The error $\Delta P(\theta)$ is statistical only and does not include the systematic error discussed in Section III-C-3.

P_{lab}=1.024 GeV/c	T_{lab}=.894 GeV		E_{cm}=1.685 GeV
$\cos\theta_{cm}$	-t	$P(\theta)$	$\Delta P(\theta)$
.749	.164	-.05	.23
.693	.201	.27	.14
.622	.247	.22	.08
.583	.273	.15	.07
.537	.303	.13	.06
.484	.338	.08	.06
.422	.378	.12	.07
.360	.419	.09	.06
.297	.460	.11	.07
.234	.501	.11	.07
.170	.542	.09	.08
.078	.603	.31	.09
-.025	.671	.42	.10
-.104	.722	.55	.22

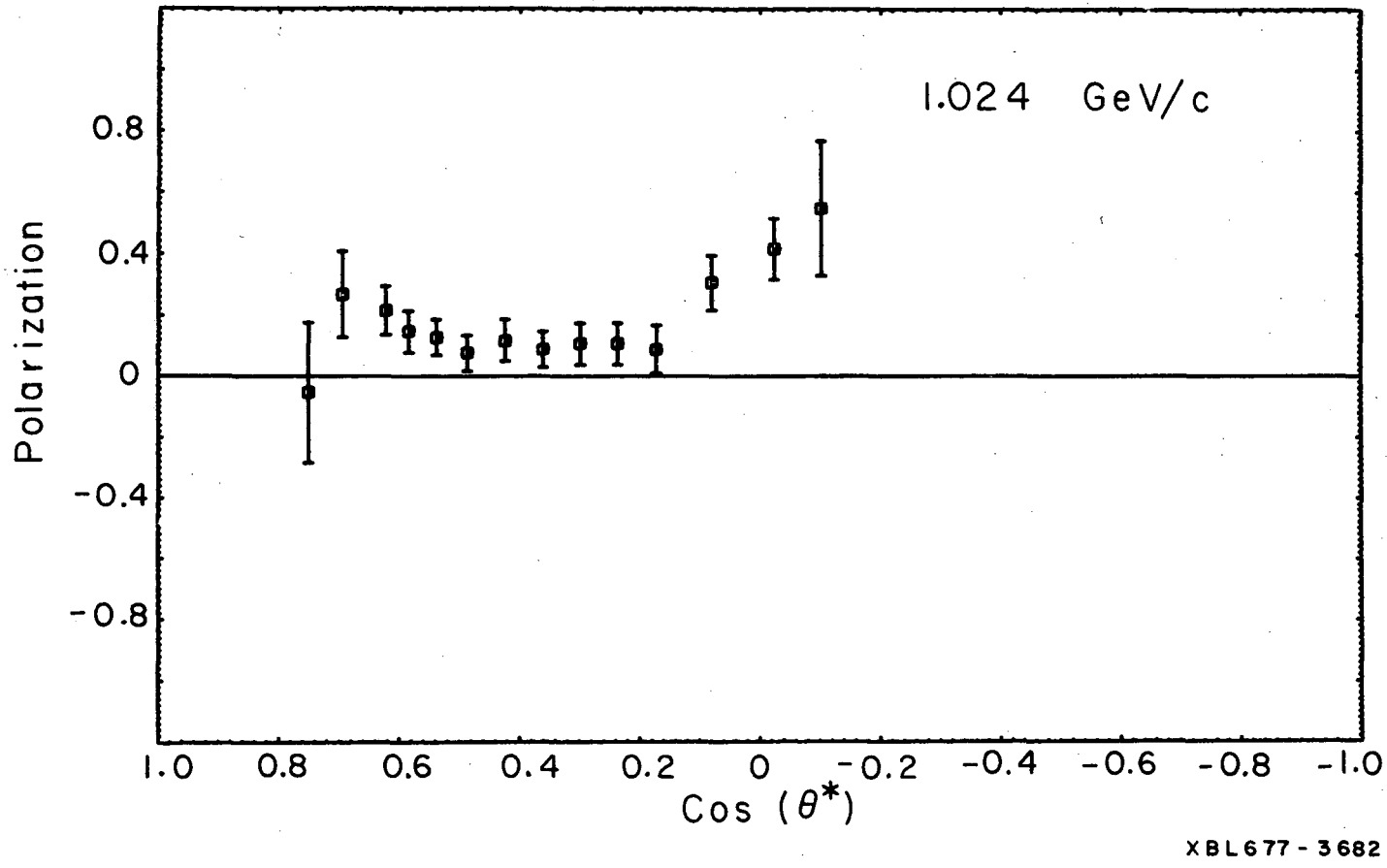

Fig. 17. Polarization parameter in π^+p elastic scattering for an incident pion momentum of 1.024 GeV/c. The errors shown are statistical only and do not include the ±8% systematic error discussed in Section III-C-3. This systematic error comes from inaccurate knowledge of the target polarization and results in an 8% uncertainty in the scale against which the polarization parameter is plotted.

Table VII. Polarization parameter $P(\theta)$ in $\pi^+ p$ scattering. The error $\Delta P(\theta)$ is statistical only and does not include the systematic error discussed in Section III-C-3.

P_{lab}=1.084 GeV/c	T_{lab}=.953 GeV		E_{cm}=1.718 GeV
Cos θ_{cm}	-t	$P(\theta)$	$\Delta P(\theta)$
.746	.179	.26	.15
.670	.233	.29	.13
.607	.277	.22	.09
.561	.309	.09	.08
.510	.345	.12	.07
.449	.389	.10	.07
.386	.433	-.02	.08
.322	.478	-.03	.10
.259	.523	-.05	.12
.195	.567	.10	.11
.111	.627	.05	.13
.006	.701	.18	.14
-.088	.767	.16	.25

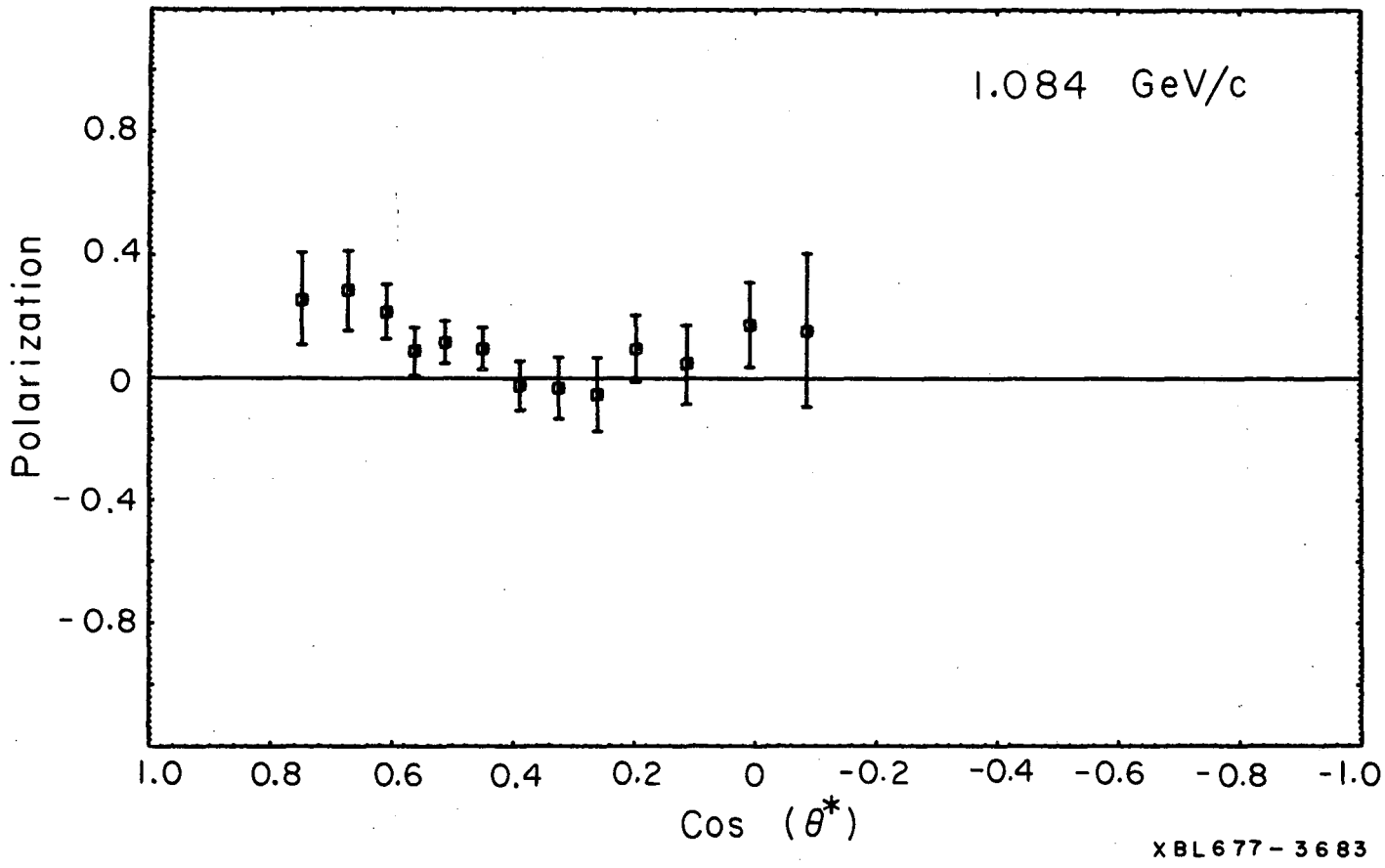

Fig. 18. Polarization parameter in π^+p elastic scattering for an incident pion momentum of 1.084 GeV/c. The errors shown are statistical only and do not include the ±8% systematic error discussed in Section III-C-3. This systematic error comes from inaccurate knowledge of the target polarization and results in an 8% uncertainty in the scale against which the polarization parameter is plotted.

Table VIII. Polarization parameter $P(\theta)$ in $\pi^+ p$ scattering. The error $\Delta P(\theta)$ is statistical only and does not include the systematic error discussed in Section III-C-3.

P_{lab}=1.155 GeV/c	T_{lab}=1.024 GeV	E_{cm}=1.756 GeV	
Cos θ_{cm}	-t	$P(\theta)$	$\Delta P(\theta)$
.787	.163	.64	.12
.755	.188	.65	.15
.727	.209	.35	.11
.642	.274	.26	.08
.596	.309	.30	.06
.549	.346	.14	.06
.491	.390	.12	.06
.428	.438	.20	.06
.364	.487	.05	.06
.299	.537	-.03	.08
.235	.586	.06	.09
.166	.639	.00	.09
.064	.717	.04	.11
-.040	.796	.00	.13
-.103	.845	.00	.25
-.928	1.476	.46	.12
-.960	1.500	.10	.10

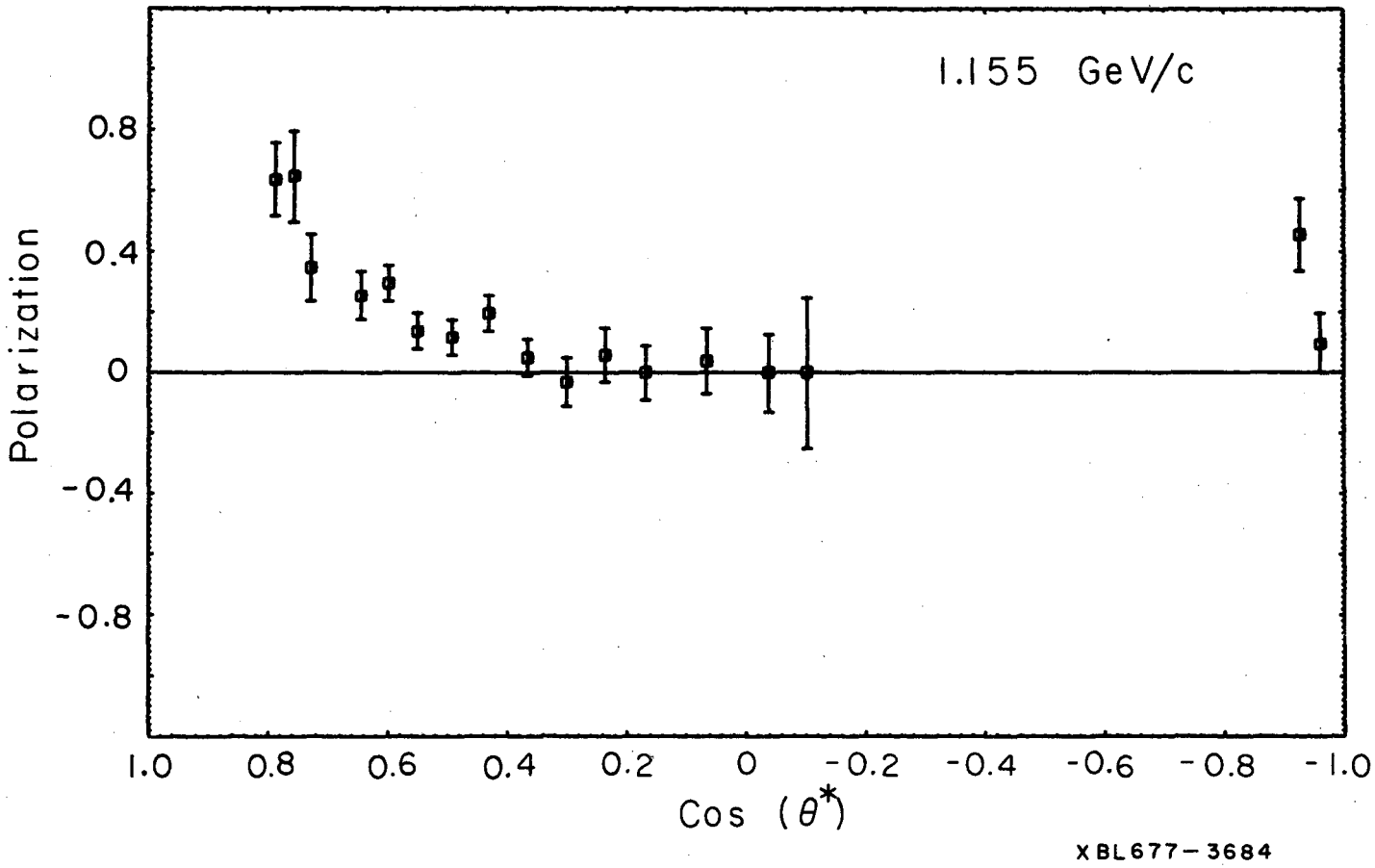

Fig. 19. Polarization parameter in π^+p elastic scattering for an incident pion momentum of 1.155 GeV/c. The errors shown are statistical only and do not include the ±8% systematic error discussed in Section III-C-3. This systematic error comes from inaccurate knowledge of the target polarization and results in an 8% uncertainty in the scale against which the polarization parameter is plotted.

Table IX. Polarization parameter $P(\theta)$ in $\pi^+ p$ scattering. The error $\Delta P(\theta)$ is statistical only and does not include the systematic error discussed in Section III-C-3.

P_{lab}=1.284 GeV/c	T_{lab}=1.152 GeV		E_{cm}=1.823 GeV
Cos θ_{cm}	-t	$P(\theta)$	$\Delta P(\theta)$
.826	.152	.70	.10
.781	.192	.85	.07
.737	.230	.81	.06
.706	.258	.63	.08
.665	.293	.54	.12
.631	.323	.50	.08
.596	.355	.22	.07
.559	.387	.21	.08
.514	.426	.06	.08
.466	.469	-.08	.09
.417	.512	-.09	.10
.367	.555	-.28	.11
.318	.598	-.46	.12
.260	.649	-.43	.15
.193	.707	-.48	.17
.096	.793	-.82	.23
-.011	.887	-.90	.25
-.092	.958	-.95	.35
-.523	1.336	.12	.26
-.639	1.437	.37	.24
-.752	1.536	.63	.31
-.830	1.605	.35	.23
-.880	1.649	.13	.13
-.922	1.686	.11	.08
-.956	1.715	-.12	.08

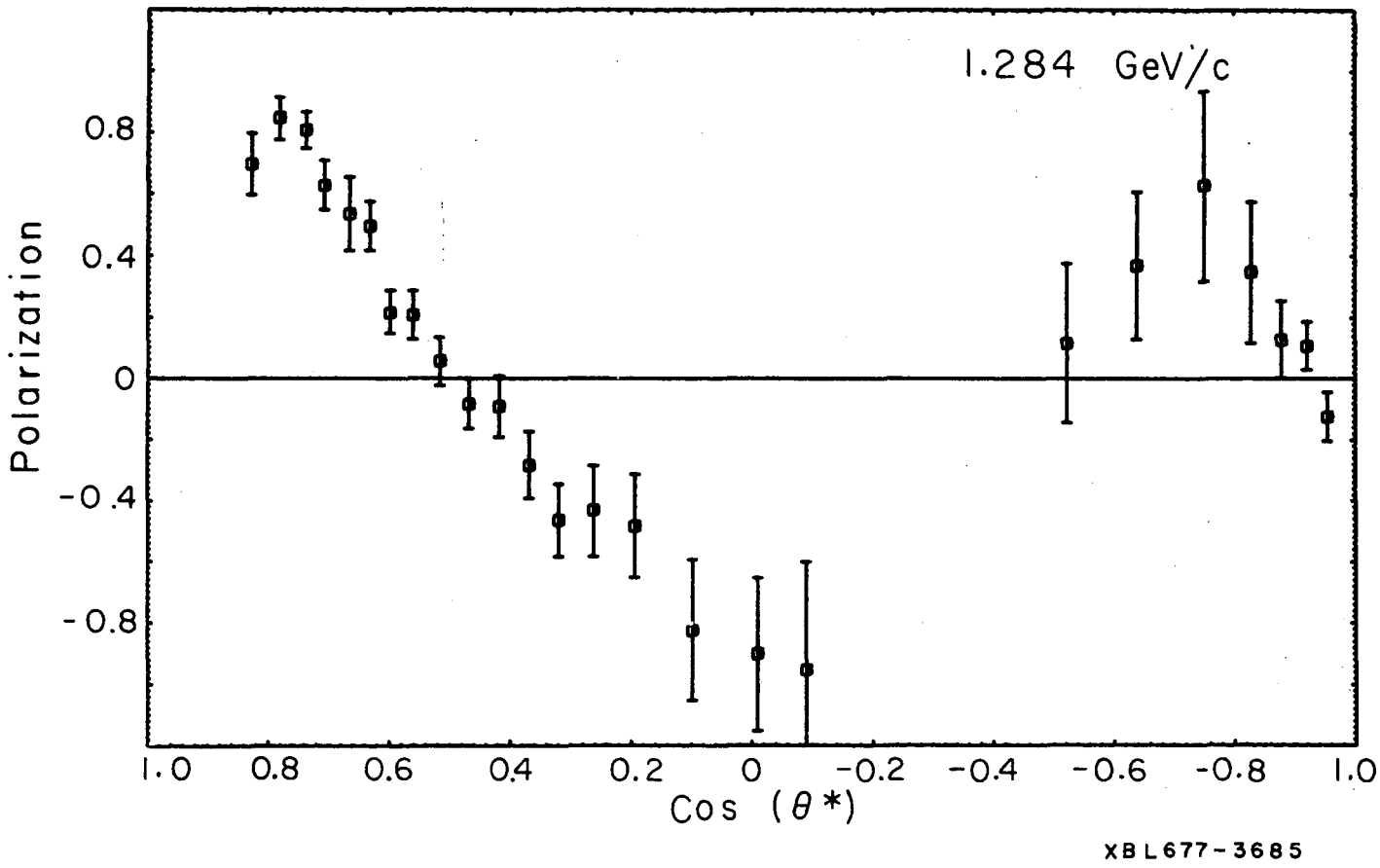

Fig. 20. Polarization parameter in $\pi^+ p$ elastic scattering for an incident pion momentum of 1.284 GeV/c. The errors shown are statistical only and do not include the ±8% systematic error discussed in Section III-C-3. This systematic error comes from inaccurate knowledge of the target polarization and results in an 8% uncertainty in the scale against which the polarization parameter is plotted.

Table X. Polarization parameter $P(\theta)$ in $\pi^+ p$ scattering. The error $\Delta P(\theta)$ is statistical only and does not include the systematic error discussed in Section III-C-3.

P_{lab}=1.352 GeV/c	T_{lab}=1.220 GeV		E_{cm}=1.857 GeV
Cos θ_{cm}	-t	$P(\theta)$	$\Delta P(\theta)$
.831	.159	.89	.14
.778	.208	.80	.11
.709	.273	.70	.10
.644	.333	.63	.10
.603	.372	.64	.11
.572	.401	.19	.17
.536	.435	.01	.12
.470	.488	-.14	.11
.413	.549	-.35	.11
.346	.612	-.58	.13
.280	.675	-.87	.14
.213	.737	-.84	.17
.139	.806	-1.02	.16
.056	.884	-.65	.16
-.024	.959	-.02	.16
-.093	1.023	.11	.19
-.215	1.138	-.51	.29
-.316	1.232	.33	.22
-.403	1.314	.18	.18
-.477	1.383	.24	.17
-.560	1.461	.22	.27
-.679	1.572	.69	.29

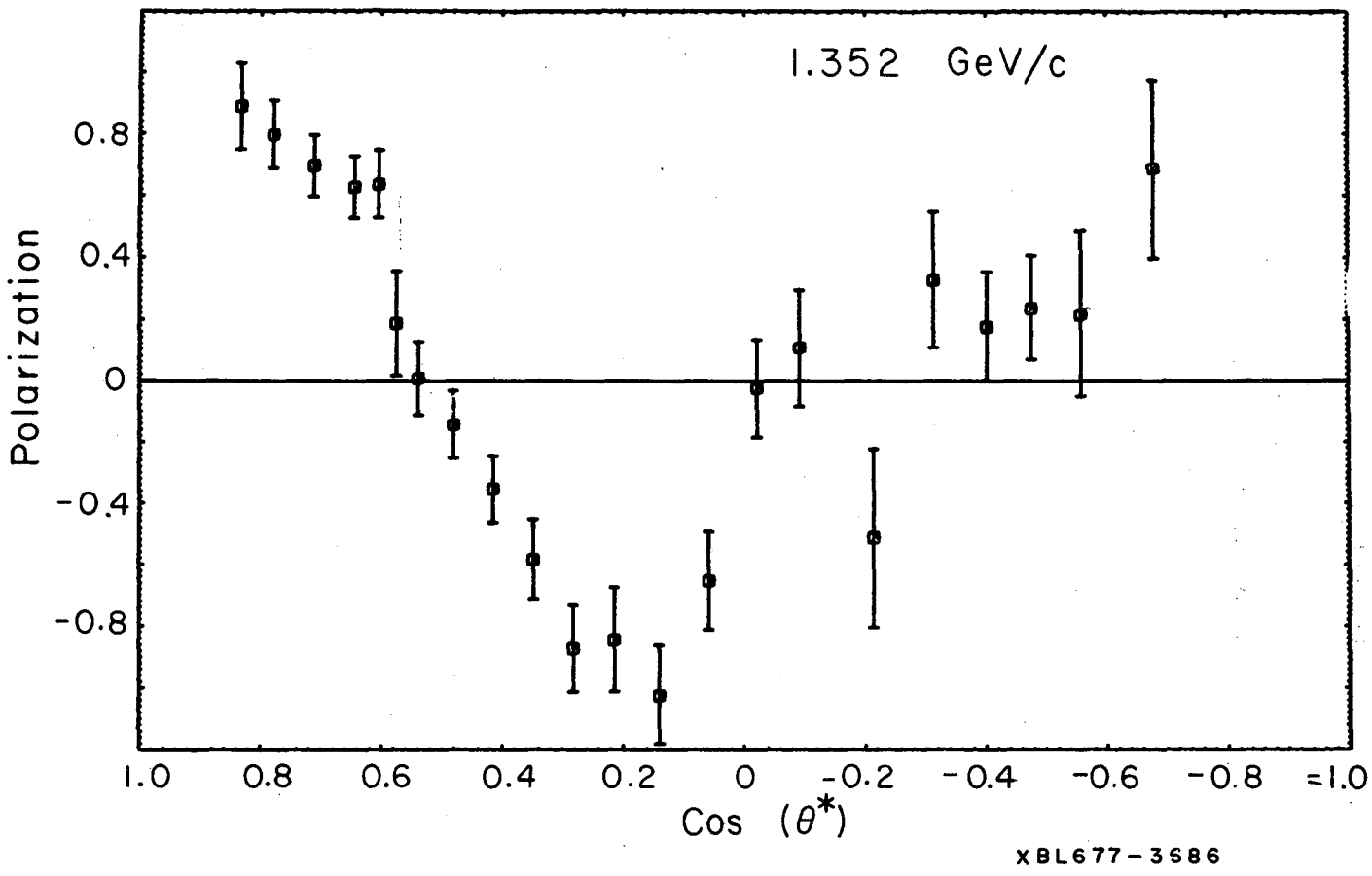

Fig. 21. Polarization parameter in π^+p elastic scattering for an incident pion momentum of 1.352 GeV/c. The errors shown are statistical only and do not include the ±8% systematic error discussed in Section III-C-3. This systematic error comes from inaccurate knowledge of the target polarization and results in an 8% uncertainty in the scale against which the polarization parameter is plotted.

Table XI. Polarization parameter $P(\theta)$ in $\pi^+ p$ scattering. The error $\Delta P(\theta)$ is statistical only and does not include the systematic error discussed in Section III-C-3.

P_{lab}=1.441 GeV/c T_{lab}=1.308 GeV E_{cm}=1.902 GeV

Cos θ_{cm}	-t	$P(\theta)$	$\Delta P(\theta)$
.861	.141	.47	.16
.835	.167	.71	.08
.801	.202	.75	.05
.765	.238	.83	.05
.721	.282	1.00	.06
.676	.328	.98	.06
.641	.363	.82	.07
.598	.408	.69	.10
.558	.449	.64	.13
.518	.489	.59	.15
.493	.514	.19	.22
.460	.548	-.35	.15
.401	.608	-.62	.15
.333	.677	-.92	.18
.265	.746	-.79	.19
.215	.797	-.43	.17
.125	.887	-.29	.16
.015	1.000	-.12	.14
-.107	1.121	-.08	.13
-.234	1.252	-.11	.22
-.334	1.353	-.21	.22
-.421	1.441	-.24	.23
-.489	1.507	.12	.12
-.614	1.637	.29	.16
-.730	1.755	.52	.41
-.804	1.830	.96	.43
-.858	1.885	.49	.20
-.900	1.927	.13	.13
-.930	1.958	-.07	.10
-.955	1.984	-.05	.10

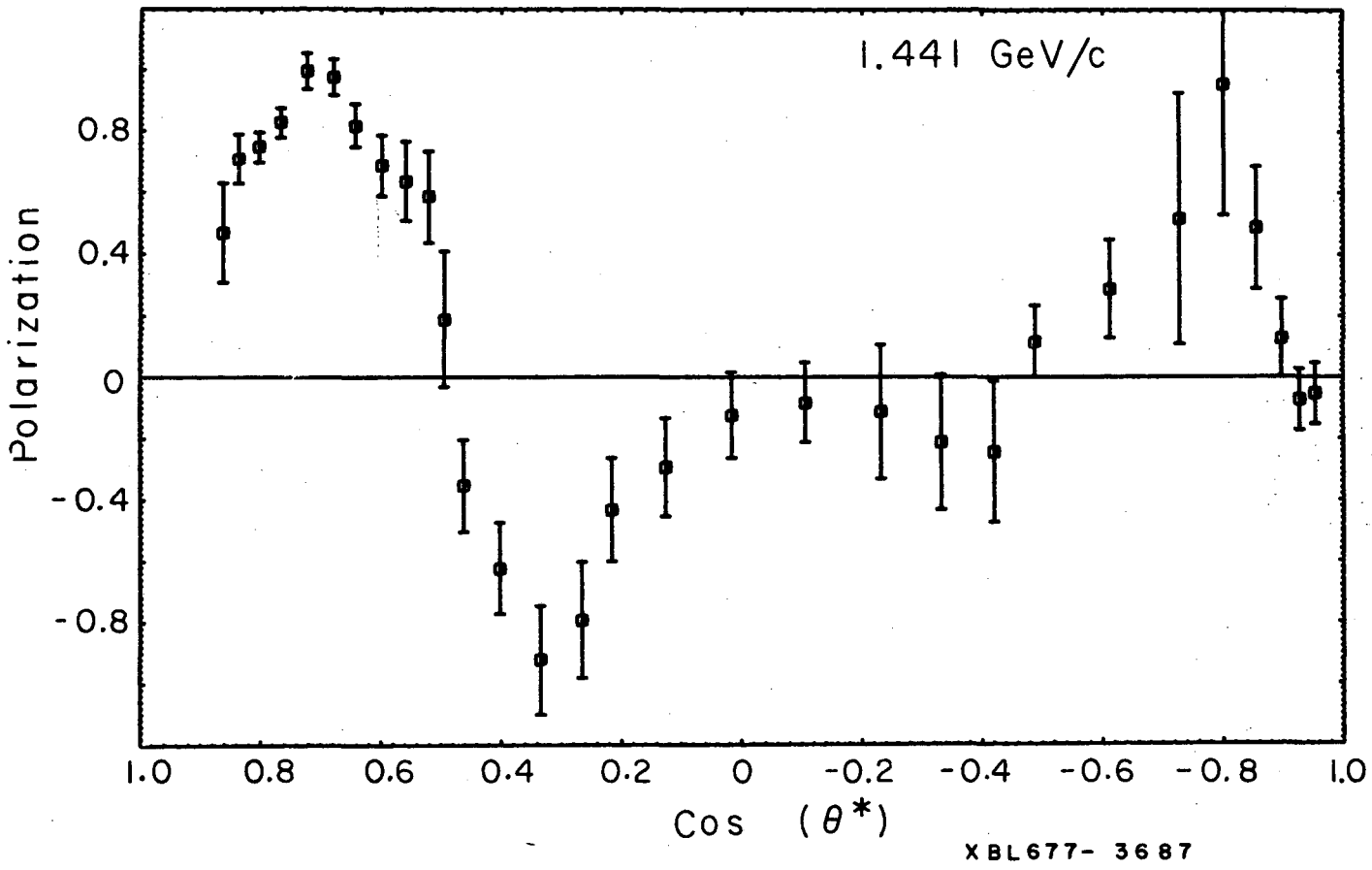

Fig. 22. Polarization parameter in π^+p elastic scattering for an incident pion momentum of 1.441 GeV/c. The errors shown are statistical only and do not include the ±8% systematic error discussed in Section III-C-3. This systematic error comes from inaccurate knowledge of the target polarization and results in an 8% uncertainty in the scale against which the polarization parameter is plotted.

Table XII. Polarization parameter $P(\theta)$ in $\pi^+ p$ scattering. The error $\Delta P(\theta)$ is statistical only and does not include the systematic error discussed in Section III-C-3.

P_{lab}=1.570 GeV/c T_{lab}=1.437 GeV E_{cm}=1.964 GeV

Cos θ_{cm}	-t	$P(\theta)$	$\Delta P(\theta)$
.880	.135	.05	.34
.853	.165	.48	.07
.818	.205	.45	.06
.790	.237	.47	.08
.766	.263	.59	.06
.732	.302	.76	.09
.689	.350	.77	.07
.648	.396	.85	.09
.609	.440	.89	.15
.557	.500	.47	.21
.490	.575	.27	.37
.422	.653	.22	.25
.352	.731	-.05	.25
.283	.809	.38	.24
.214	.887	-.02	.18
.123	.990	-.10	.19
.011	1.116	.29	.24
-.090	1.230	.42	.27
-.229	1.387	.22	.27
-.330	1.501	-.20	.32
-.411	1.587	.29	.14
-.502	1.690	.02	.13
-.636	1.846	.16	.26
-.741	1.959	1.17	.65
-.804	2.036	.99	.62
-.859	2.098	.05	.20
-.907	2.152	-.06	.13
-.945	2.195	-.01	.13

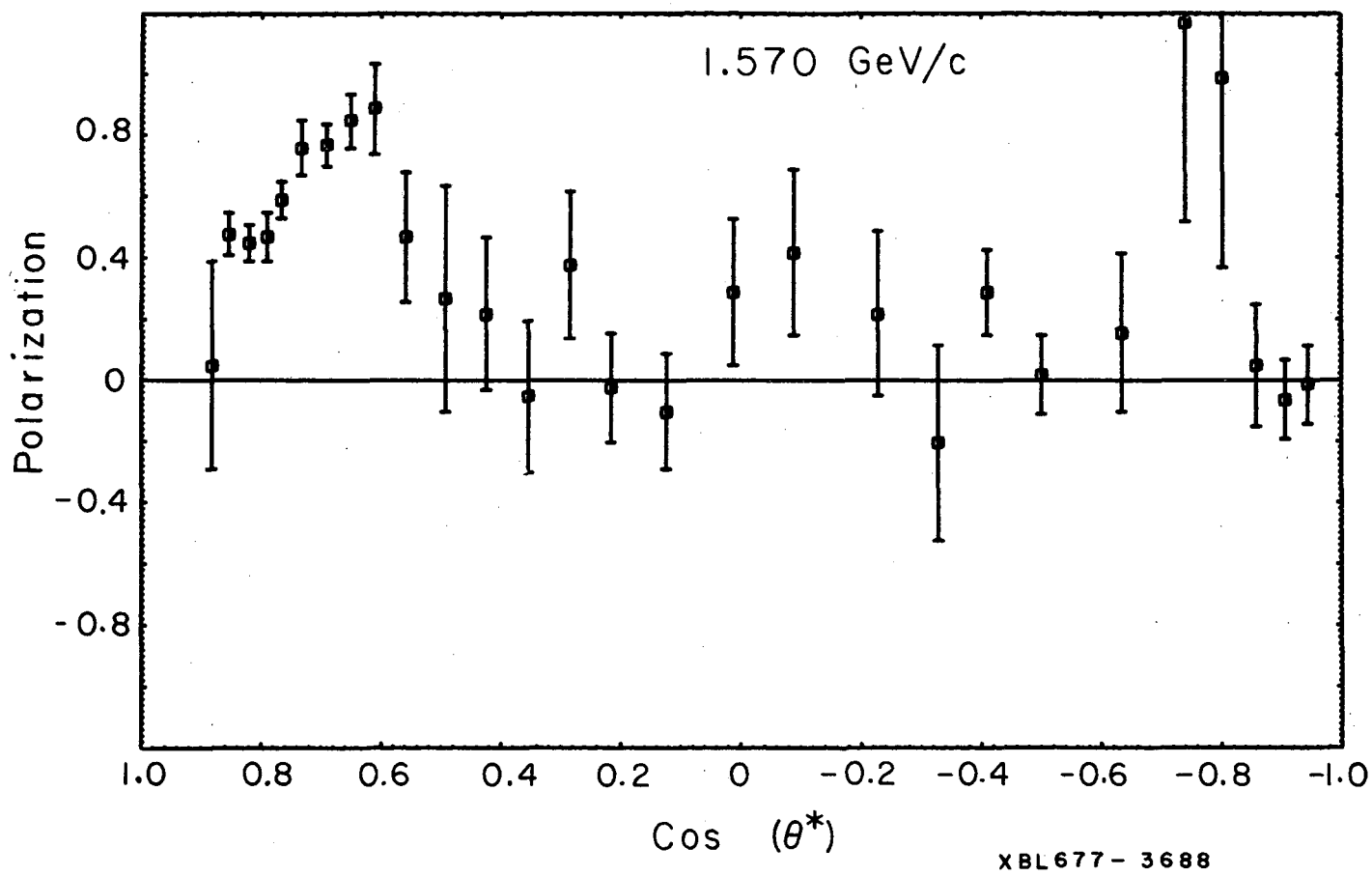

Fig. 23. Polarization parameter in π^+p elastic scattering for an incident pion momentum of 1.570 GeV/c. The errors shown are statistical only and do not include the ±8% systematic error discussed in Section III-C-3. This systematic error comes from inaccurate knowledge of the target polarization and results in an 8% uncertainty in the scale against which the polarization parameter is plotted.

Table XIII. Polarization parameter $P(\theta)$ in $\pi^+ p$ scattering. The error $\Delta P(\theta)$ is statistical only and does not include the systematic error discussed in Section III-C-3.

P_{lab}=1.690 GeV/c	T_{lab}=1.556 GeV	E_{cm}=2.020 GeV

Cos θ_{cm}	-t	$P(\theta)$	$\Delta P(\theta)$
.887	.140	.25	.08
.860	.173	.31	.05
.830	.209	.43	.04
.799	.249	.40	.05
.765	.290	.45	.05
.704	.366	.42	.08
.680	.396	.53	.08
.655	.426	.47	.09
.630	.457	.60	.11
.598	.497	.83	.12
.545	.562	.87	.14
.476	.648	.86	.16
.405	.734	.90	.16
.334	.822	.98	.13
.303	.861	.84	.21
.264	.909	.82	.14
.148	1.053	.40	.25
.090	1.124	.57	.10
-.023	1.263	.42	.11
-.111	1.371	.33	.16
-.218	1.505	.16	.25
-.320	1.631	-.23	.27
-.416	1.749	.00	.25
-.494	1.845	.05	.21
-.565	1.933	-.06	.21

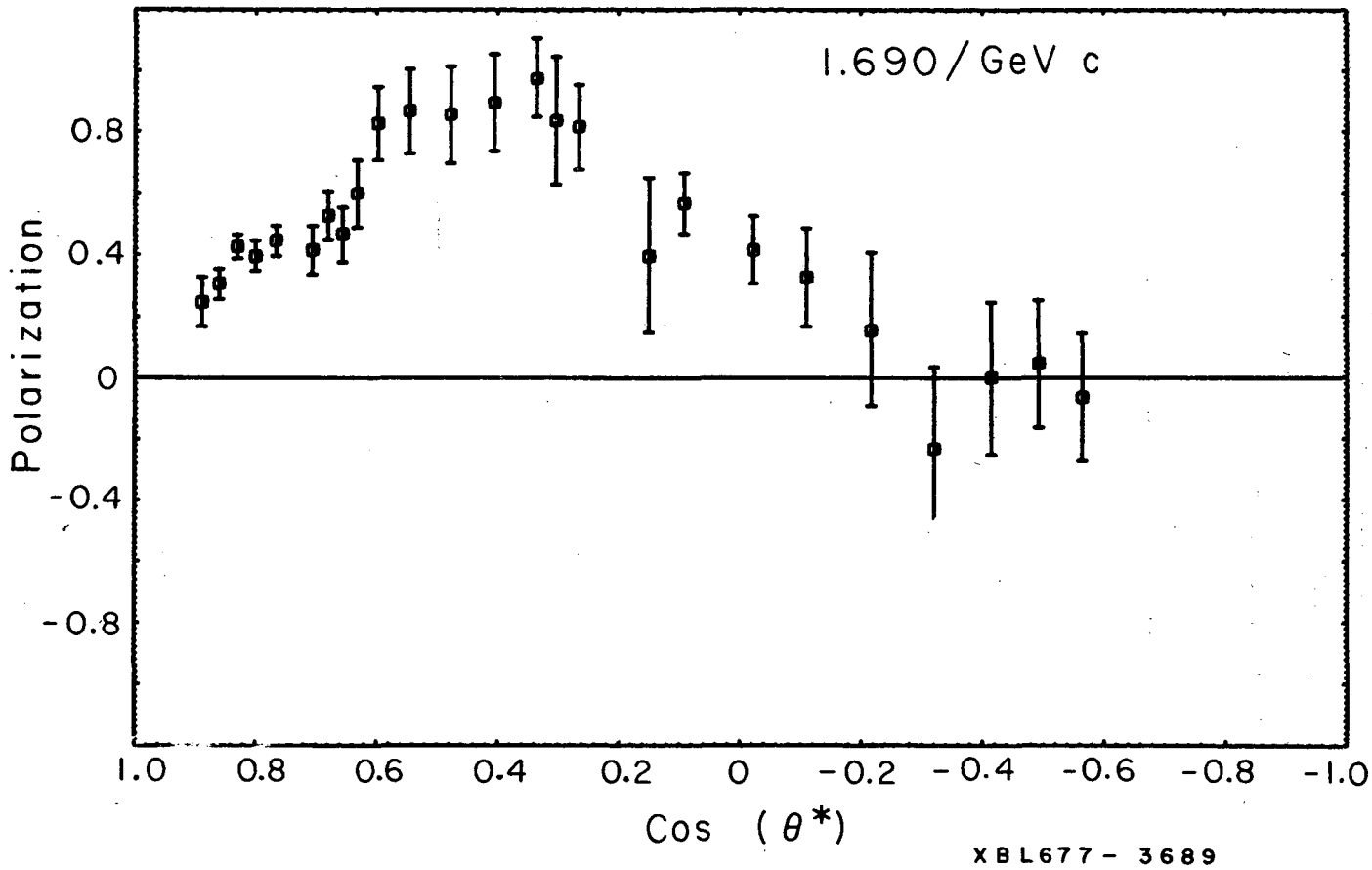

Fig. 24. Polarization parameter in π^+p elastic scattering for an incident pion momentum of 1.690 GeV/c. The errors shown are statistical only and do not include the ±8% systematic error discussed in Section III-C-3. This systematic error comes from inaccurate knowledge of the target polarization and results in an 8% uncertainty in the scale against which the polarization parameter is plotted.

Table XIV. Polarization parameter $P(\theta)$ in $\pi^+ p$ scattering. The error $\Delta P(\theta)$ is statistical only and does not include the systematic error discussed in Section III-C-3.

P_{lab}=1.869 GeV/c	T_{lab}=1.735 GeV		E_{cm}=2.102 GeV
Cos θ_{cm}	-t	$P(\theta)$	$\Delta P(\theta)$
.897	.144	.43	.14
.870	.181	.30	.08
.841	.223	.24	.06
.808	.267	.32	.06
.774	.316	.39	.06
.711	.403	.30	.09
.674	.455	.49	.08
.622	.527	.35	.11
.564	.608	.60	.14
.494	.705	.94	.20
.422	.806	1.29	.15
.349	.908	.88	.11
.277	1.001	.92	.12
.205	1.109	.85	.13
.110	1.242	.87	.20
-.006	1.403	.80	.16
-.108	1.547	.46	.22

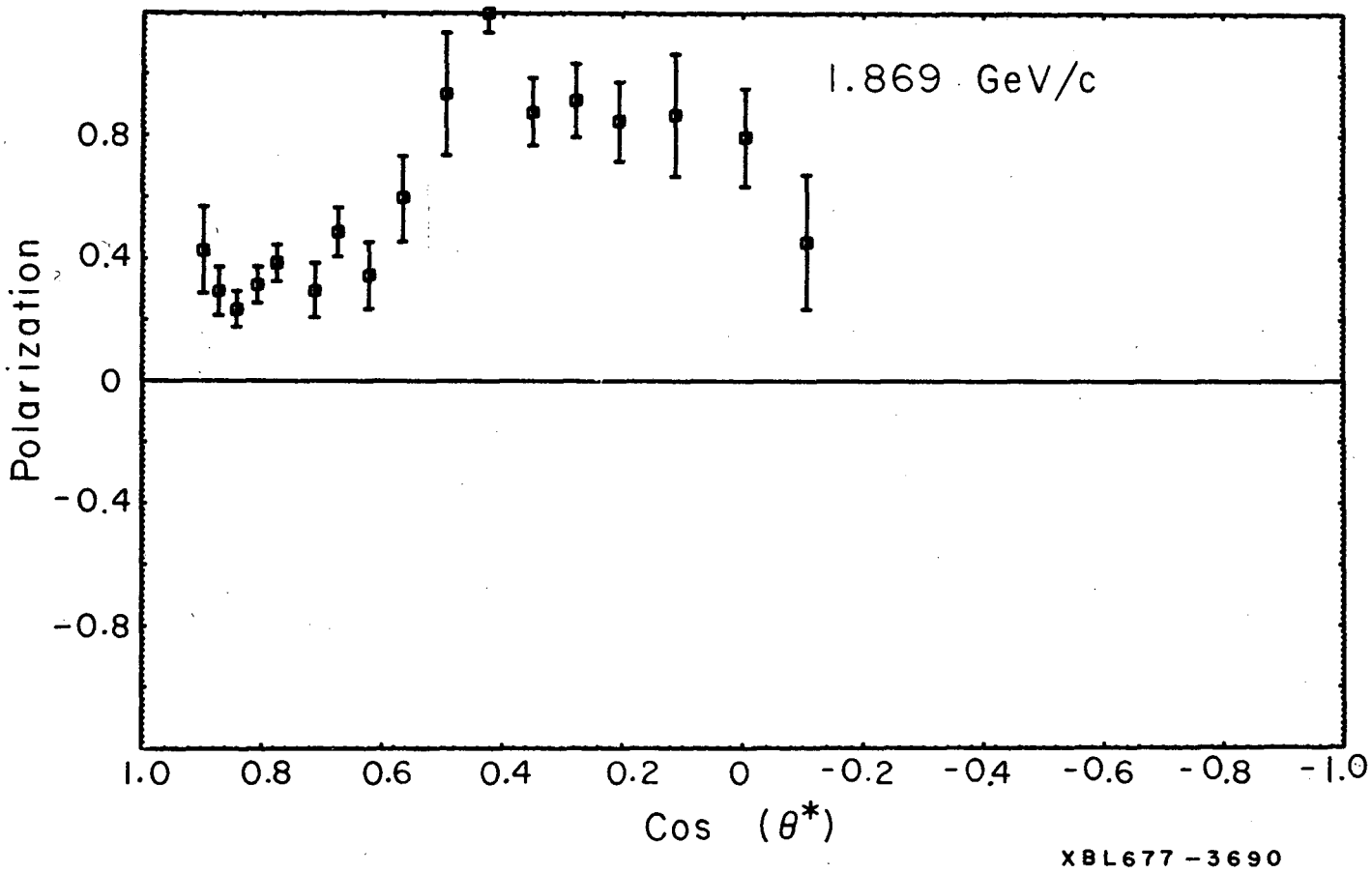

Fig. 25. Polarization parameter in π^+p elastic scattering for an incident pion momentum of 1.869 GeV/c. The errors shown are statistical only and do not include the ±8% systematic error discussed in Section III-C-3. This systematic error comes from inaccurate knowledge of the target polarization and results in an 8% uncertainty in the scale against which the polarization parameter is plotted.

Table XV. Polarization parameter $P(\theta)$ in $\pi^+ p$ scattering. The error $\Delta P(\theta)$ is statistical only and does not include the systematic error discussed in Section III-C-3.

P_{lab}=1.988 GeV/c	T_{lab}=1.853 GeV		E_{cm}=2.154 GeV
Cos θ_{cm}	-t	$P(\theta)$	$\Delta P(\theta)$
.890	.166	.29	.05
.861	.208	.36	.04
.830	.255	.28	.04
.796	.306	.32	.06
.746	.382	.30	.06
.696	.456	.29	.08
.658	.514	.19	.07
.618	.574	.29	.10
.574	.640	.23	.12
.530	.706	.43	.20
.485	.774	.69	.18
.420	.871	.79	.21
.346	.983	.90	.17
.272	1.094	.78	.16
.200	1.203	.85	.16
.103	1.348	.85	.16
-.014	1.524	.72	.23
-.117	1.679	.40	.34

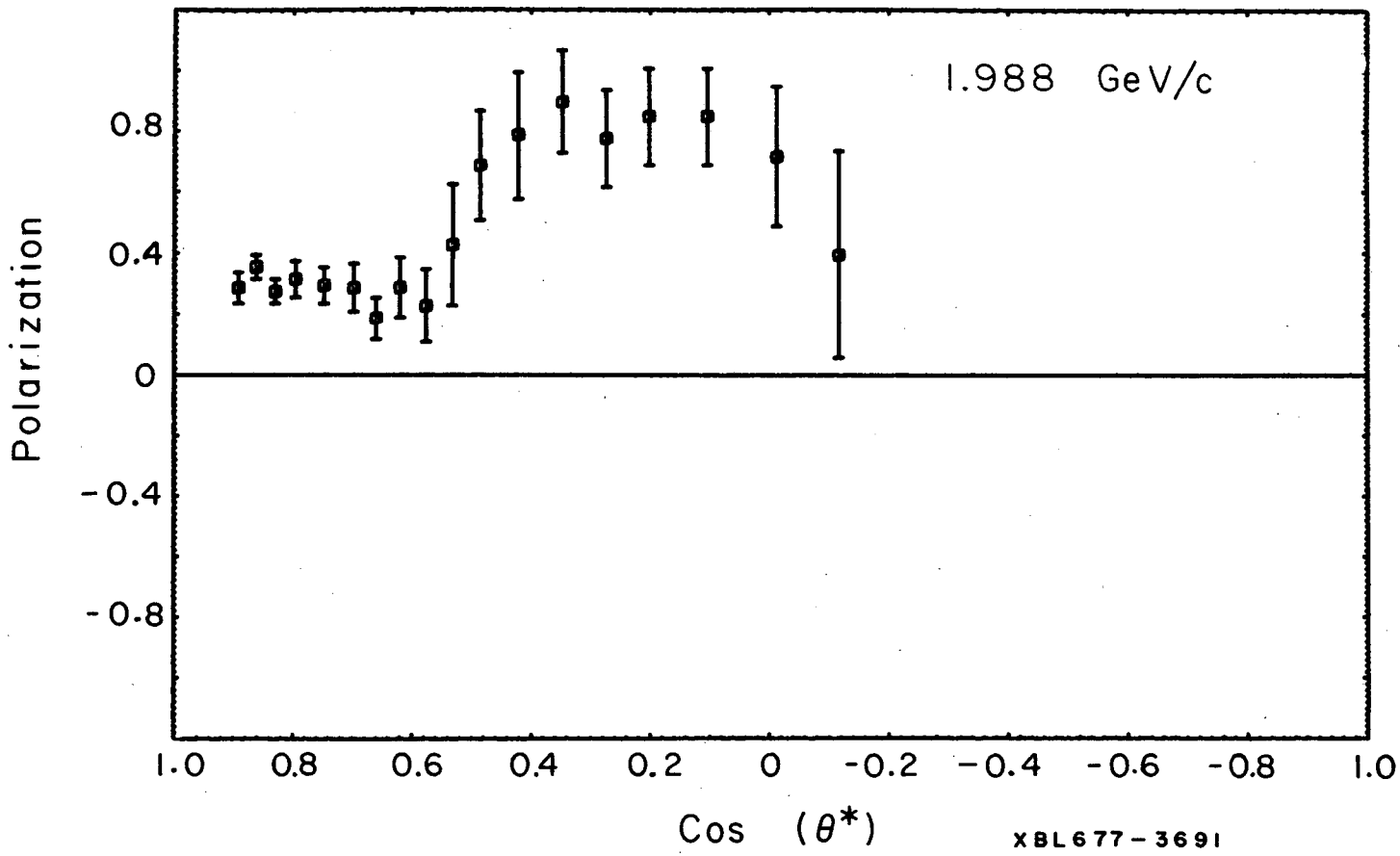

Fig. 26. Polarization parameter in π^+p elastic scattering for an incident pion momentum of 1.988 GeV/c. The errors shown are statistical only and do not include the ±8% systematic error discussed in Section III-C-3. This systematic error comes from inaccurate knowledge of the target polarization and results in an 8% uncertainty in the scale against which the polarization parameter is plotted.

Table XVI. Polarization parameter $P(\theta)$ in $\pi^+ p$ scattering. The error $\Delta P(\theta)$ is statistical only and does not include the systematic error discussed in Section III-C-3.

P_{lab}=2.535 GeV/c	T_{lab}=2.399 GeV		E_{cm}=2.380 GeV
Cos θ_{cm}	-t	$P(\theta)$	$\Delta P(\theta)$
.921	.158	.30	.07
.894	.213	.33	.04
.863	.274	.38	.04
.829	.343	.37	.06
.791	.417	.40	.08
.709	.582	.23	.11
.653	.693	.05	.11
.594	.812	.36	.21
.522	.957	.25	.19
.442	1.115	.25	.18
.362	1.275	.35	.24
.283	1.435	.23	.30
.204	1.591	-.04	.29
.121	1.757	-.03	.27
.003	1.995	-.14	.32
-.114	2.229	-.29	.37

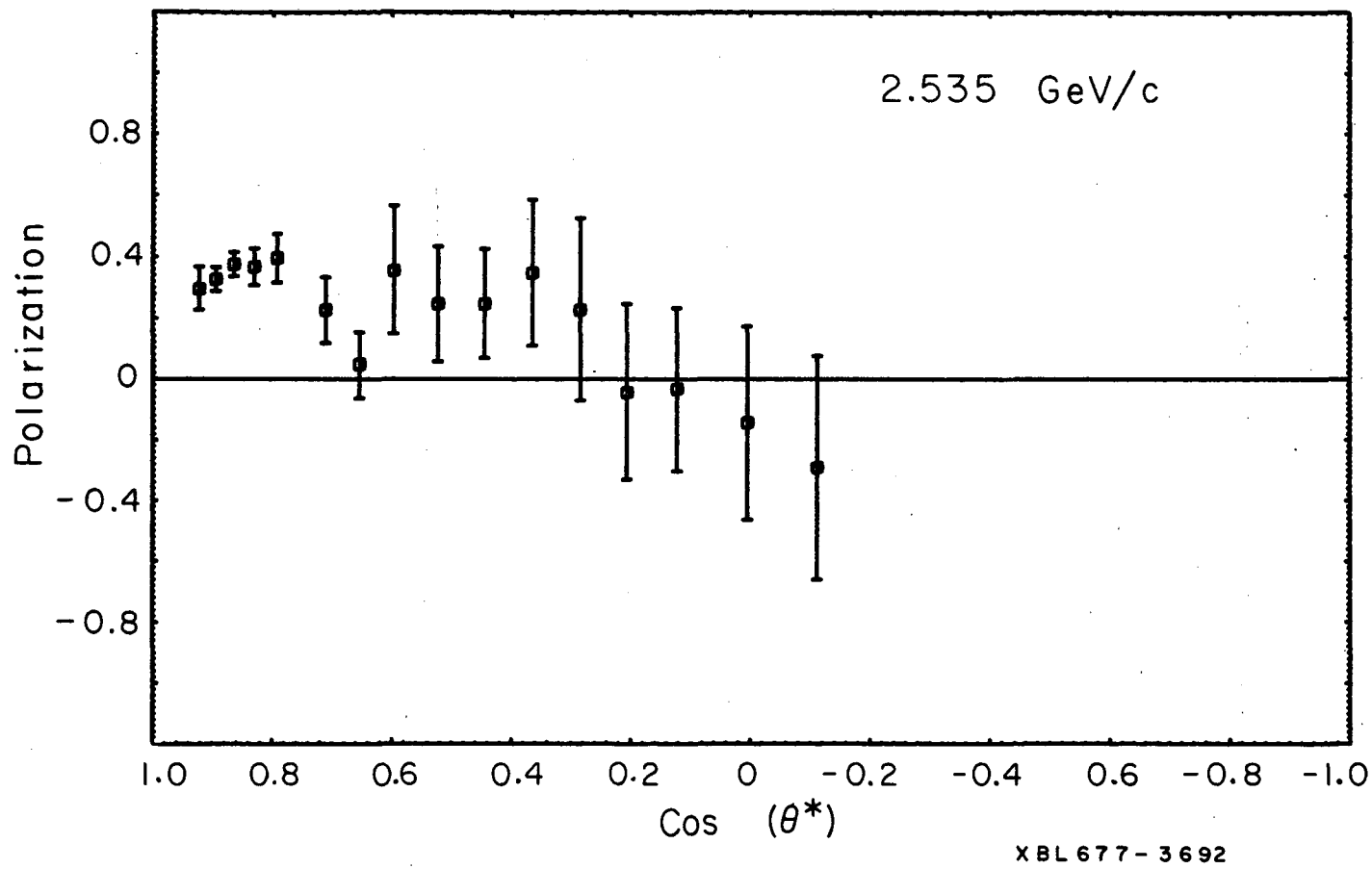

Fig. 27. Polarization parameter in $\pi^+ p$ elastic scattering for an incident pion momentum of 2.535 GeV/c. The errors shown are statistical only and do not include the ±8% systematic error discussed in Section III-C-3. This systematic error comes from inaccurate knowledte of the target polarization and results in an 8% uncertainty in the scale against which the polarization parameter is plotted.

Table XVII. Polarization parameter $P(\theta)$ in $\pi^+ p$ scattering. The error $\Delta P(\theta)$ is statistical only and does not include the systematic error discussed in Section III-C-3.

P_{lab}=3.260 GeV/c	T_{lab}=3.124 GeV		E_{cm}=2.650 GeV
Cos θ_{cm}	-t	$P(\theta)$	$\Delta P(\theta)$
.932	.181	.31	.15
.911	.237	.40	.11
.889	.297	.42	.11
.863	.364	.14	.14
.843	.419	.10	.17
.800	.534	.49	.27

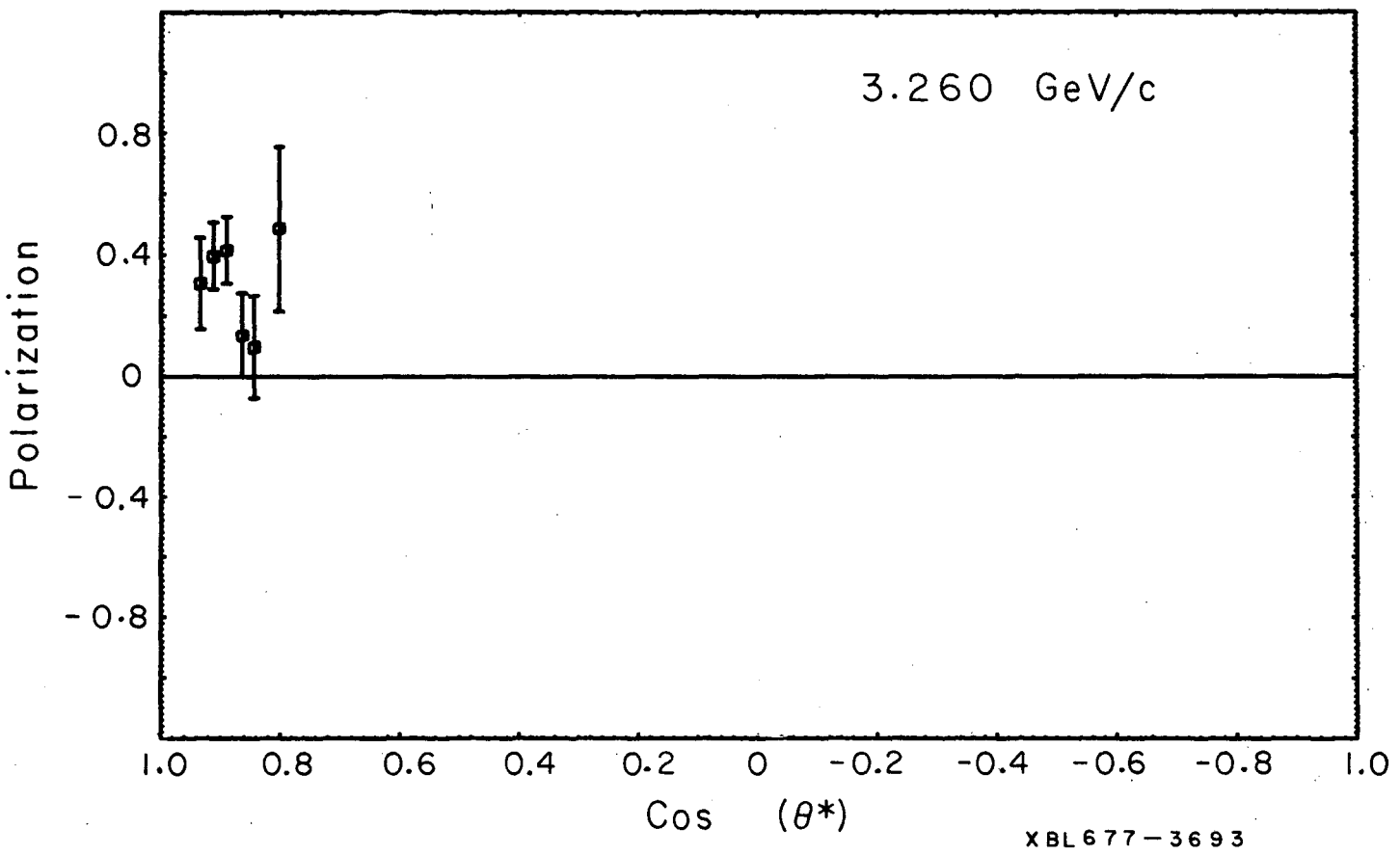

Fig. 28. Polarization parameter in $\pi^+ p$ elastic scattering for an incident pion momentum of 3.260 GeV/c. The errors shown are statistical only and do not include the ±8% systematic error discussed in Section III-C-3. This systematic error comes from inaccurate knowledge of the target polarization and results in an 8% uncertainty in the scale against which the polarization parameter is plotted.

Table XVIII. Polarization parameter $P(\theta)$ in $\pi^+ p$ scattering. The error $\Delta P(\theta)$ is statistical only and does not include the systematic error discussed in Section III-C-3.

P_{lab}=3.747 GeV/c	T_{lab}=3.610 GeV		E_{cm}=2.817 GeV
Cos θ_{cm}	-t	$P(\theta)$	$\Delta P(\theta)$
.934	.207	.64	.18
.919	.252	.08	.18
.903	.302	.36	.18
.886	.355	.60	.21
.868	.412	.32	.22
.848	.472	.02	.30
.828	.536	-.02	.34

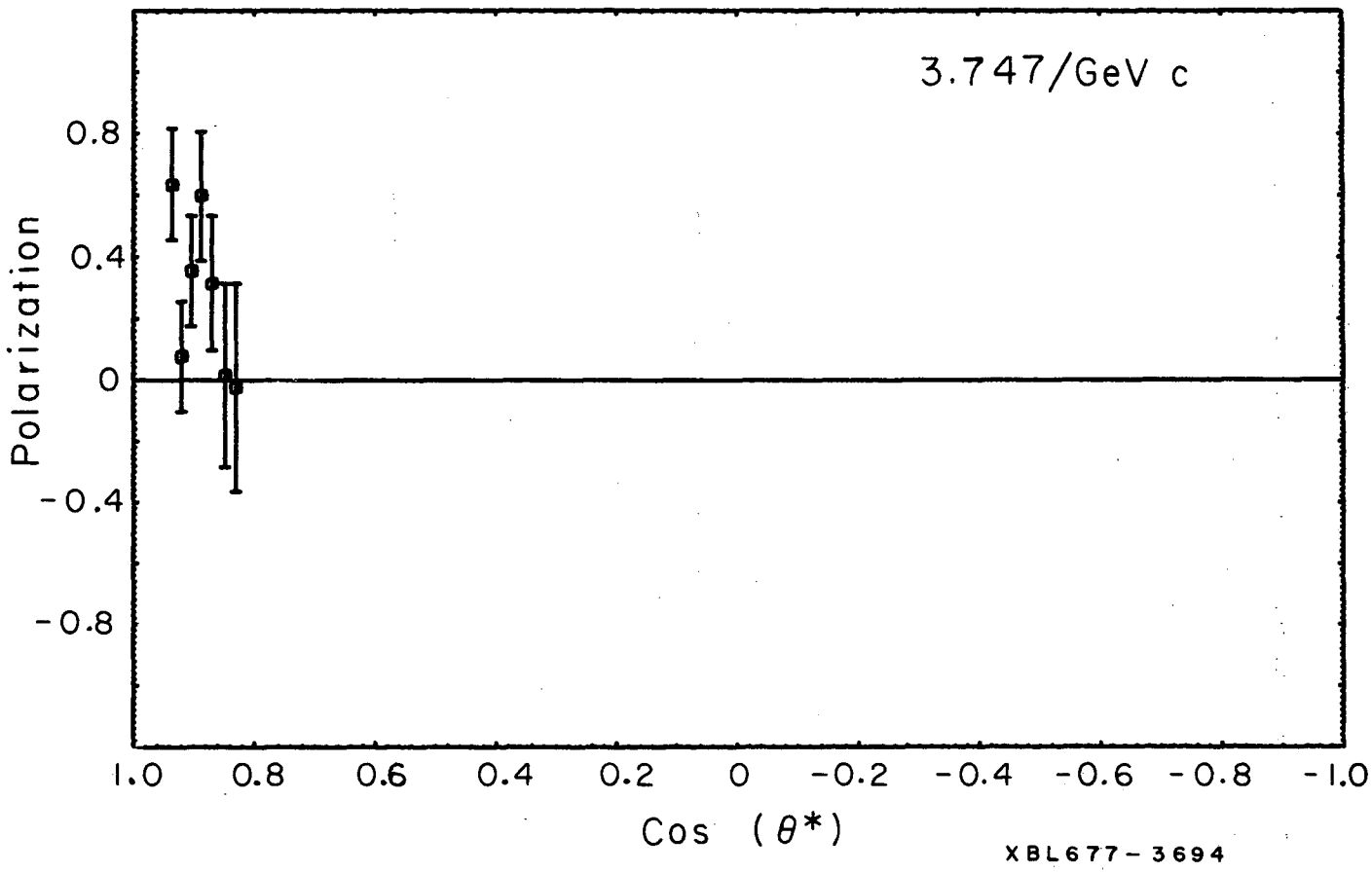

Fig. 29. Polarization parameter in π^+p elastic scattering for an incident pion momentum of 3.747 GeV/c. The errors shown are statistical only and do not include the ±8% systematic error discussed in Section III-C-3. This systematic error comes from inaccurate knowledge of the target polarization and results in an 8% uncertainty in the scale against which the polarization parameter is plotted.

Table XIX. Results of a calibration run which measured the polarization parameter in proton-proton elastic scattering at 1390 MeV/c (kinetic energy = 739 MeV).

θ_{cm} (degrees)	$P(\theta)$	$\Delta P(\theta)$
40	.45	.06
47	.52	.05
56	.53	.05
62	.55	.04
66	.43	.04
72	.35	.05
78	.30	.05
84	.14	.06
90	.01	.08

V. ANALYSIS OF THE RESULTS

A. Formalism

1. Partial-Wave Expansion of the Amplitudes

In non-relativistic notation the wave function of a system involving a single spin-1/2 particle has two components and the corresponding density matrix ρ is a two-by-two matrix.[44] The polarization $\vec{P}$ of the spin-1/2 particle is related to ρ by

$$\rho = \frac{\text{trace}\,\rho}{2} \; (1 + \vec{P}\cdot\vec{\sigma}), \qquad \text{(V-1)}$$

where $\vec{\sigma}$ is the Pauli spin operator. Let M denote the two-by-two transition matrix which takes the πN system from its initial state into its final state. It is easy to show that if parity is conserved in this transition, the most general form M can have is

$$M = f + g\,\vec{\sigma}\cdot\hat{n}\ , \qquad \text{(V-2)}$$

where f and g are complex-valued functions of energy and angle, and $\hat{n}$ is the normal to the plane of the reaction defined in Section II. This follows from the fact that since there is no change in intrinsic parity between the initial and final states, M must be a scalar rather than a pseudoscalar. Thus terms like $\vec{\sigma}\cdot\hat{k}_i$ or $\vec{\sigma}\cdot\hat{k}_f$ which change sign under parity inversion cannot appear in M. In fact the only scalar terms which can be constructed from the available kinematical quantities are the two in (V-2). The initial and final state density matrices are related by M according to

$$\rho_f = M\rho_i M^\dagger. \qquad \text{(V-3)}$$

Now the differential cross section, I, averaged over the final-state polarizations is in general

$$I = \text{trace } \rho_f. \qquad \text{(V-4)}$$

And if there is no initial-state polarization, (V-1) gives that ρ_i, normalized to unit intensity, is simply 1/2 times the two-by-two identity matrix. It follows from (V-3 and -4) that

$$I_o = |f|^2 + |g|^2. \qquad \text{(V-5a)}$$

But starting with the polarized initial state

$$\rho_i = 1/2(1 + \vec{P}_T \cdot \vec{\sigma}),$$

one obtains from (V-1 through -5) that

$$I = I_o(1 + P\vec{P}_T \cdot \hat{n}),$$

which is equation (II-2), and that

$$I_o P = 2 \text{ Re} f^* g. \qquad \text{(V-5b)}$$

Equations (V-5) are the basic relation between the currently available experimental results and the functions f and g, called the "non-spin-flip amplitude" and the "spin-flip amplitude", respectively. The spin rotation parameters mentioned in Section I can be expressed as combinations of $|f|^2 - |g|^2$ and $\text{Im} f^* g$, but they have not been experimentally measured yet.

Table XX. Scattering amplitudes for elastic pion-nucleon reactions.

Process	Amplitude
$\pi^+ + p \to \pi^+ + p$	$M_+ = f_+ + g_+ \vec{\sigma}\cdot\hat{n} = M^{3/2}$ $f_+ = f^{3/2}$ $g_+ = g^{3/2}$
$\pi^- + p \to \pi^- + p$	$M_- = f_- + g_- \vec{\sigma}\cdot\hat{n} = \frac{1}{3} M^{3/2} + \frac{2}{3} M^{1/2}$ $f_- = \frac{1}{3} f^{3/2} + \frac{2}{3} f^{1/2}$ $g_- = \frac{1}{3} g^{3/2} + \frac{2}{3} g^{1/2}$
$\pi^- + p \to \pi^o + n$	$M_o = f_o + g_o \vec{\sigma}\cdot\hat{n} = \frac{\sqrt{2}}{3} (M^{3/2} - M^{1/2})$ $f_o = \frac{\sqrt{2}}{3} (f^{3/2} - f^{1/2})$ $g_o = \frac{\sqrt{2}}{3} (g^{3/2} - g^{1/2})$

The fact that the three processes of (I-1) are all observed can be taken into account by indexing all of the above by +,-, or o to indicate the charge state in question. Thus one has f_+, f_-, f_o; g_+, g_-, g_o; etc. But if the interaction is invariant under I-spin, only four of these amplitudes are independent, since the πN system can have $I = 1/2$ or $3/2$ only. The relations are given in Table XX.

The energy dependence and angle dependence of the amplitudes can be separated by expanding f and g into series of partial-wave amplitudes:[45]

$$f^I = \frac{1}{k} \sum_{\ell=0}^{\infty} \left[(\ell + 1)\, T^I_{\ell\pm} + \ell T^I_{\ell\pm} \right] P_\ell(\cos\theta)$$

$$g^I = \frac{i}{k} \sum_{\ell=1}^{\infty} \left[T^I_{\ell+} - T^I_{\ell-} \right] P^1_\ell\ (\cos\theta). \qquad \text{(V-6)}$$

Here k is the momentum and θ the scattering angle in the center of mass. $T^I_{\ell\pm}$ is the partial-wave amplitude corresponding to the πN state with isotopic spin I, orbital angular momentum ℓ, and the total angular momentum $J = \ell + 1/2$ or $\ell - 1/2$. P_ℓ is the ordinary Legendre polynomial, and P^1_ℓ is the first associated Legendre polynomial.

$$(P^1_\ell\ (\cos\theta) = \sin\theta \frac{d}{d(\cos\theta)}\ P_\ell(\cos\theta).)$$

The use of expansions (V-6) in practice depends on the assumption that their convergence is sufficiently rapid that they can be replaced by finite sums, taken to some relatively small ℓ_{max}. It is the short-

range character of the strong interactions which makes this plausible. If that range is r, then states with ℓ large enough that $kr \ll \ell$ should not contribute significantly to the scattering amplitudes because of the centrifugal barrier. Their T_ℓ should be negligible. It is reasonable to assume in πN interactions that r is $\lesssim$ 1 fermi = $(197\ \text{MeV/c})^{-1}$ since the longest range force should involve the exchange of two pions. So $\ell_{max} \approx k/197$ (with k in units of MeV/c) is an estimate of the number of terms needed in (V-6). Taken literally, this gives $\ell_{max} = 4$ at about pion lab kinetic energy $T_\pi = 1600$ MeV (or lab momentum $P_\pi = 1734$ MeV/c, or total c.m. energy M = 2040 MeV), and $\ell_{max} = 5$ at $T_\pi = 2340$ ($P_\pi = 2475$, M = 2356).

The T's are complex-valued functions of energy (or momentum) only and are usually parameterized each by two real-valued functions of energy. Suppressing indices for clarity, we write

$$T = \frac{\eta e^{2i\delta} - 1}{2i} \qquad \text{(V-7)}$$

The η's and δ's, which are also indexed by I, ℓ, and J, are called absorption parameters and phase shifts, respectively.[1] Unitarity restricts η to lie in the range 0 to 1. This fact and the form of (V-7) dictate that in the complex plane T always lies on or within a circle of radius 1/2, centered at 0 + 1/2i. This circle is called the unitary circle and its plot, an Argand diagram.

Discussion of the behavior of amplitudes on such diagrams can

be found in the literature,[1] but an essential point to mention here is that when a particular partial-wave amplitude passes through a resonance, its trajectory traverses the top of a roughly circular arc on its Argand plot. Furthermore, causality (the "Wigner Condition"[46]) requires that the motion be in a counter-clockwise direction with increasing energy. If the resonance is perfectly elastic, that arc coincides with the unitary circle itself. This is the case with the resonance in the P_{33} partial wave at 1236 MeV. (Here the notation is spectroscopic -- S, P, D, F, G,... for ℓ = 0, 1, 2, 3, 4,... -- and the subscripts give 2I and 2J. D_{35}, for instance, has ℓ = 2, I = 3/2, J = 5/2.) In general, however, the resonance arc may lie anywhere within the unitary circle, and δ need not pass through 90° at the resonance energy.

The ultimate goal of a phase shift analysis is to discover the behavior of these partial-wave amplitudes. Equations (V-5 through -7) express the relation between them and the experimental data. In general, finding a solution entails finding a behavior which is consistent with all the data. How such a solution can be constrained, searched for, and tested for uniqueness will be discussed in Section V-B.

2. Legendre Expansion of the Observables

An alternate approach to finding out how the individual partial waves are behaving begins with direct Legendre expansion of the data itself. One varies the (dimensionless, real-valued) coefficients

A_i and B_i in the series

$$I_o = \lambda\!\!\!^{-2} \Sigma A_i P_i(\cos\theta)$$
$$I_o P = \lambda\!\!\!^{-2} \Sigma B_i P_i^1(\cos\theta) \qquad \text{(V-8)}$$

to obtain best fits to the existing data. Here $\lambda\!\!\!^{-} = k^{-1}$ is the incident c.m. wavelength/2π. The A_i and B_i are quadratically related to the T's of the last section. (These relations are explicitly listed in, for instance, Reference 1.)

Examination of these coefficients' behavior with energy, given some a priori knowledge about how a few of the partial wave amplitudes are behaving, allows one to make certain general statements about other specific amplitudes. This can sometimes give good evidence toward determining the quantum numbers of resonances already located,[49,50] but it is not as quantitative an approach as that reviewed in the last section. It also suffers from the difficulty that when the data is not available at all angles, as is often the case with the results of polarization measurements, the B_i are hard to determine in a straightforward way. The "fit" obtained will often predict impossibly large values of P at angles where there is no data. Introduction of fictitious data ($P = 0. \pm 1.$) at these angles helps to constrain the fit to be more reasonable but prejudices the result at least somewhat. Still, this was the solution used in obtaining the fits reported below to the data of this experiment.

B. Phase-Shift Analysis

1. Basic Approach

Different groups have used different methods and constraints to try to determine uniquely the behavior of the partial-wave amplitudes $T^{I}_{\ell\pm}$. Roper[27] has done an energy-dependent analysis up to T_π = 700 MeV. The most significant result of this pioneering analysis was his discovery of the "Roper" resonance in the P_{11} amplitude somewhere around M = 1400 MeV. He parametrized the non-resonant phase shifts by power series in k and used Breit-Wigner forms for the resonant amplitudes.

Two groups, Bransden *et al*[29] and Donnachie *et al*,[25,26] have since in various ways used the information obtained from partial-wave dispersion relations to help constrain the problem and extend the analysis to higher energies. The latter group has reported[26] several variants of a solution to energies as high as T_π = 1308 MeV (M = 1900 MeV).

Bareyre *et al*[23] used an approach which was energy independent at the first step. They found fits to the data at each of 13 energies between T_π = 310 and T_π = 990 MeV. These fits include S, P, D, and F waves at all 13 energies and G waves at the two highest energies. No *a priori* energy-dependent restriction was put on these fits; but after they were obtained, the particular fit to be included in the final solution was selected by the requirement that each partial wave amplitude exhibit reasonable continuity from one energy to the next. The argument for the uniqueness of the final result was that at the lowest energy the solution is unique, and in extending it upward in energy, no

alternate set of fits could be found to give continuity. The result showed resonances near the π^+p total cross section bump at T_π = 600 MeV (M = 1512 MeV) in all three of the amplitudes S_{11}, P_{11}, and D_{13}. And there were resonances contributing to the π^-p cross section bump at T_π = 900 MeV (M = 1688 MeV) and the π^+p cross section "800 MeV shoulder" in all four of S_{11}, D_{15}, F_{15} and S_{31}.

The analysis whose preliminary results are reported here most closely follows the approach of Bareyre. At each of some 19 energies, initial guesses for values of the η and δ parameters were obtained in ways described below. Then these parameters were varied in an attempt to get a good fit to the data at that energy by minimizing the scalar quantity

$$\chi^2 = \sum \left[\frac{(\epsilon Q_{meas} - Q_{calc})}{(\epsilon \Delta Q_{meas})} \right]^2 . \qquad \text{(V-9)}$$

Here Q represents some observable -- π^+, π^-, or charge-exchange differential cross section, or π^+ or π^- polarization. Q_{meas} is the measured value of that observable at a given energy and angle; Q_{calc}, the calculated value from the given η's and δ's at the same energy and angle. ϵ is a scaling parameter which was allowed to vary around 1 to account for normalization errors in a given experiment. ϵ could vary from one experiment to another, but was fixed for all data from a given experiment at a given energy. The sum is over all data available at or near a given energy. This is typically 80-100 points at a variety

of angles, invoving five types of experiments and five or six actually distinct experiments. (There could be two overlapping π^+ DCS measurements, for example. Further discussion of the data available is in the next section.)

The computer program used to minimize χ^2 is named ORPHEUS and is basically the variable-metric minimization scheme VARMIT.[51] This program makes use of χ^2, the gradient of χ^2, and the inverse of its second-derivative matrix. The first two quantities are calculated explicitly at each step of the iteration. The third is constructed during the minimization process by a method of successive approximations. Information from all three sources is used to predict the size and direction of the next iteration step. Besides being quite efficient, this scheme has the advantage that at the end of the process a good approximation to the complete error matrix is available for calculating correlations among the errors in the different parameters.

Initial guesses for input to ORPHEUS were obtained in three ways. The first started with a rather coarse survey conducted with a ravine-following minimization method operated with fixed step-length in a search mode. By this is meant that the program used information accumulated from several successive evaluations of χ^2 and its gradient to predict the direction it should move in the parameter space to select the next point for evaluation. Each such move or "step" was over a fixed distance in terms of a metric on the parameter space and was calculated to follow the curvature of the contours of constant χ^2 in that parameter space. The term "search mode" refers to the fact that the program was required to continue to step forward once it had established a general direction in which χ^2 tended to decrease. Even if χ^2 eventually began to increase in this direction, the steps were not completely reversed. Instead the program was instructed to follow the contour along which χ^2 seemed to increase least rapidly. This procedure was designed to allow the program from each start to step through and compare several successive relative minima in χ^2. At each energy these searches were started at points chosen randomly in the general vicinity of the solutions published by Bareyre[23] and Lovelace.[26] This restriction was imposed mainly to conserve computer time by making it more likely that the search program could find an acceptably small relative minimum of χ^2 in its prescribed number of steps. Initial values of the absorption parameters (η's) were chosen randomly in the region ranging from $\pm.1$ to $\pm.4$ around their values in the Bareyre and

Lovelace solutions. The phase-shift parameters (δ's) were chosen from a region ranging from $\pm 20^{\circ}$ to $\pm 90^{\circ}$ in a similar manner. The amount of variation allowed depended on the energy and the orbital angular momentum of the partial-wave amplitude involved. In general, lower partial waves (smaller ℓ) and higher energies were given the most latitude.

Some 40 to 120 starts (Table XXII) were made at each energy in this survey. The point with best χ^2 found along the path of 75 to 100 iteration steps after each such random start was then used as input to ORPHEUS. After a relatively brief effort to improve the χ^2 of all these cases (about 40 sec of 6600 computer time per case), the best candidates were selected for more intensive (2-3 min/case) minimization efforts. Final selection of acceptable fits from each set of cases at each energy was based on comparison of the final χ^2 to the number of degrees of freedom corresponding to the number of data used and to the other cases' χ^2's obtained under the same conditions. There were wide variations in the amount of change in the values of the parameters between an initial random start and a final acceptable fit obtained in this way.

The second source of initial guesses was fits obtained in the above way at energy E_n, but submitted as starting points for ORPHEUS using data at energy E_{n+1} or E_{n-1}. Initial χ^2 for such a start was usually at least an order of magnitude better than that of a purely random start and roughly comparable to that obtained in a start taken from the output of the crude ravine search. Final χ^2 tended to be

acceptable in a somewhat greater percentage of the cases than with the method above, and the amount the parameters changed to achieve a fit at the adjacent energy was comparable to the changes between one energy and the next in a "continuous" solution like Bareyre's.

It should be mentioned, however, that because of variations in how the minimization program takes its first few steps, this procedure is not necessarily guaranteed to find the nearest relative minimum of χ^2 at the adjacent energy. When fits at energy E_n were continued to E_{n+1} and then the resulting E_{n+1} fits resubmitted with E_n data, the original starting point was recovered in only about half of the cases tried.

The third source of ORPHEUS starting points was the solutions published by other groups. Those of Bareyre[23] and of Donnachie,[26] in particular, were used as inputs at each energy of this analysis, and at several energies the resulting fit is the one included in the tentative solution reported below. (See Table XXIV)

2. Data Used in the Search

An analysis of this type would be completely impossible were it not for the great increase in the last few years of the amount of πN data available. In the energy range considered here the contributions have come mainly from Saclay, Rutherford, Argonne, and Berkeley, and have generally been the results of major experimental efforts in which a given observable is measured at a number of energies with the same setup. Efforts have been made to measure the different observables at the same energies so there would be complete sets of data at specific points. At the present time a "complete" set consists of only five types of experiments, however. The spin rotation parameters have not been measured at all, and only a few data points exist for charge-exchange polarization.

The points at which this analysis was carried out were chosen for their availability of complete or nearly complete sets of data. Though some new data has been published [16,21] since the analyses of Bareyre or Donnachie, the points used here are not different from those of earlier analyses, except that two high-energy points have been added.

The specific energies chosen for analysis and the data used in each case are listed in Table XXI. Except for the interpolation of some charge-exchange differential cross section data mentioned below, none of the data was edited or corrected in any way. The only prejudice exercised was which of the experiments to use in the fits at a

Table XXI. Data used in the phase-shift analysis. The entries are: pion kinetic energy(reference).

Nominal T_π (MeV)	Differential Cross Sections π^+	π^-	Ch.Exch.	Polarizations π^+	π^-
490	490(12)	490(12)	500(16)	492(20)	492(20)
					472(21)
550	550(12)	550(12)	533(16)		546(21)
581	581(11)	581(11)	592(16)	572(19)	572(19)
600	600(12)	600(12)	588(14)	619(21)	619(21)
650	650(12)	650(12)	655(16)	619(21)	619(21)
698	698(11)	698(11)	704(16)	689(19)	692(21)
					689(19)
747	747(13)	747(13)	755(14)	766(21)	766(21)
					747(18)
796	796(13)	796(13)	796*(14)	766(21)	796(18)
845	845(13)	845(13)	845*(14)	864(19)	845(18)
870	870(13)	870(13)	875(16)	864(19)	864(19)
900	900(13)	900(13)	900*(16)	894(21)	900(18)
949	949(13)	949(13)	949*(16)	953(21)	949(18)
990	990(11)	990(11)	975(16)	981(19)	981(19)
1049	1049(13)	1049(13)	1049*(16)	1024(21)	1024(21)
1148	1148(13)	1148(13)	1117(16)	1152(21)	1148(18)
			1151(14)		
1228	1228(13)	1228(13)	1228*(16)	1220(21)	1220(21)
1307	1311(11)	1307(13)	1300(16)	1308(21)	1307(18)
				1301(19)	
1446	1446(13)	1446(13)	1446*(16),(17)	1439(21)	1446(18)
1566	1545(11)	1566(22)	1581(17)	1556(21)	1566(22)

* data interpolated to this energy

few of the energies where there were duplications. Where both groups reported results, the charge-exchange data of Ref. 16 was preferred to that of Ref. 14. And at T_π = 870 MeV where the π^+ and π^- cross sections of Ref. 11 and Ref. 13 are in some disagreement, the latter was used. At all other points all the available data were used.

When only the four types of data--π^+ and π^- differential cross sections and π^+ and π^- polarizations--were available at a given energy, and charge-exchange differential cross section data were available at energies on both sides, the fifth type was created artificially by interpolation. Simple linear interpolation was used on both the data points and the errors. This was thought preferable to the alternative of conducting searches with only four experiments for two reasons. First the number of different statistically good fits to the data is much reduced by the added constraints of the additional data. Second, without some information about the charge-exchange cross section, the fits often predicted irrational values for it. Such interpolation was used only for charge-exchange differential cross section and only at the seven points listed in Table XXI. No interpolation in angle was necessary because in this energy range data of this type has been reported by all groups at fixed intervals of center-of-mass angle.

The number of degrees of freedom listed in Table XXI for each energy is the total number of measurements minus the number of parameters allowed to vary in the search. All the fits in the analysis reported here were through G waves (ℓ_{max} = 4), and involved both

I-spins. So the number of parameters is $4(2\ell_{max} + 1)$ + number ϵ's = 41, for a typical case of five experiments. In this analysis none of these parameters was restricted in any way (except that η was required to lie between 0 and 1) other than by the data and χ^2.

The total number of "measurements" listed in Table XXI includes four which correspond to the real and imaginary parts of the I=1/2 and I=3/2 amplitudes. The imaginary parts, by the optical theorem, come essentially from total cross section measurements. The real parts are not measured directly, but are obtained by dispersion-relation calculations. The values used of both real and imaginary parts were taken from Ref. 47.

The number of measurements also includes the number of scaling parameters (ϵ's) involved at that energy--four to six depending on the number of experiments used in the search. These ϵ's are treated by the program both as data to be fit and as parameters to be varied. As data they are taken to be $1 \pm \Delta\epsilon$, where $\Delta\epsilon$ is the systematic error reported by the experimenter. (If no systematic error was reported, $\Delta\epsilon$ was taken to lie between .10 and .05, depending on the type of experiment.) As parameters they are used in the calculation of χ^2 and its gradient and in general treated by the program on the same footing as the η's and δ's. Because of their dual role of data and parameters, the number of ϵ's does not affect the number of degrees of freedom.

3. Energy Independent Results

The number of different starting points for χ^2 minimization at each energy are listed in Table XXII. At all except the two highest energies all of the three methods described above were used to select those starts. At T_π = 1446 MeV starts were made only from some of the acceptable fits at 1307 MeV. And in turn only the results of these starts (not all of which were good fits) were used as input at 1566 MeV.

The number of good fits listed in XXII is intended to give an idea of the amount of ambiguity involved in a search of this type and is not to be considered the total number of fits that might possibly be found. It is simply the number which have been found as of this writing (July, 1967). At each energy these fits all have comparable χ^2. (The range from best to worst is ten to twenty.) And all are distinct not only in the sense that they will not converge no matter how long the minimization program works on them, but also in that they differ by significant amounts. By this last is meant amounts comparable to (or greater than) that between fits at adjacent energies in a final "continuous" solution, like Bareyre's or the one reported below.

As a quantitative measure of this distance between fits we have used a metric based on the separation of the amplitudes on the Argand diagrams. Consider each amplitude to be plotted on a separate diagram and each diagram to contribute two dimensions to a $4(2\ell_{max} + 1)$-dimensional Euclidian space. The distance between two fits is taken to be the Cartesian distance between the points they occupy in this space. The normalization used is such that two diametrically opposite fits --

Table XXII. Energy independent phase-shift results. The symbols are defined in the text.

T_π (MeV)	P_π (MeV/c)	M (MeV)	Number of starts	Number of fits	best χ^2	DF	best χ^2 / DF
490	614	1443	42	6	79.2	58	1.37
550	675	1481	50	15	64.7	49	1.32
581	707	1501	75	35	59.2	41	1.44
600	726	1512	65	30	53.8	65	.83
650	777	1543	60	31	65.9	63	1.05
698	826	1572	66	30	68.6	67	1.02
746	875	1601	71	28	76.2	77	.99
796	925	1629	110	47	45.6	51	.90
845	975	1658	58	33	48.9	54	.91
870	1000	1672	103	31	46.7	50	.93
900	1030	1688	96	27	41.1	54	.76
949	1080	1716	49	13	52.9	53	1.00
990	1121	1738	76	24	47.8	54	.89
1049	1180	1769	42	7	75.6	65	1.16
1148	1280	1821	41	14	70.5	65	1.09
1228	1360	1862	42	13	79.1	69	1.15
1307	1440	1901	55	23	84.8	71	1.19
1446	1579	1968	26	12	61.9	68	.91
1566	1700	2025	13	6	82.2	83	.99

that is, two fits which have all η's equal to 1 and corresponding δ's differing by 90° -- are taken to be 100 units apart.

In terms of this distance, fits at a given energy can be regarded as distinct if they are more than about three to five units apart (depending on their energy). And fits at adjacent energies (separated by about fifty MeV) in a "continuous" solution will be typically 8-12 units apart in the energy range considered here. By no means all the distances encountered are this small, however. With a few exceptions it is true that at each of the energies in Table XXII almost equally good fits have been obtained, in terms of χ^2, that are more than 25 units apart. Such fits are radically different in most of their partial waves, and usually predict very different values for unmeasured observables -- specifically the charge-exchange polarization.

The "best χ^2" listed in Table XXII is simply the best found at each energy to date. It is intended to convey some idea of the quality of the fits at one energy relative to that of fits at another, but cannot be taken too literally in this respect. Usually, at an energy where χ^2 is significantly greater than expected, most of the contribution comes from two or three well-defined data points. All the different fits at such an energy will fail at the same few data. It seems more reasonable to regard these points as being themselves in error than all the fits intrinsically bad.

The best χ^2 found at each energy does seem to be a meaningful guide for judging the acceptability of other fits at that energy, however. Slight changes in the data, such as the substitution of the charge-

exchange data of Reference 16 for that of Reference 15, can affect χ^2 by as much as 10-15. (Reference 15 is a preliminary report and Reference 16 a final report on the results of the same experiment.) But such changes affect all the χ^2's in a given set of fits in generally the same way. Fits which had relatively bad χ^2's with the old data are still relatively bad with the new. So the selection of the fits listed in Table XXII is based on their statistical merit relative to the best fit obtained at each energy rather than to an absolute scale. The fits in each set were run under identical conditions to make it meaningful to compare their χ^2's, the distribution of χ^2's was plotted, and fits which were more than 10 to 20 worse than the best were discarded.

The differences among the fits at a given energy are most noticeable in the lower partial waves, particularly S and P. It was found that no matter where an F or G wave amplitude was started, the minimization process would move it back to near zero (except at energies where resonances could be expected). But usually fits could be found whose S and P amplitudes, especially in the I = 1/2 state, were distributed over the entire unitary circle. The inability of the data to determine these amplitudes very exactly was also evident in their sensitivity to small changes in the data. Modifications like the charge-exchange cross section substitution mentioned above would sometimes move a few of the lower amplitudes a fifth of the way across the Argand plot. (But this would usually correspond to a distance of less than 5 units in the metric defined above, so the distinctions among fits at a given energy would be preserved.) This is an argument against interpreting the mathematically computed errors on these lower waves too literally.

4. Continuation with Energy

The hope in an analysis like this one is that the tremendous ambiguities which result when each energy is considered separately will be reduced or removed by requiring "reasonable" behavior in each amplitude as a function of energy. The problem is to define "reasonable", and then to apply this criterion to the multitude of fits obtained at the various energies.

A minimum requirement for reasonableness is continuity, but in practice this requires the basic assumption that the energies at which individual fits have been made are close enough together that discontinuity will be manifest. Even if this assumption is valid, there remains the job of detecting the continuity. When as many fits as are enumerated in Table XXII are plotted versus energy, the result is hardly enlightening. There appear to be many ways to select one fit from each energy so that a given partial wave will behave smoothly, but it is difficult to get all eighteen to behave smoothly simultaneously, or to tell how many alternate ways there may be to do this.

To quantize the continuity condition so the computer could do the sorting, the distance defined in the last section was used and the additional assumption made that the most continuous path through the maze of fits would be the shortest one. All of the fits were read into the computer and the lengths of the shortest path from a single starting point (taken to be the fit by Donnachie et al at T_π = 450 MeV) to each fit at each energy were calculated. The only restriction placed on which fits could be included in such a path was that there should be one from

each energy between 450 MeV and the termination point.

This is an unsophisticated procedure, but the results are interesting. First of all, the shortest total path from 450 MeV to 1570 MeV gives a solution which has almost all the features of Bareyre's or Donnachie's solutions. The resonances in the D and F waves are clearly present. The S and P trajectories are less smooth, but they at least pass through the same general parts of the unitary circle as do Bareyre's. And their roughness is not much worse than that of the Donnachie solution. The surprising point is that this approximate reproduction of all the resonant behavior previously reported can be obtained from this version of the continuity requirement. One would expect paths which include resonances to be longer than those without them because of the distance amplitudes move in passing through resonance. So, if anything, the selection process used here should be prejudiced against finding resonances. Yet even the loop in the S_{11} amplitude just above the eta threshold is approximately reproduced.

A second point is that the fits selected by the shortest path from the starting point to any of the fits at a much higher energy tend to be the same over most of the path. Thus the shortest path from fit 1 at energy E_1 to any one of fits 1-20 at energy E_n will tend all to pass through, say, fit 4 at E_{n-3}. This says that at least with the collection of fits on hand at the moment, most paths which branch off from the shortest overall path do not continue for very many energies.

When this selection technique was first used on an early collection of fits, all obtained only from the random-starting procedure already

described, no branch path was observed to survive for more than four energies. (The overall result was essentially the same as the one reported here, however.) More recently, after a number of new fits had been obtained by the second starting procedure of trying direct continuation of individual fits to an adjacent energy, several branches have been extended through additional energies. One now extends through ten, departing from the solution reported here at 650 MeV and disappearing after 1050 MeV. The χ^2's of some of the fits along this path are not particularly good and it is not seriously proposed as an alternate solution. The point is that this general search and sort procedure seems to offer a promising base for an extensive investigation of the question of uniqueness.

Another advantage of this sorting technique is that it is easy to test which partial waves are helping most to constrain the solution. Only the definition of distance need be changed. One such test was made by computing the distance as described above except that S waves were completely ignored. Thus continuity in the sense of short path-length depended only on the P, D, F, and G waves. The result was interesting because the result was essentially the same, even including the behavior of the S waves. This is some confirmation that the higher wave (P_{11}, D_{13}, D_{15}, F_{15}, P_{33}, and F_{37}) resonances are really there, even if the behavior of the lower waves is hard to determine with existing data.

The results of this analysis (as they stand at this writing) are plotted in Figs. 30 through 37. The meaning of the symbols used

to plot the points in these figures and a summary of the properties of the fits at the different energies are given in Table XXIV. The numerical values of the parameters at each energy and the mathematical calculation of their errors are given in Table XXV. These errors come directly from the inverse of the χ^2 second-derivative matrix as mentioned in Section V-B-1. But as is also discussed above, they should not be regarded too literally as giving the real uncertainty with which we have determined the solution, even if this solution is basically the correct one. The "epsilons" listed in Table XXV are the scaling parameters, also discussed in Section V-B-1, which were allowed to vary around 1.0 to adjust the normalization of each experiment. At each energy the order in which they are listed is the same as that of the References in Table XXI.

As a convenience in evaluating this solution, the currently accepted properties of the resonances in the πN system are summarized in Table XXIII.[48]

It is to be emphasized that this solution is presented only as an example of the results which have been obtained to date with the search methods discussed above. It is not necessarily the "best" solution in any theoretical sense, nor is it claimed to be unique. The highest-energy points are particularly speculative.

Table XXIII. πN resonances and their properties, taken from Ref. 48.

Mass (MeV)	Width (MeV)	I-spin (I)	Ang. Mom. (ℓ)	Spin-Parity (J^P)	Spectroscopic Symbol
~1400	~200	1/2	1	$1/2^+$	P_{11}
1525	105	1/2	2	$3/2^-$	D_{13}
1570	130	1/2	0	$1/2^-$	S_{11}
1670	140	1/2	2	$5/2^-$	D_{15}
1688	110	1/2	3	$5/2^+$	F_{15}
1700	240	1/2	0	$1/2^-$	S_{11}
2190	200	1/2	4	$7/2^-$	G_{17}
2650	~300	1/2	6?	$11/2^-$?	$I_{1,11}$
3030	400	1/2	8?	$15/2^-$?	$K_{1,15}$
1236	120	3/2	1	$3/2^+$	P_{33}
1670	~180	3/2	0	$1/2^-$	S_{31}
1920	200	3/2	3	$7/2^+$	F_{37}
2420	~275	3/2	5?	$11/2^+$?	$H_{3,11}$
2850	~300	3/2	7?	$15/2^+$?	$J_{3,15}$
3230	440	3/2	9?	$19/2^+$?	$L_{3,19}$

Table XXIV. Summary of the properties of the phase-shift solution presented in Table XXV and Figs. 30-37.

T_π (MeV)	P_π (MeV/c)	M (MeV)	Plot Symbol	X^2	DF	X^2/DF	Source of fit
370	490	1362	01				(a)*
410	532	1390	02				(a)
447	570	1415	03				(a)
490	614	1443	04	86.5	58	1.491	(b)*
550	675	1481	05	86.0	49	1.754	(c)*
581	707	1501	06	64.8	41	1.581	(d)*
600	726	1512	07	62.1	65	.955	(d)
650	777	1543	08	68.2	63	1.083	(b)
698	826	1572	09	68.9	67	1.028	(d)
746	875	1601	10	95.1	77	1.236	(c)
796	925	1629	11	48.7	51	.954	(c)
845	975	1658	12	57.3	54	1.062	(d)
870	1000	1672	13	56.7	50	1.133	(b)
900	1030	1688	14	53.2	54	.984	(c)
949	1080	1716	15	63.0	53	1.188	(c)
990	1121	1738	16	52.6	54	.974	(b)
1049	1180	1769	17	76.9	65	1.183	(b)
1148	1280	1821	18	74.6	65	1.148	(b)
1228	1360	1862	19	79.3	69	1.149	(b)
1307	1440	1901	20	96.0	71	1.353	(d)
1446	1579	1968	21	90.0	68	1.324	(c)
1566	1700	2025	22	92.5	83	1.114	(c)

* (a) Taken directly from Ref. 26.

(b) Found from random start.

(c) Found from continuation from adjacent energy.

(d) Found from start at values of Ref. 23 or Ref. 26.

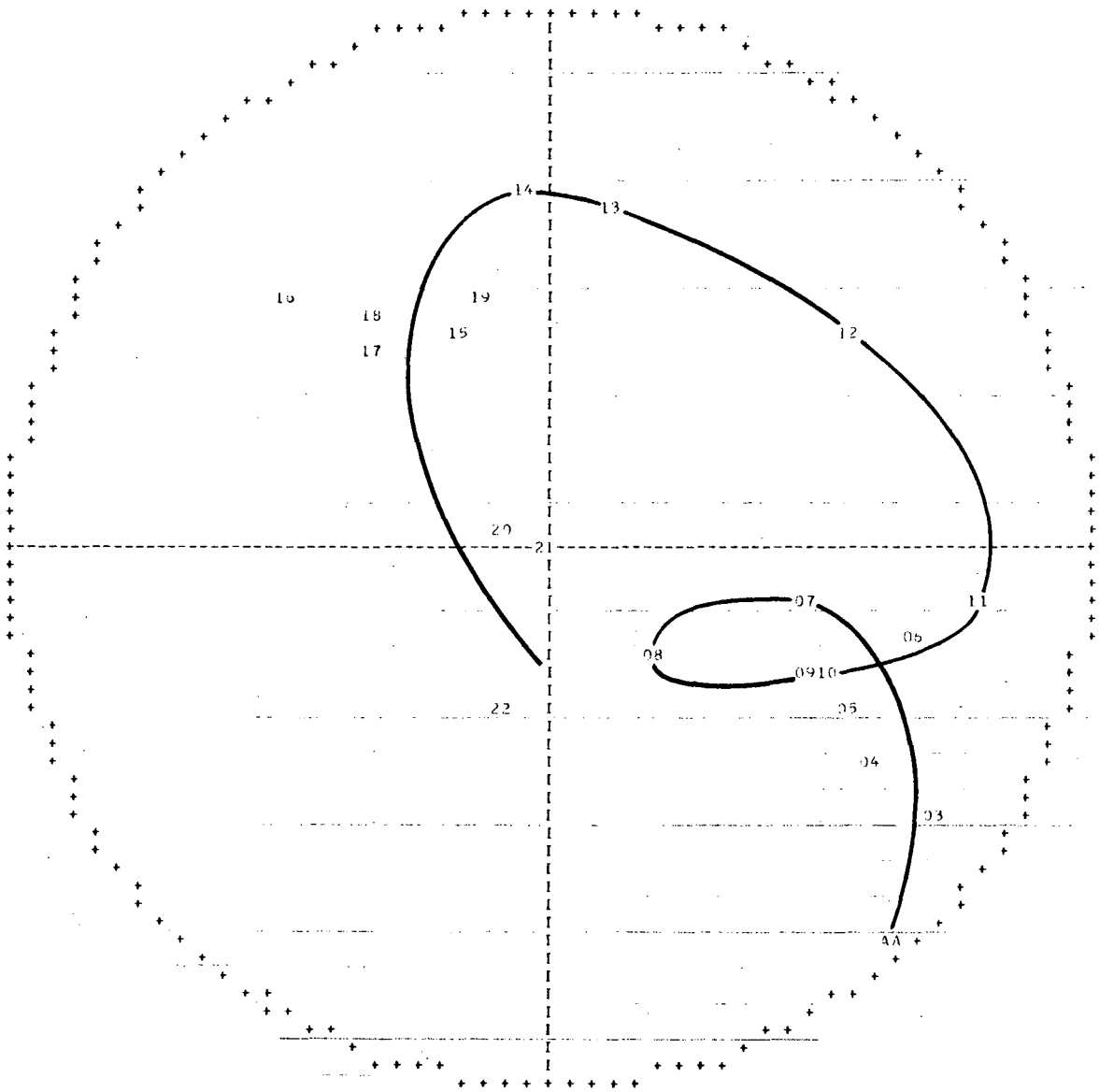

XBL 678-4601

Fig. 30. Argand plot of the energy dependence of the S_{11} πN partial-wave amplitude. Table XXIV gives the energies corresponding to the points plotted; Table XXV, their numerical values and errors. The curve is drawn simply to guide the eye.

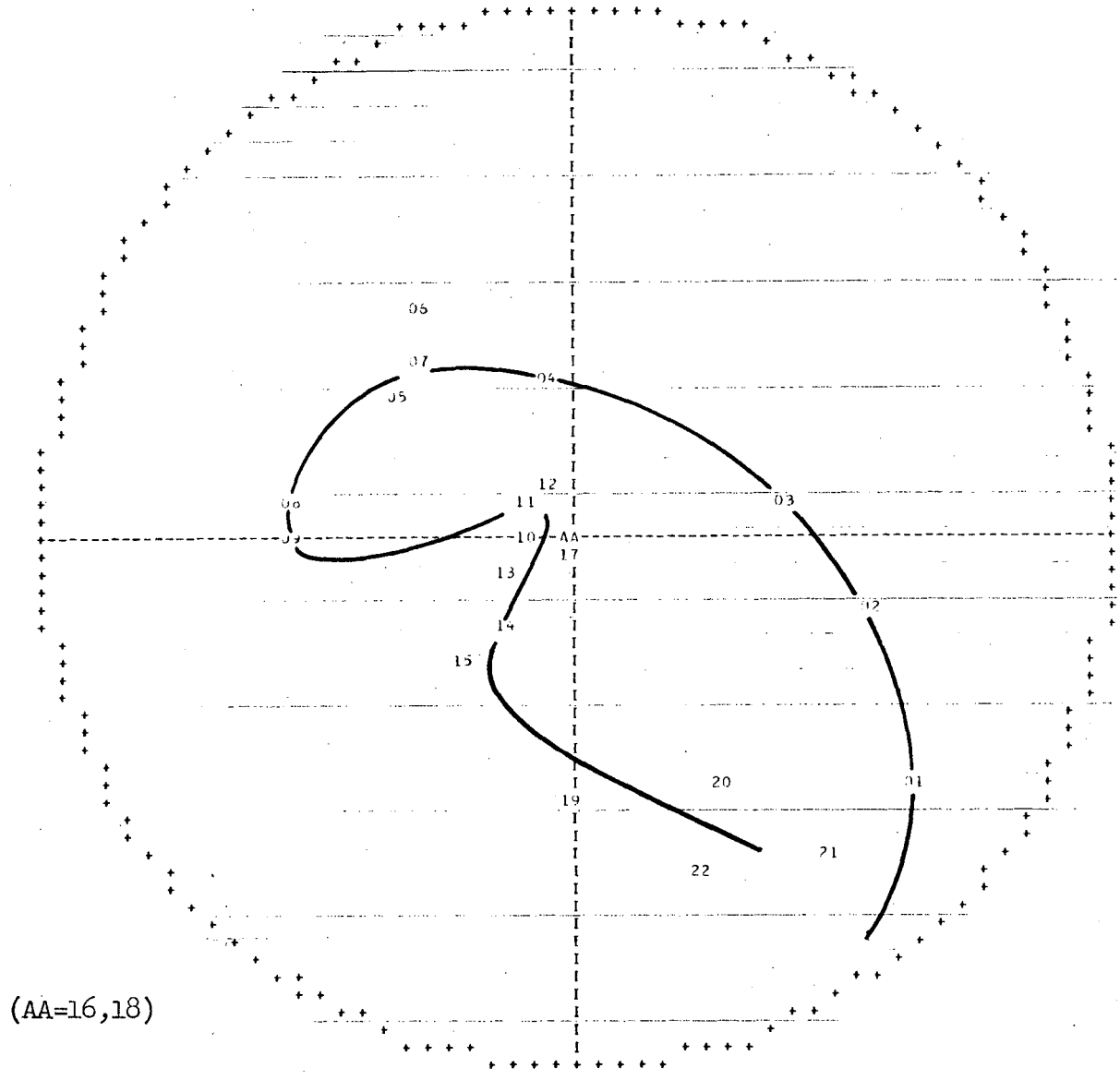

Fig. 31. Argand plot of the energy dependence of the P_{11} πN partial-wave amplitude. Table XXIV gives the energies corresponding to the points plotted; Table XXV, their numerical values and errors. The curve is drawn simply to guide the eye.

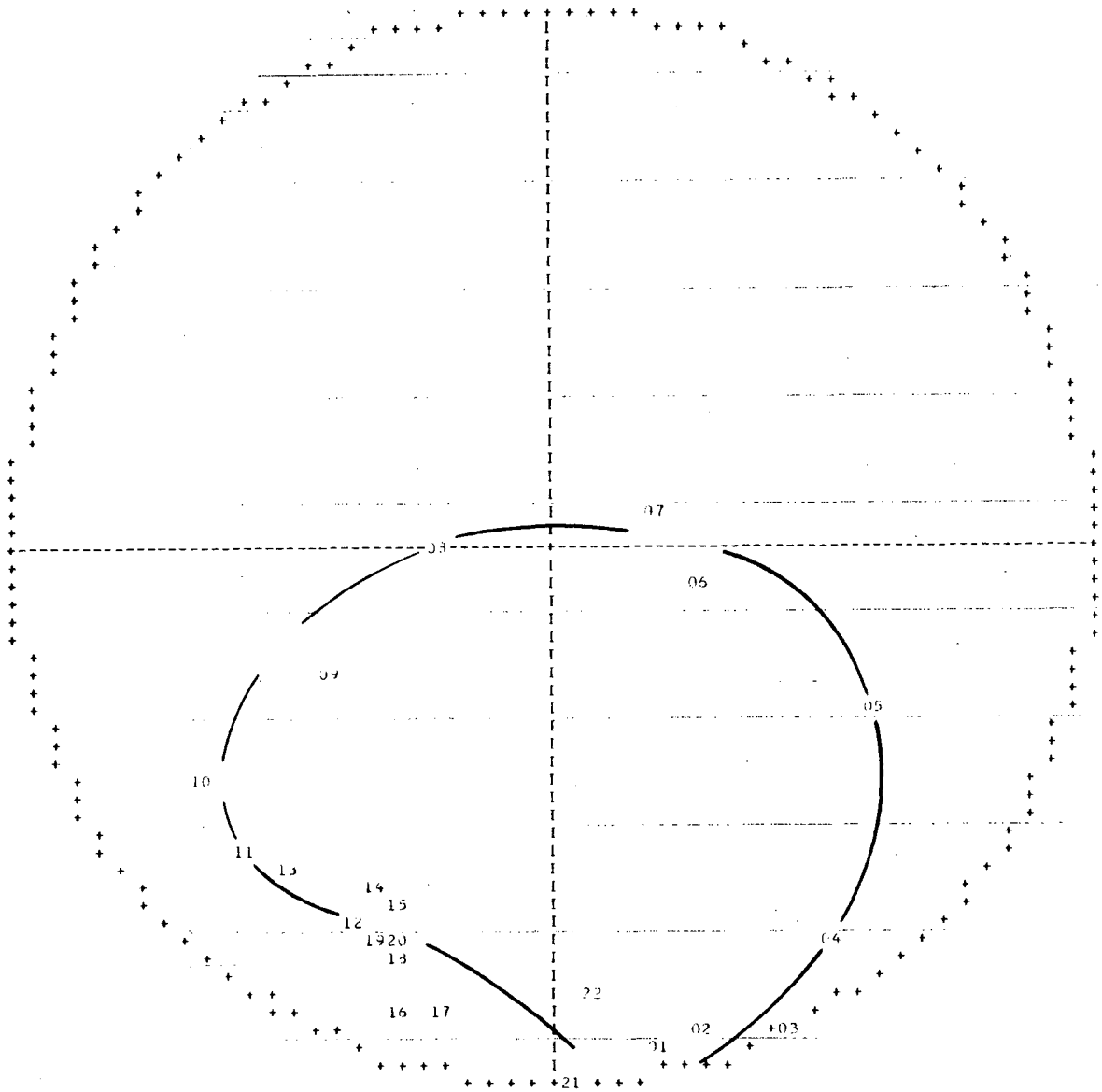

Fig. 32. Argand plot of the energy dependence of the D_{13} πN partial-wave amplitude. Table XXIV gives the energies corresponding to the points plotted; Table XXV, their numerical values and errors. The curve is drawn simply to guide the eye.

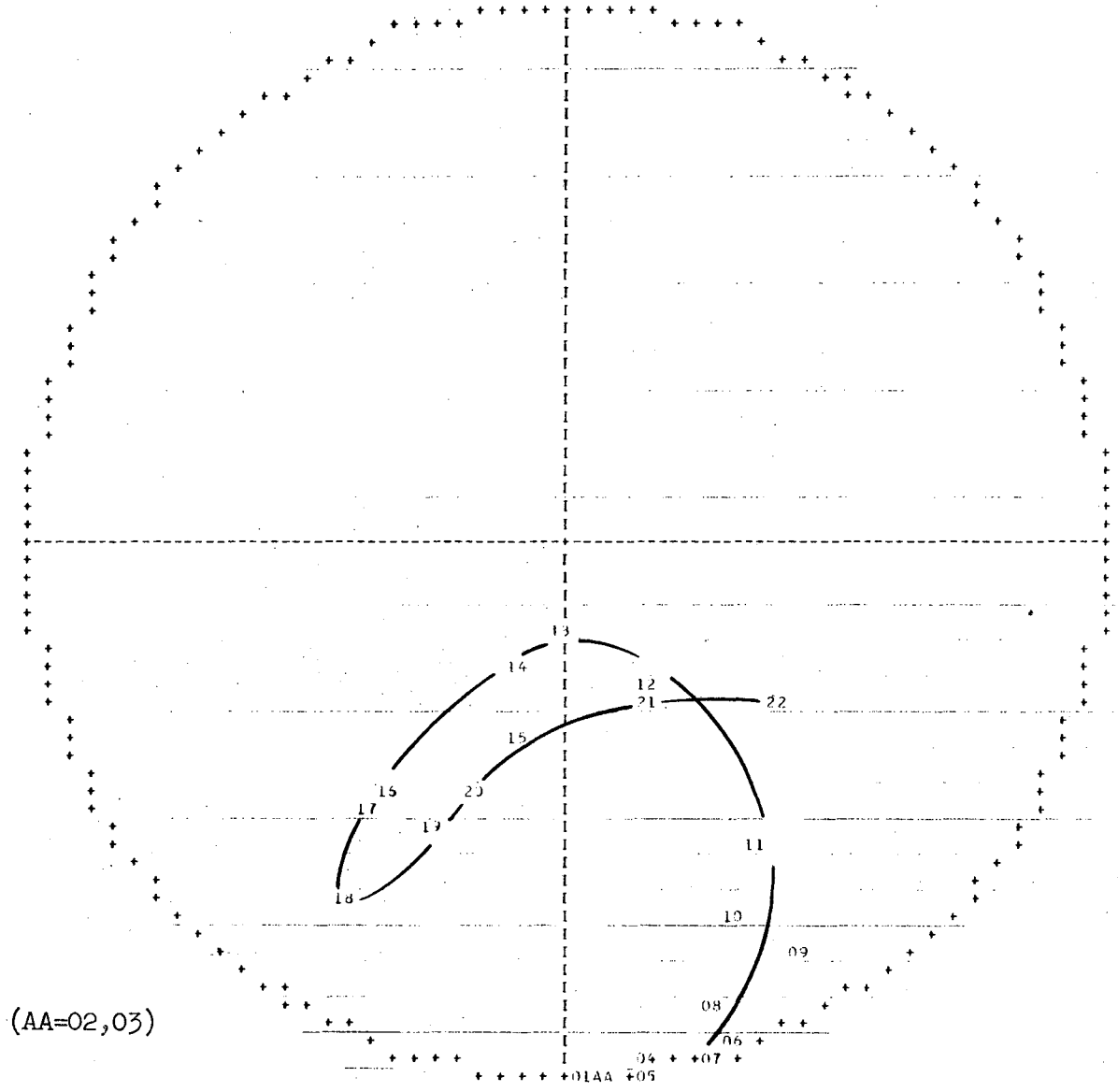

Fig. 33. Argand plot of the energy dependence of the D_{15} πN partial-wave amplitude. Table XXIV gives the energies corresponding to the points plotted; Table XXV, their numerical values and errors. The curve is drawn simply to guide the eye.

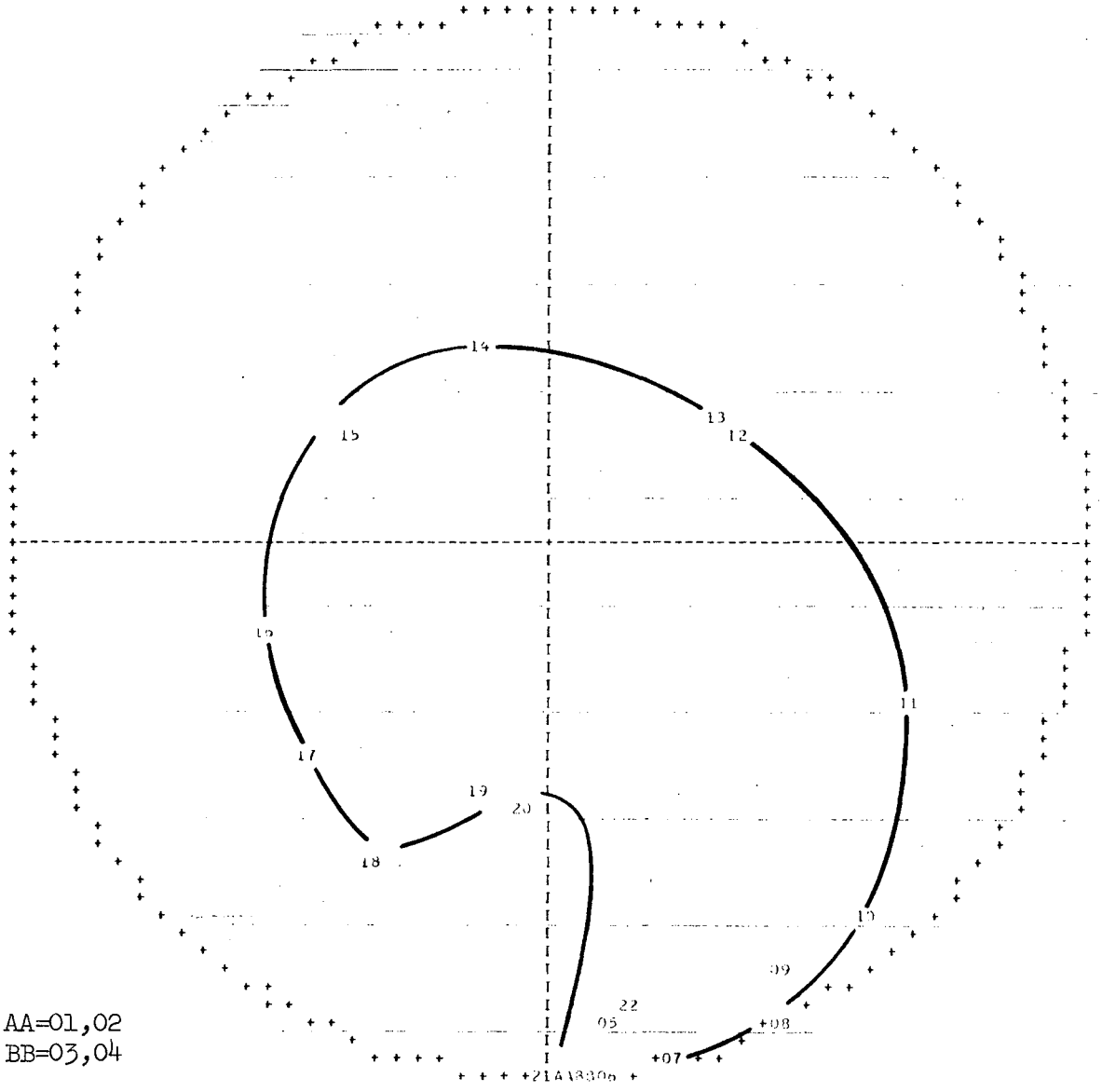

Fig. 34. Argand plot of the energy dependence of the F_{15} πN partial-wave amplitude. Table XXIV gives the energies corresponding to the points plotted; Table XXV, their numerical values and errors. The curve is drawn simply to guide the eye.

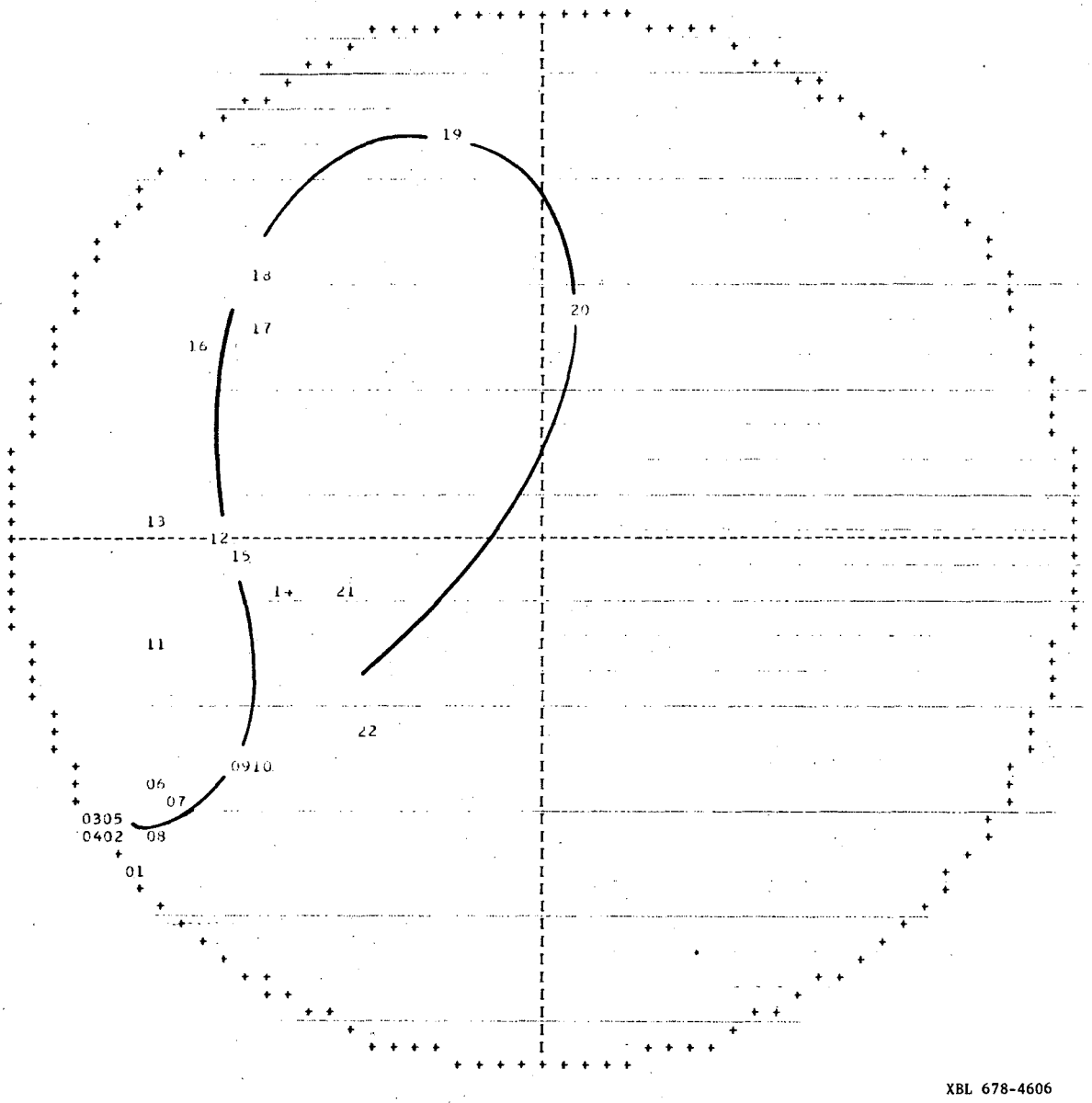

Fig. 35. Argand plot of the energy dependence of the S_{31} πN partial-wave amplitude. Table XXIV gives the energies corresponding to the points plotted; Table XXV, their numerical values and errors. The curve is drawn simply to guide the eye.

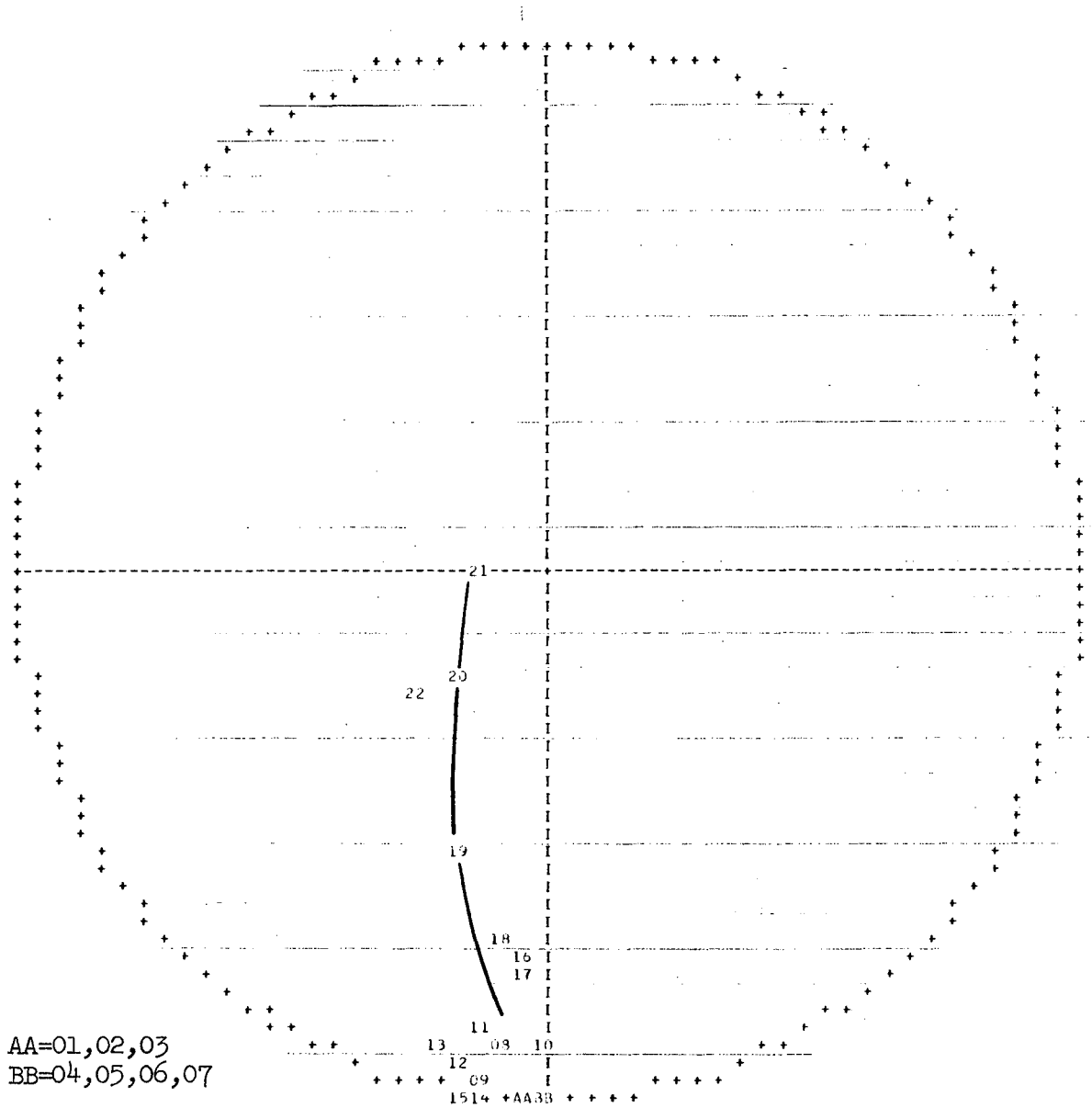

Fig. 36. Argand plot of the energy dependence of the D_{35} πN partial-wave amplitude. Table XXIV gives the energies corresponding to the points plotted; Table XXV, their numerical values and errors. The curve is drawn simply to guide the eye.

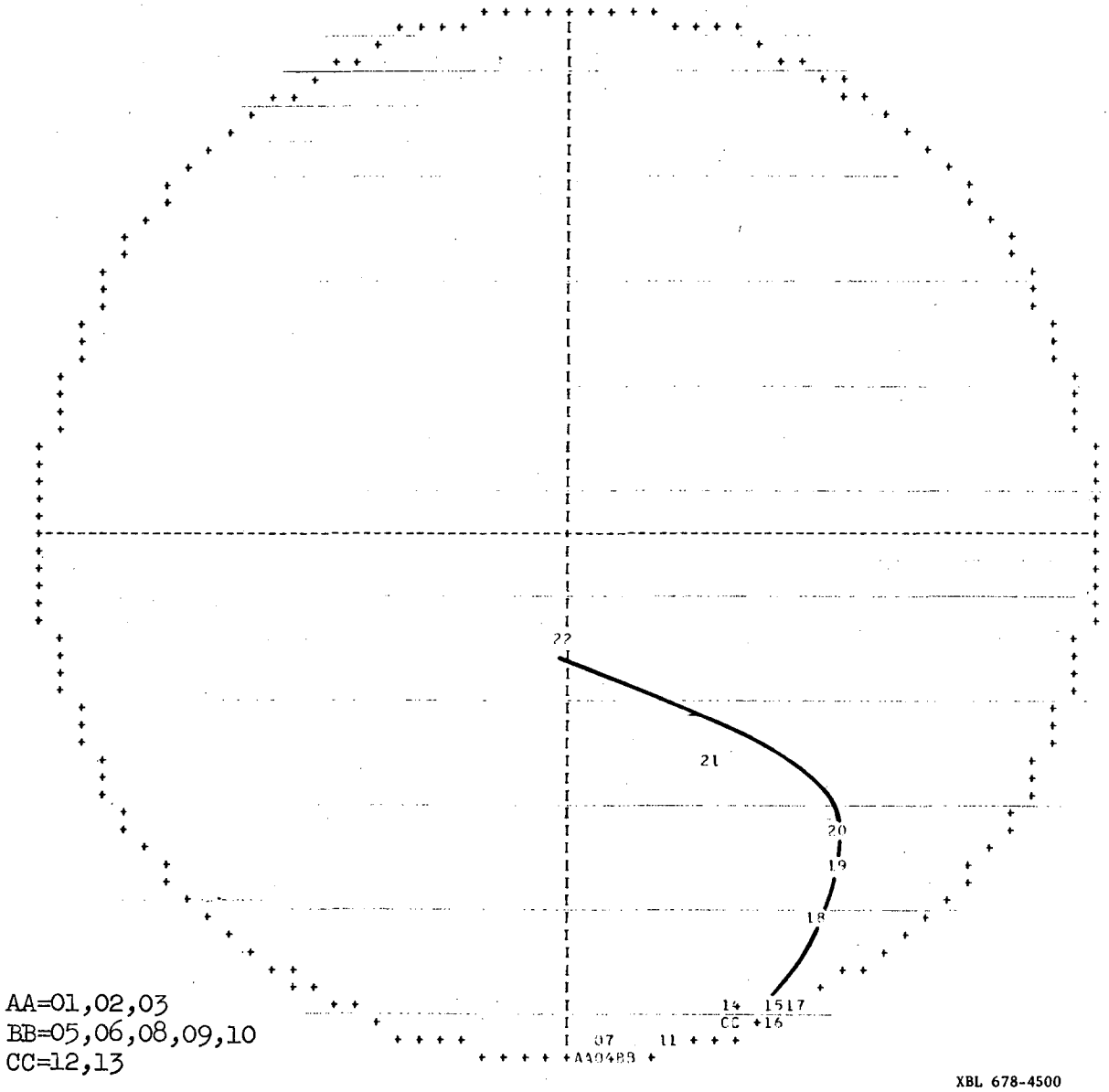

Fig. 37. Argand plot of the energy dependence of the F_{37} πN partial-wave amplitude. Table XXIV gives the energies corresponding to the points plotted; Table XXV, their numerical values and errors. The curve is drawn simply to guide the eye.

Table XXV. Numerical results of the phase-shift analysis.

PLAB= 613.9 TLAB= 490.0 PCM= 399.3 INVARMASS= 1442.6
CHI-SQUARE= 8.64798E+01 FOR 58 DEGREES OF FREEDOM 100 MEASUREMENTS

	I=3/2 PARAMETERS ETA			DELTA			I=1/2 PARAMETERS ETA			DELTA		
S31	1.0000	+/-	.0003	-28.2119	+/-	.4534	S11	.7377	+/-	.0217	28.5039	+/- .8432
P31	1.0000	+/-	.0006	-19.3656	+/-	.5441	P11	.2993	+/-	.0224	-87.9211	+/- 3.1978
P33	.9545	+/-	.0113	-21.8070	+/-	.2810	P13	.9231	+/-	.0264	-.0061	+/- .0005
D33	.9456	+/-	.0094	-1.5282	+/-	.1381	D13	.8864	+/-	.0207	18.0222	+/- .8614
D35	.9999	+/-	.0002	-.1623	+/-	.0150	D15	.9756	+/-	.0088	4.8362	+/- .3446
F35	1.0000	+/-	.0003	-.8723	+/-	.0978	F15	.9998	+/-	.0004	2.0685	+/- .5232
F37	1.0000	+/-	.0001	2.7210	+/-	.1420	F17	.9999	+/-	.0002	1.5567	+/- .3204
G37	1.0000	+/-	.0000	.6730	+/-	.1125	G17	1.0000	+/-	.0009	1.5789	+/- .2145
G39	.9677	+/-	.0089	-.2425	+/-	.0410	G19	.9997	+/-	.0041	.3879	+/- .0608
EPSILON(1)= .5934 +/- .0233												
EPSILON(2)= .5514 +/- .0199												
EPSILON(3)= .5928 +/- .0233												
EPSILON(4)= 1.0309 +/- .0372												
EPSILON(5)= 1.0151 +/- .0325												
EPSILON(6)= .9770 +/- .0461												

PLAB= 675.3 TLAB= 550.0 PCM= 427.8 INVARMASS= 1481.1
CHI-SQUARE= 8.59680E+01 FOR 49 DEGREES OF FREEDOM 89 MEASUREMENTS

	I=3/2 PARAMETERS ETA			DELTA			I=1/2 PARAMETERS ETA			DELTA		
S31	.9604	+/-	.0080	-27.6798	+/-	.4130	S11	.6549	+/-	.0175	31.1004	+/- .9758
P31	.9997	+/-	.0009	-17.2331	+/-	.3553	P11	.4301	+/-	.0127	-65.5627	+/- 1.9577
P33	1.0000	+/-	.0012	-19.0874	+/-	.2854	P13	.8304	+/-	.0133	-.0062	+/- .0001
D33	.9745	+/-	.0133	-2.3885	+/-	.0859	D13	.6850	+/-	.0174	31.4794	+/- .7773
D35	.9999	+/-	.0020	-.1792	+/-	.0041	D15	.9999	+/-	.0004	4.7761	+/- .1343
F35	.9991	+/-	.0046	-.7414	+/-	.0555	F15	.9120	+/-	.0087	3.6614	+/- .1771
F37	.9993	+/-	.0009	3.7352	+/-	.1182	F17	.9802	+/-	.0038	2.2002	+/- .0701
G37	1.0000	+/-	.0012	.2551	+/-	.0436	G17	.9997	+/-	.0005	2.9096	+/- .1466
G39	.9966	+/-	.0028	-.1677	+/-	.0145	G19	1.0000	+/-	.0002	.5053	+/- .0149
EPSILON(1)= 1.0459 +/- .0203												
EPSILON(2)= .8758 +/- .0180												
EPSILON(3)= 1.0010 +/- .0188												
EPSILON(4)= .9530 +/- .0169												

XBL 678-4610

(continued on next page)

Table XXV. Numerical results of the phase-shift analysis. (continued)

PLAB= 706.9 TLAB= 581.0 PCM= 442.0 INVARMASS= 1500.6
CHI-SQUARE= 6.48161E+01 FOR 41 DEGREES OF FREEDOM 82 MEASUREMENTS

	I=3/2 PARAMETERS ETA		I=3/2 PARAMETERS DELTA			I=1/2 PARAMETERS ETA		I=1/2 PARAMETERS DELTA	
S31	.8611	+/- .0314	-29.0205	+/- .6820	S11	.7004	+/- .0410	38.0284	+/- 1.9228
P31	.9956	+/- .0021	-22.1660	+/- 1.3013	P11	.5221	+/- .0619	-73.7904	+/- 3.5829
P33	.9151	+/- .0202	-13.2911	+/- .7889	P13	.7299	+/- .0514	-6.2270	+/- 1.9664
D33	.8860	+/- .0225	-2.8329	+/- .5404	D13	.2975	+/- .0907	38.1912	+/- 4.0895
D35	1.0000	+/- .0007	.5662	+/- .5419	D15	1.0000	+/- .0004	9.5896	+/- 1.7009
F35	1.0000	+/- .0046	-1.2753	+/- .3442	F15	1.0000	+/- .0003	3.9347	+/- .6278
F37	.9999	+/- .0003	3.2659	+/- .2968	F17	.9999	+/- .0004	.6611	+/- .1796
G37	1.0000	+/- .0000	-.4769	+/- .1333	G17	.9999	+/- .0002	2.1561	+/- .5825
G39	1.0000	+/- .0004	.1189	+/- .2340	G19	.9944	+/- .0125	-.8203	+/- .2365

EPSILON(1)= 1.0006 +/- .0305
EPSILON(2)= .9750 +/- .0288
EPSILON(3)= .9837 +/- .0271
EPSILON(4)= .9990 +/- .0588
EPSILON(5)= 1.0202 +/- .0558

PLAB= 726.3 TLAB= 600.0 PCM= 450.5 INVARMASS= 1512.5
CHI-SQUARE= 6.20897E+01 FOR 63 DEGREES OF FREEDOM 104 MEASUREMENTS

	I=3/2 PARAMETERS ETA		I=3/2 PARAMETERS DELTA			I=1/2 PARAMETERS ETA		I=1/2 PARAMETERS DELTA	
S31	.8510	+/- .0149	-27.4634	+/- .6373	S11	.4767	+/- .0153	39.2196	+/- 1.4719
P31	.9659	+/- .0128	-20.6271	+/- .6799	P11	.4470	+/- .0195	-69.8469	+/- 1.3009
P33	.9566	+/- .0054	-14.5474	+/- .3400	P13	.8060	+/- .0147	-8.3739	+/- .6002
D33	.8630	+/- .0101	-2.2066	+/- .3446	D13	.2016	+/- .0210	53.1089	+/- 1.8391
D35	1.0000	+/- .0011	.0468	+/- .2056	D15	.9970	+/- .0019	7.8033	+/- .3547
F35	.9822	+/- .0024	1.3928	+/- .0932	F15	.9972	+/- .0013	6.5144	+/- .2437
F37	.9832	+/- .0061	2.0001	+/- .0804	F17	.9992	+/- .0005	.3231	+/- .0106
G37	.9750	+/- .0040	-.3993	+/- .1454	G17	.9999	+/- .0009	1.2255	+/- .4004
G39	.9986	+/- .0007	-.0112	+/- .1366	G19	.9998	+/- .0001	.5019	+/- .2145

EPSILON(1)= .9938 +/- .0189
EPSILON(2)= .9777 +/- .0162
EPSILON(3)= 1.0164 +/- .0224
EPSILON(4)= .9865 +/- .0412
EPSILON(5)= .9986 +/- .0289

XBL 678-4607

(continued on next page)

Table XXV. Numerical results of the phase-shift analysis. (continued)

PLAB= 777.2 TLAB= 650.0 PCM= 472.5 INVARMASS= 1543.2
CHI-SQUARE= 6.82041E+01 FOR 63 DEGREES OF FREEDOM 104 MEASUREMENTS

	I=3/2 PARAMETERS ETA	DELTA		I=1/2 PARAMETERS ETA	DELTA
S31	.9052 +/- .0287	-26.0587 +/- .6344	S11	.2860 +/- .0373	24.1538 +/- 2.1756
P31	.9562 +/- .0173	-17.2506 +/- .6687	P11	.5137 +/- .0395	-48.1765 +/- 1.4141
P33	1.0000 +/- .0009	-10.8122 +/- .3144	P13	.8448 +/- .0250	-13.4732 +/- .7796
D33	.8796 +/- .0144	2.6580 +/- .5830	D13	.2179 +/- .0218	-45.6261 +/- 2.9331
D35	.9086 +/- .0058	-3.1422 +/- .3593	D15	.9048 +/- .0193	9.2125 +/- .4479
F35	.9366 +/- .0102	1.4690 +/- .2680	F15	.9998 +/- .0012	13.1945 +/- .6701
F37	.9992 +/- .0007	3.5104 +/- .2227	F17	.9830 +/- .0122	-.5962 +/- .1474
G37	.9996 +/- .0003	.4380 +/- .1497	G17	1.0000 +/- .0001	3.7093 +/- .3307
G39	.9999 +/- .0004	.4515 +/- .0947	G19	.9998 +/- .0001	-.3467 +/- .0835

EPSILON(1)= 1.0052 +/- .0260
EPSILON(2)= .9755 +/- .0216
EPSILON(3)= 1.0128 +/- .0358
EPSILON(4)= 1.0034 +/- .0393
EPSILON(5)= 1.0123 +/- .0389

PLAB= 825.9 TLAB= 698.0 PCM= 492.9 INVARMASS= 1572.1
CHI-SQUARE= 6.88669E+01 FOR 67 DEGREES OF FREEDOM 109 MEASUREMENTS

	I=3/2 PARAMETERS ETA	DELTA		I=1/2 PARAMETERS ETA	DELTA
S31	.7201 +/- .0434	-26.3092 +/- 1.0991	S11	.5160 +/- .0589	31.6017 +/- 3.6580
P31	.9755 +/- .0318	-21.5406 +/- 1.0767	P11	.5230 +/- .0738	-45.8181 +/- 2.5819
P33	.8967 +/- .0278	-7.1862 +/- .7808	P13	.9318 +/- .0480	-9.7232 +/- 1.8054
D33	.7590 +/- .0271	.8023 +/- .6915	D13	.4812 +/- .0384	-30.0699 +/- 1.9619
D35	.9611 +/- .0220	-3.0388 +/- .5136	D15	.8867 +/- .0345	14.6165 +/- .6378
F35	1.0000 +/- .0012	.0528 +/- .0121	F15	.9168 +/- .0414	13.9235 +/- .7294
F37	.9999 +/- .0006	3.7636 +/- .3769	F17	1.0000 +/- .0014	1.5481 +/- .8516
G37	.9871 +/- .0162	-.8211 +/- .2840	G17	.9998 +/- .0019	2.1994 +/- .6811
G39	1.0000 +/- .0005	.3776 +/- .1444	G19	.9998 +/- .0025	.1862 +/- .1910

EPSILON(1)= .9965 +/- .0316
EPSILON(2)= .9975 +/- .0310
EPSILON(3)= .9913 +/- .0350
EPSILON(4)= .9981 +/- .0649
EPSILON(5)= .9735 +/- .0601
EPSILON(6)= 1.0184 +/- .0572

XBL 678-4611

(continued on next page)

Table XXV. Numerical results of the phase-shift analysis. (continued)

PLAB= 974.5 TLAB= 746.0 PCM= 512.7 INVARMASS= 1600.5
CHI-SQUARE= 9.51367E+01 FOR 77 DEGREES OF FREEDOM 119 MEASUREMENTS

	I=3/2 PARAMETERS ETA	DELTA	I=1/2 PARAMETERS ETA	DELTA
S31	.6729 +/- .0162	-24.3342 +/- .5893	S11 .5626 +/- .0169	31.8410 +/- .9447
P31	.7225 +/- .0177	-28.8561 +/- .6012	P11 .0910 +/- .0047	-42.1788 +/- 1.8676
P33	.9203 +/- .0109	-7.3155 +/- .2657	P13 .8069 +/- .0165	-3.4932 +/- .1751
D33	.9999 +/- .0003	-.3746 +/- .0082	D13 .7734 +/- .0157	-28.3023 +/- .4459
D35	.9079 +/- .0086	.2777 +/- .2234	D15 .7677 +/- .0092	12.7387 +/- .3717
F35	.7827 +/- .0087	1.0944 +/- .1177	F15 .9319 +/- .0137	20.8366 +/- .4088
F37	.9966 +/- .0009	3.0724 +/- .2364	F17 1.0000 +/- .0001	.1803 +/- .0040
G37	.9989 +/- .0029	1.0245 +/- .0260	G17 .9992 +/- .0028	.8473 +/- .0210
G39	.9990 +/- .0009	.3778 +/- .0116	G19 .9855 +/- .0068	.1336 +/- .0027

EPSILON(1)= .9897 +/- .0233
EPSILON(2)= .9728 +/- .0154
EPSILON(3)= 1.0482 +/- .0211
EPSILON(4)= 1.0252 +/- .0272
EPSILON(5)= .9605 +/- .0257
EPSILON(6)= .9981 +/- .0312

PLAB= 925.1 TLAB= 735.0 PCM= 532.7 INVARMASS= 1629.5
CHI-SQUARE= 4.86547E+01 FOR 51 DEGREES OF FREEDOM 92 MEASUREMENTS

	I=3/2 PARAMETERS ETA	DELTA	I=1/2 PARAMETERS ETA	DELTA
S31	.7357 +/- .0237	-36.9205 +/- 1.0074	S11 .7943 +/- .0438	41.8958 +/- 1.2992
P31	.6827 +/- .0251	-28.2930 +/- 1.0074	P11 .0962 +/- .0149	-69.3417 +/- 3.5417
P33	.8740 +/- .0134	-4.2688 +/- .5124	P13 .8274 +/- .0146	-2.0457 +/- .7873
D33	.9941 +/- .0217	-.3837 +/- .0966	D13 .8105 +/- .0361	-22.4836 +/- .9648
D35	.8550 +/- .0111	-3.6069 +/- .4210	D15 .6680 +/- .0214	17.1522 +/- .5507
F35	.7281 +/- .0152	2.2677 +/- .1858	F15 .7518 +/- .0453	32.8141 +/- 1.4645
F37	.9928 +/- .0016	5.6074 +/- .2930	F17 .9999 +/- .0017	.1684 +/- .2879
G37	.9999 +/- .0016	.8013 +/- .0436	G17 .9992 +/- .0007	.8734 +/- .5162
G39	.9969 +/- .0010	.4710 +/- .0256	G19 1.0000 +/- .0013	.1312 +/- .2168

EPSILON(1)= .9832 +/- .0253
EPSILON(2)= .9668 +/- .0190
EPSILON(3)= 1.0979 +/- .0298
EPSILON(4)= .9933 +/- .0545
EPSILON(5)= 1.0074 +/- .0535

XBL 678-4616

(continued on next page)

Table XXV. Numerical results of the phase-shift analysis. (continued)

PLAB= 975.0 TLAB= 845.4 PCM= 551.8 INVARMASS= 1657.7
CHI-SQUARE= 5.73320E+01 FOR 54 DEGREES OF FREEDOM 95 MEASUREMENTS

	I=3/2 PARAMETERS ETA		I=3/2 PARAMETERS DELTA		I=1/2 PARAMETERS ETA		I=1/2 PARAMETERS DELTA	
S31	.5927	+/- .0377	-45.2059	+/- 1.7092	S11	.6639 +/- .0369	62.6738	+/- 1.6164
P31	.9666	+/- .0244	-23.3058	+/- .9044	P11	.0943 +/- .0194	-77.7502	+/- 7.2083
P33	.6555	+/- .0208	-5.4478	+/- .6389	P13	.8988 +/- .0188	-.4834	+/- .0588
D33	.8464	+/- .0218	-.1063	+/- .0178	D13	.7882 +/- .0210	-12.8570	+/- .7529
D35	.9323	+/- .0153	-4.7733	+/- .4482	D15	.3216 +/- .0184	15.1422	+/- 1.3985
F35	.8588	+/- .0280	.5615	+/- .0797	F15	.4243 +/- .0215	59.2034	+/- 1.9240
F37	1.0000	+/- .0002	9.5219	+/- .2988	F17	.9999 +/- .0001	.0917	+/- .0106
G37	1.0000	+/- .0001	.5680	+/- .0860	G17	1.0000 +/- .0001	4.2442	+/- .3840
G39	.9618	+/- .0100	-.0383	+/- .0056	G19	.9644 +/- .0081	-.6513	+/- .1324
EPSILON(1)=	.9873	+/- .0221						
EPSILON(2)=	.9196	+/- .0166						
EPSILON(3)=	1.1614	+/- .0337						
EPSILON(4)=	1.0317	+/- .0501						
EPSILON(5)=	.9783	+/- .0484						

PLAB= 999.9 TLAB= 870.0 PCM= 561.2 INVARMASS= 1671.6
CHI-SQUARE= 5.66634E+01 FOR 50 DEGREES OF FREEDOM 91 MEASUREMENTS

	I=3/2 PARAMETERS ETA		I=3/2 PARAMETERS DELTA		I=1/2 PARAMETERS ETA		I=1/2 PARAMETERS DELTA	
S31	.7040	+/- .0411	-46.3235	+/- 1.7039	S11	.6302 +/- .0487	84.7830	+/- 2.1067
P31	.9774	+/- .0290	-19.0389	+/- 1.2710	P11	.1386 +/- .0396	-28.4064	+/- 7.2969
P33	.6106	+/- .0196	-6.1954	+/- 1.0654	P13	.9997 +/- .0063	-.3777	+/- .9223
D33	.8605	+/- .0301	-.6590	+/- .6003	D13	.7679 +/- .0268	-18.5050	+/- 1.1836
D35	.9229	+/- .0142	-6.3051	+/- .5514	D15	.1638 +/- .0191	-2.9817	+/- .6733
F35	.8241	+/- .0287	.4949	+/- .3243	F15	.3905 +/- .0332	63.2876	+/- 2.7312
F37	.9942	+/- .0044	9.2234	+/- .3538	F17	.9996 +/- .0009	.0550	+/- .5882
G37	.9951	+/- .0054	-.4128	+/- .1486	G17	.9210 +/- .0192	3.4384	+/- .5986
G39	.9802	+/- .0096	.6313	+/- .1518	G19	.9878 +/- .0120	1.9145	+/- .4184
EPSILON(1)=	.9518	+/- .0235						
EPSILON(2)=	.9681	+/- .0259						
EPSILON(3)=	1.0750	+/- .0284						
EPSILON(4)=	1.0870	+/- .0505						
EPSILON(5)=	1.0057	+/- .0485						

XBL 678-4612

(continued on next page)

Table XXV. Numerical results of the phase-shift analysis. (continued)

PLAB= 1030.2 TLAB= 900.0 PCM= 572.5 INVARMASS= 1688.3
CHI-SQUARE= 5.31626E+01 FOR 54 DEGREES OF FREEDOM 95 MEASUREMENTS

	I=3/2 PARAMETERS ETA	DELTA	I=1/2 PARAMETERS ETA	DELTA
S31	.5025 +/- .0196	-38.3587 +/- 1.0417	S11 .6641 +/- .0176	-88.9240 +/- 1.0699
P31	.9054 +/- .0152	-31.7662 +/- .6904	P11 .1881 +/- .0086	-17.4039 +/- 2.4147
P33	.5761 +/- .0112	-8.1454 +/- .8237	P13 .8740 +/- .0134	-.6435 +/- .0247
D33	.9257 +/- .0112	-1.4264 +/- .0847	D13 .6991 +/- .0184	-13.0824 +/- .6454
D35	1.0000 +/- .0006	-3.6897 +/- .4060	D15 .2509 +/- .0108	-10.4550 +/- .8335
F35	.8034 +/- .0121	.7182 +/- .0461	F15 .3764 +/- .0151	-82.2899 +/- 1.3668
F37	.9625 +/- .0077	9.8858 +/- .2332	F17 .9938 +/- .0053	.0524 +/- .0027
G37	1.0000 +/- .0001	.5245 +/- .0988	G17 .9983 +/- .0011	4.6164 +/- .2372
G39	.9772 +/- .0056	-.2969 +/- .0809	G19 .9704 +/- .0051	-.4701 +/- .2237

EPSILON(1)= .9307 +/- .0177
EPSILON(2)= .9746 +/- .0124
EPSILON(3)= 1.1556 +/- .0200
EPSILON(4)= 1.0146 +/- .0525
EPSILON(5)= 1.0076 +/- .0407

PLAB= 1080.0 TLAB= 949.4 PCM= 590.6 INVARMASS= 1715.6
CHI-SQUARE= 6.29850E+01 FOR 53 DEGREES OF FREEDOM 94 MEASUREMENTS

	I=3/2 PARAMETERS ETA	DELTA	I=1/2 PARAMETERS ETA	DELTA
S31	.5489 +/- .0146	-42.5859 +/- .6869	S11 .4433 +/- .0207	-79.1302 +/- 1.7713
P31	.9013 +/- .0142	-30.3500 +/- .7670	P11 .2960 +/- .0229	-19.2277 +/- 1.1735
P33	.6023 +/- .0112	-4.9210 +/- .2065	P13 .7505 +/- .0099	-2.4545 +/- .1445
D33	.8792 +/- .0115	-4.1815 +/- .2330	D13 .7294 +/- .0145	-12.0307 +/- .7587
D35	.9990 +/- .0018	-4.2999 +/- .1257	D15 .3766 +/- .0110	-7.1599 +/- .3565
F35	.7763 +/- .0114	.0060 +/- .0002	F15 .4002 +/- .0148	-50.9147 +/- .8208
F37	.9981 +/- .0023	12.2924 +/- .2028	F17 .9997 +/- .0005	-2.3939 +/- .1235
G37	.9997 +/- .0021	.1809 +/- .0053	G17 .9930 +/- .0130	3.0539 +/- .1246
G39	.9744 +/- .0052	-.3785 +/- .0235	G19 .9878 +/- .0055	-.1115 +/- .0068

EPSILON(1)= .9365 +/- .0164
EPSILON(2)= .9609 +/- .0149
EPSILON(3)= 1.1869 +/- .0236
EPSILON(4)= .9999 +/- .0353
EPSILON(5)= .9987 +/- .0374

XBL 678-4613

(continued on next page)

Table XXV. Numerical results of the phase-shift analysis. (continued)

PLAB= 1120.9 TLAB= 990.0 PCM= 605.2 INVARMASS= 1737.6
CHI-SQUARE= 5.25891E+01 FOR 54 DEGREES OF FREEDOM 95 MEASUREMENTS

	I=3/2 PARAMETERS ETA	DELTA		I=1/2 PARAMETERS ETA	DELTA
S31	.7510 +/- .0337	-60.2977 +/- 1.5732	S11	.6504 +/- .0399	-67.4764 +/- 2.1263
P31	.8482 +/- .0342	-22.1437 +/- .8890	P11	.0000 +/- .0000	-1.0049 +/- .0999
P33	.8344 +/- .0186	-5.8314 +/- 1.0946	P13	.6200 +/- .0228	-1.7815 +/- 1.4733
D33	.7575 +/- .0215	-11.2312 +/- .8184	D13	.9134 +/- .0376	-9.0467 +/- 1.4924
D35	.7364 +/- .0204	-1.2999 +/- .8524	D15	.5732 +/- .0324	-16.8757 +/- .8184
F35	.8660 +/- .0205	3.4110 +/- .5078	F15	.5345 +/- .0325	-36.2713 +/- .8820
F37	1.0000 +/- .0002	11.3683 +/- .4644	F17	1.0000 +/- .0003	2.1866 +/- .5400
G37	.9998 +/- .0002	-2.1659 +/- .3189	G17	.9027 +/- .0174	.7588 +/- .1216
G35	.9804 +/- .0117	1.1699 +/- .1810	G19	1.0000 +/- .0004	.0522 +/- .0111
EPSILON(1)= .9722 +/- .0253					
EPSILON(2)= .9666 +/- .0273					
EPSILON(3)= 1.0159 +/- .0356					
EPSILON(4)= .9970 +/- .0663					
EPSILON(5)= .9681 +/- .0378					

PLAB= 1190.0 TLAB= 1043.6 PCM= 625.8 INVARMASS= 1762.0
CHI-SQUARE= 7.69162E+01 FOR 54 DEGREES OF FREEDOM 105 MEASUREMENTS

	I=3/2 PARAMETERS ETA	DELTA		I=1/2 PARAMETERS ETA	DELTA
S31	.6525 +/- .0259	-64.0783 +/- 1.1171	S11	.4339 +/- .0244	-68.2813 +/- 1.6239
P31	.9926 +/- .0262	-22.9293 +/- .6742	P11	.0397 +/- .0090	-1.1789 +/- 1.0179
P33	.9099 +/- .0207	-4.5768 +/- .7625	P13	.6451 +/- .0120	-5.2165 +/- 1.2009
D33	.7741 +/- .0115	-12.3685 +/- .6397	D13	.9934 +/- .0219	-5.9998 +/- .6799
D35	.7773 +/- .0186	-2.0234 +/- .5756	D15	.6191 +/- .0219	-17.7351 +/- .7331
F35	.8432 +/- .0124	3.3227 +/- .2541	F15	.5025 +/- .0176	-33.5449 +/- .7074
F37	.9991 +/- .0006	13.3383 +/- .3739	F17	1.0000 +/- .0006	.4164 +/- .2153
G37	.9093 +/- .0113	-.3278 +/- .1549	G17	.3362 +/- .0111	4.5331 +/- .4259
G39	.9469 +/- .0093	1.2651 +/- .1703	G19	.9998 +/- .0001	.5699 +/- .1361
EPSILON(1)= .9844 +/- .0220					
EPSILON(2)= 1.0043 +/- .0102					
EPSILON(3)= 1.0421 +/- .0299					
EPSILON(4)= .9860 +/- .0402					
EPSILON(5)= .9346 +/- .0280					

XBL 678-4609

(continued on the next page)

Table XXV. Numerical results of the phase-shift analysis. (continued)

PLAB= 1280.0 TLAB= 1140.5 PCM= 652.5 INVARMASS= 1870.2
CHI-SQUARE= 7.456705E+01 FOR 69 DEGREES OF FREEDOM 104 MEASUREMENTS

	I=3/2 PARAMETERS ETA	DELTA	I=1/2 PARAMETERS ETA	DELTA
S31	.7123 +/- .0462	-80.3547 +/- 2.0451	S11	.5231 +/- .0455	-71.9930 +/- 2.7423
P31	1.0000 +/- .0026	-10.4765 +/- 1.3522	P11	.0007 +/- .0001	-3.7354 +/- .3816
P33	.7910 +/- .0246	-5.1316 +/- .8254	P13	.6243 +/- .0338	-6.4167 +/- 1.2315
D33	.7173 +/- .0203	-12.1280 +/- 1.0341	D13	.8170 +/- .0317	-9.4405 +/- 1.2352
D35	.7061 +/- .0210	-5.5884 +/- .9314	D15	.7939 +/- .0317	-16.0736 +/- .8731
F35	.7623 +/- .0152	2.4203 +/- .3760	F15	.6783 +/- .0224	-14.7935 +/- 1.1196
F37	.8743 +/- .0292	17.1367 +/- .5679	G17	.8394 +/- .0256	-.4429 +/- .5246
G37	1.0000 +/- .0023	-1.5261 +/- .3128	G17	.6056 +/- .0120	6.4795 +/- .5525
G39	.8524 +/- .0137	2.6114 +/- .4341	G19	.9984 +/- .0121	.2135 +/- .0494

EPSILON(1)= .7815 +/- .0534
EPSILON(2)= 1.0019 +/- .0341
EPSILON(3)= 1.0595 +/- .0383
EPSILON(4)= .9509 +/- .0359
EPSILON(5)= .9022 +/- .0452

PLAB= 1359.4 TLAB= 1227.0 PCM= 685.3 INVARMASS= 1861.2
CHI-SQUARE= 7.931165E+01 FOR 69 DEGREES OF FREEDOM 110 MEASUREMENTS

	I=3/2 PARAMETERS ETA	DELTA	I=1/2 PARAMETERS ETA	DELTA
S31	.7779 +/- .0476	-83.4234 +/- 2.2866	S11	.4755 +/- .0531	-81.6435 +/- 3.1962
P31	.9987 +/- .0026	-15.4490 +/- 1.0485	P11	.4976 +/- .0339	-.0396 +/- .0045
P33	.9091 +/- .0284	-9.3165 +/- 1.4847	P13	.5360 +/- .0252	-16.8617 +/- 2.1359
D33	.6866 +/- .0237	-10.7509 +/- 1.3491	D13	.8209 +/- .0289	-12.0346 +/- .8280
D35	.5573 +/- .0293	-8.9477 +/- 1.4076	D15	.5839 +/- .0290	-12.7149 +/- .9882
F35	.8515 +/- .0211	2.7442 +/- .4292	F15	.4946 +/- .0208	-7.3591 +/- 1.7205
F37	.8115 +/- .0231	19.3749 +/- .7627	F17	1.0000 +/- .0012	-2.0715 +/- .3173
G37	.9519 +/- .0171	-4.0741 +/- .4578	G17	.9735 +/- .0154	3.5037 +/- .5820
G39	.7801 +/- .0192	4.5484 +/- .4889	G19	1.0000 +/- .0001	-.1072 +/- .0116

EPSILON(1)= .9362 +/- .0253
EPSILON(2)= 1.0119 +/- .0292
EPSILON(3)= 1.0689 +/- .0334
EPSILON(4)= 1.0210 +/- .0305
EPSILON(5)= .8963 +/- .0343

XBL 678-4608

(continued on next page)

Table XXV. Numerical results of the phase-shift analysis. (continued)

PLAB= 1443.9 TLAB= 1311.0 PCM= 711.8 INVARMASS= 1903.1
CHI-SQUARE= 9.60396E+01 FOR 71 DEGREES OF FREEDOM 112 MEASUREMENTS

	I=3/2 PARAMETERS ETA	DELTA		I=1/2 PARAMETERS ETA	DELTA
S31	.4454 +/- .0329	84.5564 +/- 2.1108	S11	.0720 +/- .0321	-53.1159 +/-10.3055
P31	.6369 +/- .0403	-16.8146 +/- 1.2229	P11	.5639 +/- .0299	15.9338 +/- 1.5821
P33	1.0000 +/- .0005	-18.6350 +/- .8150	P13	.6515 +/- .0248	-25.5360 +/- 1.0652
D33	.8044 +/- .0233	-16.0302 +/- .8270	D13	.7810 +/- .0219	-10.9716 +/- 1.2856
D35	.2761 +/- .0234	-19.9982 +/- 1.8750	D15	.5129 +/- .0202	-10.2415 +/- 1.0165
F35	.8218 +/- .0187	2.8749 +/- .4101	F15	.4970 +/- .0185	-2.7943 +/- 1.1141
F37	.7553 +/- .0206	21.7226 +/- .6515	F17	1.0000 +/- .0001	1.1092 +/- .1781
G37	1.0000 +/- .0001	-1.6586 +/- .2250	G17	.9270 +/- .0146	.9487 +/- .5987
G39	.7004 +/- .0178	-2.6658 +/- .5636	G19	1.0000 +/- .0001	1.7724 +/- .3794
EPSILON(1)= .9783 +/- .0237					
EPSILON(2)= .9970 +/- .0266					
EPSILON(3)= 1.0090 +/- .0375					
EPSILON(4)= .9203 +/- .0271					
EPSILON(5)= 1.0132 +/- .0593					

PLAB= 1579.4 TLAB= 1446.0 PCM= 752.8 INVARMASS= 1968.5
CHI-SQUARE= 9.00349E+01 FOR 68 DEGREES OF FREEDOM 109 MEASUREMENTS

	I=3/2 PARAMETERS ETA	DELTA		I=1/2 PARAMETERS ETA	DELTA
S31	.3836 +/- .0195	-36.5979 +/- 1.1633	S11	.0032 +/- .0175	-17.9027 +/- .9151
P31	.1253 +/- .0229	7.5011 +/- .1898	P11	.7731 +/- .0241	19.3844 +/- .6786
P33	.9998 +/- .0010	-13.4984 +/- .4393	P13	.5237 +/- .0157	-20.9749 +/- 1.2182
D33	.9349 +/- .0135	-16.7412 +/- .3733	D13	.9918 +/- .0027	1.5909 +/- .0735
D35	.1399 +/- .0125	-43.4455 +/- 1.0972	D15	.3435 +/- .0153	14.0746 +/- 1.1682
F35	.7451 +/- .0105	-4.3145 +/- .2474	F15	.9991 +/- .0034	.4476 +/- .3212
F37	.4948 +/- .0116	16.1650 +/- .5018	F17	.6282 +/- .0162	3.7722 +/- .2620
G37	.9152 +/- .0079	-1.9820 +/- .2349	G17	.9974 +/- .0032	-1.0601 +/- .0837
G39	1.0000 +/- .0006	-6.3745 +/- .2130	G19	.7488 +/- .0094	-5.1470 +/- .3673

EPSILON(1)= .9345 +/- .0106
EPSILON(2)= 1.0348 +/- .0208
EPSILON(3)= .9890 +/- .0253
EPSILON(4)= 1.0669 +/- .0289
EPSILON(5)= 1.0483 +/- .0244

XBL 678-4615

(continued on next page)

Table XXV. Numerical results of the phase-shift analysis. (continued)

PLAB= 1699.9 TLAB= 1566.0 PCM= 787.6 INVARMASS= 2024.9
CHI-SQUARE= 9.24600E+01 FOR 83 DEGREES OF FREEDOM 124 MEASUREMENTS

	I=3/2 PARAMETERS ETA		I=3/2 PARAMETERS DELTA		I=1/2 PARAMETERS ETA		I=1/2 PARAMETERS DELTA	
S31	.4750 +/-	.0174	-20.2806 +/-	1.4152	S11	.3210 +/- .0214	-6.8049 +/-	2.7924
P31	.3792 +/-	.0082	.1656 +/-	1.4234	P11	.6883 +/- .0190	10.3207 +/-	1.1718
P33	.8453 +/-	.0130	-21.9612 +/-	.4998	P13	.4397 +/- .0161	-20.6391 +/-	1.3115
D33	.9913 +/-	.0047	-6.9426 +/-	.4793	D13	.8347 +/- .0151	2.2432 +/-	.6191
D35	.3315 +/-	.0131	-21.7788 +/-	1.0455	D15	.5008 +/- .0181	25.6825 +/-	.7869
F35	.7E05 +/-	.0081	-1.9955 +/-	.3934	F15	.8700 +/- .0121	5.4588 +/-	.2478
F37	.2C23 +/-	.0059	1.4205 +/-	1.7698	F17	.4275 +/- .0124	8.3996 +/-	.2323
G37	.9987 +/-	.0003	-3.1181 +/-	.1892	G17	.9965 +/- .0020	-.0185 +/-	.0006
G39	.9933 +/-	.0016	-.2475 +/-	.0135	G19	.8965 +/- .0120	-10.1663 +/-	.3682

EPSILON(1)= 1.0687 +/- .0112
EPSILON(2)= .9897 +/- .0087
EPSILON(3)= 1.0695 +/- .0242
EPSILON(4)= 1.0309 +/- .0205
EPSILON(5)= .9729 +/- .0268

XBL 678-4614

C. Legendre Fits

The results of fitting the data of this experiment to an expansion similar to that in (V-8) are shown in Fig. 38. The actual expansion used was

$$I_o P = \Sigma C_i P_i^1(\cos\theta) ,$$

so the C_i are not dimensionless as were the B_i in Section V-A-2. The π^+p differential cross section data (I_o) used was that of Duke et al (Reference 13). The behavior of these coefficients, when related to the partial-wave amplitudes by the formulae given in Reference 1, supports the F_{37} assignment[49] to the 1920 MeV π^+p resonance.

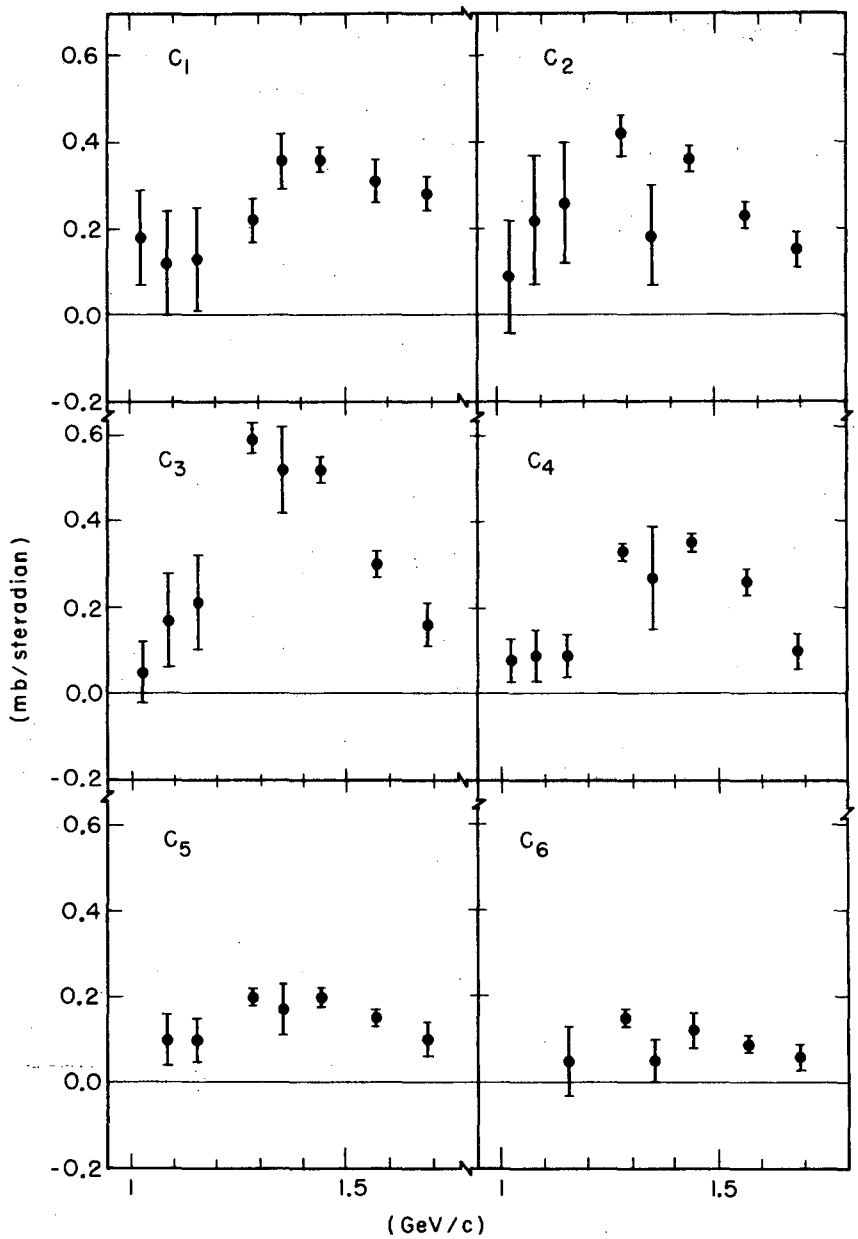

Fig. 38. Coefficients in the associated Legendre expansion $I_o P = \Sigma C_i P_i^1(\cos\theta_{c.m.})$ versus lab momentum of the pion for $\pi^+ p$ scattering.

ACKNOWLEDGMENTS

It has been a pleasure and an inspiration to work with and learn from Professors Gilbert Shapiro, Owen Chamberlain, and Herbert Steiner. I am indebted to Professor Shapiro, in particular, for his influence in introducing me to the field of high energy physics.

Dr. Leland E. Holloway has been a personal friend and a great help in assembling the electronics for this experiment. Drs. Paul D. Grannis and Luc Valentin contributed in many ways, but especially to the programming involved in the analysis of the data.

My co-worker, Dr. Michel J. Hansroul, has earned my sincere gratitude for his close collaboration and friendship throughout this work.

Dr. John F. Arens, Dr. John E. Brolley, Dr. Byron D. Dieterle, Dr. David M. Weldon, Raymond Fuzesy, William Gorn, Charles Morehouse, Michael Paciotti, Peter Robrish and Stephen Rock all contributed generously during the setup and data-taking phases of this experiment. Messrs. Robrish and Morehouse, in particular, deserve credit for their work on the beam design and target polarization measurements, respectively.

The assistance of the Bevatron staff and the personnel of the LRL computer center is gratefully acknowledged.

The final preparation of this thesis would have been impossible without the generous and able secretarial assistance of Mrs. Rosemary Fowell.

Most of all I am indebted to my wife, Katherine, for her patience, perseverance, and encouragement during these last few years. This is her thesis, too.

APPENDIX

Throughout this appendix we will suppress the subscript k which varies with θ_{up} bin number. The formulae apply to each θ_{up} bin independently.

In Section III-C, we obtained the least squares fit conditions:

$$\frac{\partial J}{\partial I_o} = \frac{\partial J}{\partial I_1} = 0 \tag{A-1}$$

where

$$J = \sum_i M_i \left[H_i - (I_o + I_1 p_i) \right]^2 ,$$

$$H_i = \frac{N_i - B_i}{M_i} , \tag{A-2}$$

$$I_1 = I_o P ,$$

and

$$B_i = bM_i .$$

From (A-1), one gets

$$\sum_i (N_i - B_i) - I_o \sum_i M_i - I_o P \sum_i M_i p_i = 0$$

and

$$\sum_i (N_i - B_i) p_i - I_o \sum_i M_i p_i - I_o P \sum_i M_i p_i^2 = 0 .$$

Eliminating I_o and solving for P, this yields

$$P = \frac{\sum_i (N_i - B_i) p_i - \langle p \rangle \sum_i (N_i - B_i)}{\langle p^2 \rangle \sum_i M_i H_i - \langle p \rangle \sum_i H_i M_i p_i} \tag{A-3}$$

where

$$< p > = \frac{\sum_i M_i p_i}{\sum_i M_i} \qquad \text{(A-4)}$$

and

$$< p^2 > = \frac{\sum_i M_i p_i^2}{\sum_i M_i} \quad . \qquad \text{(A-5)}$$

If a new variable, q_i , is defined by

$$q_i = p_i - < p > ,$$

then

$$< q^2 > = < p^2 > - < p >^2$$

and (A-3) becomes

$$P = \frac{\sum_i (N_i - B_i)\, q_i}{< q^2 > \sum_i (N_i - B_i) - < p > \sum_i (N_i - B_i)\, q_i} \quad .$$

This can be written more consisely as

$$P = \frac{\epsilon}{1 - \epsilon < p >} , \qquad \text{(A-6)}$$

where

$$\epsilon = \frac{\sum_i (N_i - B_i)\, q_i}{< q^2 > \sum_i (N_i - B_i)} \quad . \qquad \text{(A-7)}$$

The error in P is obtained from (A-6):

$$(\Delta P)^2 = \left[\frac{\partial P}{\partial \epsilon}\,\Delta\epsilon\right]^2 + \left[\frac{\partial P}{\partial \langle p \rangle}\,\Delta \langle p \rangle\right]^2 .$$

The second term of this expression can be verified to be very small, and its contribution can be neglected in the calculation of ΔP. Thus

$$\Delta P = \frac{1}{(1 - \epsilon \langle p \rangle)^2}\,\Delta\epsilon , \tag{A-8}$$

$$\Delta\epsilon = \left[\sum_i \left[\frac{\partial \epsilon}{\partial N_i}\,\Delta N_i\right]^2 + \sum_i \left[\frac{\partial \epsilon}{\partial M_i}\,\Delta M_i\right]^2 + \left[\frac{\partial \epsilon}{\partial b}\,\Delta b\right]^2 + \sum \left[\frac{\partial \epsilon}{\partial p_i}\,\Delta p_i\right]^2\right]^{1/2} . \tag{A-9}$$

The first three terms in (A-9) express the contribution to the error which results from the statistical uncertainty of the counting rates.

ΔN_i is the uncertainty in the number of coplanar counts in the elastic peak for run i : $\Delta N_i = \sqrt{N_i}$.

ΔM_i is the uncertainty in the number of monitor counts used to normalize run i : $\Delta M_i = \sqrt{M_i}$.

Δb is the uncertainty in the number of background counts per unit monitor and for a given θ_{up} bin is the same for all runs in a single block of data. From (III-1):

$$\Delta b = \left[b\,\frac{\Sigma D_j + \Sigma M_j}{(\Sigma M_j)^2}\right]^{1/2} .$$

Here, as in Section III-C-1, D_j is the number of counts in the elastic peak region of dummy-target (or simulated dummy-target) run j, and M_j is the number of monitor counts

for that run.

The last term in (A-9) gives the contribution to the error which results from the uncertainty in the target polarization during run i. This error is not simply statistical, and so has been included in the systematic error discussed in Section III-C-3.

REFERENCES

1. R. D. Tripp, Baryon Resonances, CERN Report 65-7 (Rev.), and International School of Physics, Enrico Fermi, XXXIII Course, Strong Interactions (Academic Press, N. Y., 1966).
We use the notation of this article and in general refer the reader to it for further details and references about the formalism of πN scattering.

2. P. Bareyre, C. Bricman, M. J. Longo, G. Valladas, G. Villet, G. Bizard, J. Duchon, J. M. Fonataine, J. P. Tatry, J. Seguinot, and J. Yonnet, Phys. Rev. Letters 14, 878 (1965).

3. T. J. Devlin, J. Solomon, and G. Bertsch, Phys. Rev. Letters 14, 1031 (1965).

4. J. C. Brisson, J. F. Detoeuf, P. Falk-Vairant, L. van Rossum, and G. Valladas, Nuovo Cimento 19, 210 (1961).

5. T. J. Devlin, B. J. Moyer, and V. Perez-Mendez, Phys. Rev. 125, 690 (1962).

6. A. N. Diddens, E. W. Jenkins, T. F. Kycia, and K. F. Riley, Phys. Rev. Letters 10, 262 (1963).

7. A. Stirling, Thesis, Saclay report No. CEA-R2838 (1966).

8. N. P. Klepikov, V. A. Mescheryakov, and S. N. Sokolov, Analysis of Experimental Data on the Total Cross Sections for Pion-Proton Interaction, (Joint Inst. for Nuclear Research, Dubna, USSR, 1960). A compilation of total cross-section data; the references are cited in the article.

9. P. Bareyre, C. Bricman, G. Valladas, G. Villet, G. Bizard, and J. Seguinot, Phys. Letters 8, 137 (1964).

10. A. Citron, W. Galbraith, T. F. Kycia, B. A. Leontic, R. H. Phillips, and A. Rousset, Phys. Rev. Letters 13, 205 (1964).

11. J. A. Helland, T. J. Devlin, D. E. Hagge, M. J. Longo, B. J. Moyer, and C. D. Wood, Phys. Rev. 134, B1062 (1964).
J. A. Helland, C. D. Wood, T. J. Devlin, D. E. Hagge, M. J. Longo, B. J. Moyer, and V. Perez-Mendez, Phys. Rev. 134, B1079 (1964).

12. P. M. Ogden, D. E. Hagge, J. A. Helland, M. Banner, J-F Detoeuf, and J. Teiger, Phys. Rev. 137, B1115 (1965).

13. P. J. Duke, D. P. Jones, M. A. R. Kemp, P. G. Murphy, J, D. Prentice, and J. J. Thresher, Phys. Rev. 149, 1077 (1966).

14. F. Bulos, R. E. Lanou, A. E. Pifer, A. M. Shapiro, M. W. Idgoff, R. Pavini, A. E. Brenner, C. A. Bordner, M. E. Law, E. E. Ronst, K. Strauch, J. Szymanski, P. Bastien, B. B. Brabson, Y. Eisenberg, B. T. Feld, V. K. Fischer, I. A. Pless, L. Rosenson, R. K. Yamamoto, G. Calvelli, L. Guerriero, G. A. Saladin, A. Tomasin, L. Ventura, G. Voci, F. Waldner, Phys. Rev. Letters 13, 558 (1964); L. Guerriero, Proc. Roy. Soc. (London) A289, 471 (1966).

15. Charles Chiu, Pion-Proton Charge-Exchange Scattering 500-1300 MeV (Ph. D. thesis), UCRL-16209, (1965).

16. C. B. Chiu, R. D. Eandi, A. C. Helmholz, R. W. Kenney, B. J. Moyer, J. A. Poirier, W. B. Richards, R. J. Cence, V. J. Peterson, N. K. Sehgal, and V. J. Stenger, Phys. Rev. 156, 1415 (1967).

17. A. S. Carroll, I. F. Corbett, C. J. S. Damerell, N. Middlemas, D. Newton, A. B. Clegg, and W. S. C. Williams, Phys. Rev. Letters 16, 288 (1966).

18. H. H. Atkinson, C. R. Cox, P. J. Duke, K. S. Heard, D. P. Jones, M. A. R. Kemp, P. G. Murphy, J. D. Prentice, and J. J. Thresher, Proc. Roy. Soc. (London) A289, 449 (1966) and Phys. Rev. Letters 15, 468 (1965).

19. R. D. Eandi, T. J. Devlin, R. W. Kenney, P. G. McManigal, and B. J. Moyer, Phys. Rev. 136, B536 (1964) and Phys. Rev. 136, B1187 (1964).

20. P. Bareyre, C. Bricman, M. J. Longo, G. Valladas, G. Villet, G. Bizard, J. Duchon, J. M. Fontaine, J. P. Patry, J. Seguinot, and J. Yonnet, Phys. Rev. Letters 14, 198 (1965) and Phys. Rev. Letters 14, 878 (1965).

21. Owen Chamberlain, Michel J. Hansroul, Claiborne H. Johnson, Paul D. Grannis, Leland E. Holloway, Luc Valentin, Peter R. Robrish, and Herbert M. Steiner, Phys. Rev. Letters 17, 975 (1966).

22. S. Suwa, A. Yokosawa, N. E. Booth, R. J. Esterling, and R. E. Hill, Phys. Rev. Letters 15, 560 (1965).

Robert J. Esterling. Roger E. Hill, Norman E. Booth, S. Suwa, and A. Yokosawa, π^- Elastic Scattering Between 1.7 and 2.5 GeV/c, Enrico Fermi Institute for Nuclear Studies, Report No. EFINS 66-29, (1966).

23. P. Bareyre, C. Bricman, A. V. Stirling, and G. Villet, Phys. Letters 18, 342 (1965).

24. R. J. Cence, Phys. Letters 20, 306 (1966).

25. P. Auvil, A. Donnachie, A. T. Lea, and C. Lovelace, Phys. Letters 12, 76 (1964); 19, 148 (1965).

26. A. Donnachie, R. G. Kirsopp, A. T. Lea, and C. Lovelace, "Pion-nucleon phase shifts up to 1311 MeV", presented at the International Conference on High Energy Physics, Berkeley (1966).

27. L. D. Roper, Phys. Rev. Letters 12, 340 (1964); L. D. Roper, R. M. Wright, and B. T. Feld, Phys. Rev. 138, B190 (1965). L. D. Roper and R. M. Wright, Phys. Rev. 138, B921 (1965).

28. M. H. Hull and F. C. Lin, Phys. Rev. 139, B630 (1965).

29. B. H. Bransden, P. J. O'Donnell and R. G. Moorhouse, Phys. Letters 11, 339 (1964); Phys. Rev. 139, B1566 (1965); Proc. Roy. Soc. (London) A289, 538 (1966); Phys. Letters 19, 420 (1965).

30. W. Troka, F. Betz, O. Chamberlain, B. Dieterle, H. Dost, Claude Schultz, and G. Shapiro, Phys. Rev. 144, 1115 (1966).

31. J. H. Foote, O. Chamberlain, E. H. Rogers, H. M. Steiner, Phys. Rev. 122, 959 (1961).

32. S. Kellman, W. P. Kovecik, T. A. Romanowski, Phys. Rev. 129, 365 (1963).

33. H. R. Rugge, O. T. Vik, Phys. Rev. 129, 2300 (1963).

34. Don L. Lind, Barry C. Barish, Richard J. Kurz, Philip M. Ogden, V. Perez-Mendez, Angular Distribution of Charge-Exchange and

Inelastic Neutrons in π^-p Interactions at 313 and 371 MeV, UCRL-11435, October 1964.

35. O. Chamberlain, C. D. Jeffries, C. H. Schultz, G. Shapiro, and L. van Rossum, Phys. Letters 7, 293 (1963).

36. J. H. Foote, O. Chamberlain, E. H. Rogers, H. M. Steiner, C. E. Wiegand, T. Ypsilantis, Phys. Rev. 122, 948 (1961).

37. A. Donnachie and J. Hamilton, Phys. Rev. 133, B1053 (1964) and references cited therein.

38. G. Shapiro, Progr. In Nucl. Techn. and Instrumentation, North-Holland, January 1964.

39. H. H. Atkinson, "Technology of Present High Energy Targets", Proceedings of the International Conference on Polarized Targets and Ion Sources, Saclay, France, December 1966.

40. C. D. Jeffries, Dynamic Nuclear Orientation (Interscience Publishers, New York, 1963).

41. F. Betz, J. Arens, O. Chamberlain, H. Dost, P. Grannis, M. Hansoul, L. Holloway, C. Schultz, and G. Shapiro, Phys. Rev. 148, 1289 (1966).

42. David Cheng, Nucleon-Nucleon Polarization at 700, 600, 500, and 400 MeV (Ph. D. thesis) UCRL-11962 (July 1965) (to be published).

43. Homer A. Neal, Jr., Technical Report No. 23, University of Michigan, Ann Arbor (unpublished).

44. For a description of the properties of the density matrix, see, for instance:

E. Segrè, Appendix F, Nuclei and Particles, Benjamin, N. Y. 1964.

45. J. V. Lepore, Phys. Rev. 79, 137 (1950); J. Ashkin, Suppl. Nuovo Cimento, 14, 221 (1959).

46. E. P. Wigner, Phys. Rev., 98, 145 (1955).
R. H. Dalitz, Ann. Rev. Nucl. Sci., 13, 339 (1963).

47. J. Baacke, private communication.
G. Höhler, G. Ebel, and J. Giesecke, Zeitschrift für Physik 180, 430 (1964).

48. A. H. Rosenfeld, A. Barbaro-Galtieri, W. J. Pololsky, L. R. Price, P. Soding, C. G. Wohl, M. Roos, and W. J. Willis, 39, 1 (1967).

49. P. J. Duke, D. P. Jones, M. A. R. Kemp, P. G. Murphy, J. D. Prentice, J. J. Thresher, H. H. Atkinson, C. R. Cox, and K. S. Heard, Phys. Rev. Letters 15, 468 (1965).

50. A. Yokosawa, S. Suwa, R. E. Hill, R. J. Esterling, and N. E. Booth, Phys. Rev. Letters 16, 714 (1966).

51. W. C. Davidson, "Variable Metric Method for Minimization: VARMIT Method", ANL-5990 (Rev.)(unpublished)(1959).

This report was prepared as an account of Government sponsored work. Neither the United States, nor the Commission, nor any person acting on behalf of the Commission:

A. Makes any warranty or representation, expressed or implied, with respect to the accuracy, completeness, or usefulness of the information contained in this report, or that the use of any information, apparatus, method, or process disclosed in this report may not infringe privately owned rights; or

B. Assumes any liabilities with respect to the use of, or for damages resulting from the use of any information, apparatus, method, or process disclosed in this report.

As used in the above, "person acting on behalf of the Commission" includes any employee or contractor of the Commission, or employee of such contractor, to the extent that such employee or contractor of the Commission, or employee of such contractor prepares, disseminates, or provides access to, any information pursuant to his employment or contract with the Commission, or his employment with such contractor.